New Pathways to Oxide Materials for Photocatalytic Applications

---

Dissertation
zur Erlangung der naturwissenschaftlichen Doktorwürde
(Dr. sc. nat.)

vorgelegt der
Mathematisch-naturwissenschaftlichen Fakultät
der
Universität Zürich

von

Roman Kontic
von Basel BS

Promotionskomitee

Prof. Dr. Greta R. Patzke (Vorsitz)

Prof. Dr. Roger Alberto

Prof. Dr. Roland K. O. Sigel

Zürich, 2014

Contents

Abbreviations

BET	Brunauer-Emmett-Teller
CB	Conduction band
CVD	Chemical vapour deposition
DFT	Density functional theory
DMMP	Dimethyl methylphosphonate
DOS	Density of states
EDX	Energy-dispersive x-ray spectroscopy
EMEZ	Electron microscopy ETH Zurich
FEG	Field emission (electron) gun
FT-IR	Fourier-transform infrared spectroscopy
HRTEM	High resolution transmission electron microscopy
HT	Hydrothermal
ICDD	International center for diffraction data
ICSD	International crystal structure database
LED	Light emitting diode
LA-ICP-MS	Laser ablation inductively coupled plasma mass spectrometry
MAS-NMR	Magic angle spinning nuclear magnetic resonance
PVD	Physical vapour deposition
PXRD	Powder x-ray diffraction
RhB	Rhodamine B
SHE	Standard hydrogen electrode
SEM	Scanning electron microscopy
SNSF	Swiss national science foundation
STEM	Scanning transmission electron microscopy
TBPB	Tetrabutyl phosphonium bromide
TEM	Transmission electron microscopy
UV/vis	Ultraviolet/visible light
VB	Valence band
WOC	Water oxidation catalyst
XPS	X-ray photoelectron spectroscopy

Publications

The following parts of this PhD thesis have been published:

Chapter 1
The introduction contains some modified content of several of the publications mentioned for the following chapters, although most of the content has not been previously published in this form.

Chapter 2
Roman Kontic, Greta R. Patzke:
"Synthetic Trends for $BiVO_4$ Photocatalysts: Molybdenum Substitution vs. TiO_2 and SnO_2 Heterojunctions" *Journal of Solid State Chemistry* **189**:38–48, **2012**.

Chapter 3
Debora Ressnig, Roman Kontic, Greta R. Patzke:
"Morphology Control of $BiVO_4$ Photocatalysts: pH Optimization vs. Self-organization" *Materials Chemistry and Physics* **135**(2–3):457–466, **2012**.

Chapter 4
Roman Kontic, Ari P. Seitsonen, Greta R. Patzke:
"Exploring Vanadate Photocatalysts: Prediction vs. Practice" *submitted*.

Chapter 5
This last chapter gives an outlook on possible approaches to new nitride and oxinitride photocatalysts and summarises some experiments in that direction. It consists mainly of unpublished results.

In addition, the author of this thesis made contributions to the following publications (in reverse order of publication):

- Greta R. Patzke, Roman Kontic, Zeinab Shiolashvili, Nino Makhatadze, and David Jishiashvili:
  "Hydrazine-Assisted Formation of Indium Phosphide (InP)-Based Nanowires and Core-Shell Composites" *Materials* **6**(1):85–100, **2013**.

  The publication demonstrates the formation of indium phosphide nanowires in a one-step chemical vapor process using bulk InP as precursor. In comparison to traditional chemical vapour deposition (CVD) this process does not use expensive and highly toxic volatile In and P precursors. Instead, these precursors are formed *in situ* through the reaction with hydrazine (N_2H_4) vapour containing traces of water (see also section 5.2).

  The process yields InP nanowires with diameters around 20 nm; using mixed starting materials it is also possible to produce core-shell nanowires, with a shell of Ga_2O_3 or amorphous Zn/P/O. The different products and product morphologies can be addressed by tuning the relevant parameters such as source temperature, substrate temperature, distance between source and substrate, partial pressure of hydrazine and water, reaction time, and substrate material.

  The author of the present PhD thesis contributed the analysis with electron microscopy (except HRTEM), energy dispersive x-ray spectroscopy, and powder x-ray diffraction; and supported the preparation of the manuscript.

- Georg R. Meseck, Roman Kontic, Greta R. Patzke, and Stefan Seeger:
  "Photocatalytic Composites of Silicone Nanofilaments and TiO_2 Nanoparticles" *Advanced Functional Materials* **21**(22):4433–4438, **2012**.

  Silicone nanofilaments are presented as a new substrate for TiO_2 nanoparticles. Immobilisation of TiO_2 on high-surface area substrates is important to improve the recyclability of these nano-photocatalysts while preserving the advantage of the high surface area of the nanoparticles.

  Glass slides were covered with a carpet of silicone nanofilaments using a wet chemical approach, based on trichloromethylsilane (TCMS) in dry

toluene. A controlled amount of humidity hydrolysed the TCMS, which subsequently polycondensated to silicon nanofilaments growing from the glass surface. For further functionalisation, these superhydrophilic nanofilaments were treated in an O_2-plasma in order to introduce hydrophilic Si-OH groups.

In a second step, TiO_2 nanoparticles were deposited on the plasma-treated substrates in a water / ethanol mixture, starting from TiF_4. Next to the water content in this mixture and the deposition time, the reaction temperature played a crucial role.

HRTEM images confirm the crystalline nature of the deposited TiO_2 nanoparticles, with sizes in the range between 15 and 25 nm.

To investigate the photocatalytic activity of the samples, dye degradation tests with methylene blue (MB) under black light irradiation were executed in areated aqueous solution. These tests showed a clear advantage of the TiO_2 nanoparticles deposited on nanofilament substrate over a plain glass substrate. Annealing of the samples further improved the activity of the samples. Recycling tests show a high stability of the catalyst, which exhibits only minimal decrease in activity over four subsequent runs.

The author of the present PhD thesis contributed the photocatalytical investigations and supporting discussions about synthetic and analytical techniques.

- Greta R. Patzke, Ying Zhou, Roman Kontic, Franziska Conrad:
  "Oxide Nanomaterials: Synthetic Developments, Mechanistic Studies and Technological Innovations" *Angewandte Chemie International Edition* **50**(4):826–859, **2010**.

  This review article consists of three main parts: (1) Methods for the synthesis of oxides, including the discussion of targeting approaches, (2) discussion of different *in situ* methods for the observation of nanoparticle formation, (3) overview of applications basing on the unique properties of nanoscale materials.

The author of the present PhD thesis contributed the major part of the third section of the review and additionally supported the assembly of the first section.

- Ying Zhou, Kathrin Vuille, Andre Heel, Benjamin Probst, Roman Kontic, Greta R. Patzke:
  "An Inorganic Route to Photocatalytically Active Bismuth Vanadate" *Applied Catalysis A: General* **375**(1):140–148, **2010**.

  A hydrothermal approach towards highly crystalline and highly active $BiVO_4$ particles is presented. The influence of organic (acetic acid) and inorganic (K_2SO_4) additives on the morphology and photocatalytic activity of the products was investigated.

  While the inorganic additive K_2SO_4 leads to an improved particle shape of $BiVO_4$, it also yields nanofibres of a so-far unidentified potassium vanadate as secondary product. Due to the strong difference in shape the two products can be separated by filtration.

  The particles emerging from the synthesis with K_2SO_4 exhibited a more interesting morphology and higher photocatalytic activity in comparison with other synthesis approaches. Visible light photocatalytic activity was investigated by dye degradation experiments as well as by oxygen production experiments. Recycling tests showed some deactivation, but the activity remains high even after four cycles.

  The author of the present PhD thesis contributed some experiments on the bismuth nitrate / vanadium oxide / potassium sulfate system and investigations on the respective products.

Chapter 1

Introduction

1.1 The need for renewable energy and clean water

The advances of chemistry and engineering of the 19th and 20th century brought forth major changes in the societies and economies of western countries.[1] The industrial production of fertilisers and drugs reduced the amount of time and manpower required to produce food for a large number of people and improved the life-expectancy and quality of life of the population. The invention of machines, and later modern informatics, increased the productivity of workers by orders of magnitude. All these changes only opened up the diversity of options and life-styles which are the foundation of "western" societies. Economical and social globalisation spreads all these possibilities, and the desires thereafter, all over the world.[1]

These advanced developments, however, are accompanied by some commonly undesired side-effects. Apart from the social and economical changes, which are not only positive[2,3], the continued pollution of air and water resources increasingly threatens the quality of life of many people, mostly in developing countries but also in the "first world".

The human body contains an average of 70 percent (by weight) of water. Water is essential for all life on earth, where it plays important roles as a solvent, but also as reactant, cooling or transport medium.[4] Over the past century most developed countries installed systems of sewage treatment plants to reduce the impact of household and industrial waste waters on aquatic systems. While these facilities work well for most effluents, there are unfortunately some substances, the so-called *emerging pollutants*, which are not degraded during conventional cleaning steps. The origin of these substances varies from medicaments over pesticides to softening agents for plastics; their common features are that they are not, or only to a small extent, degraded by the existing sewage treatment facilities, and

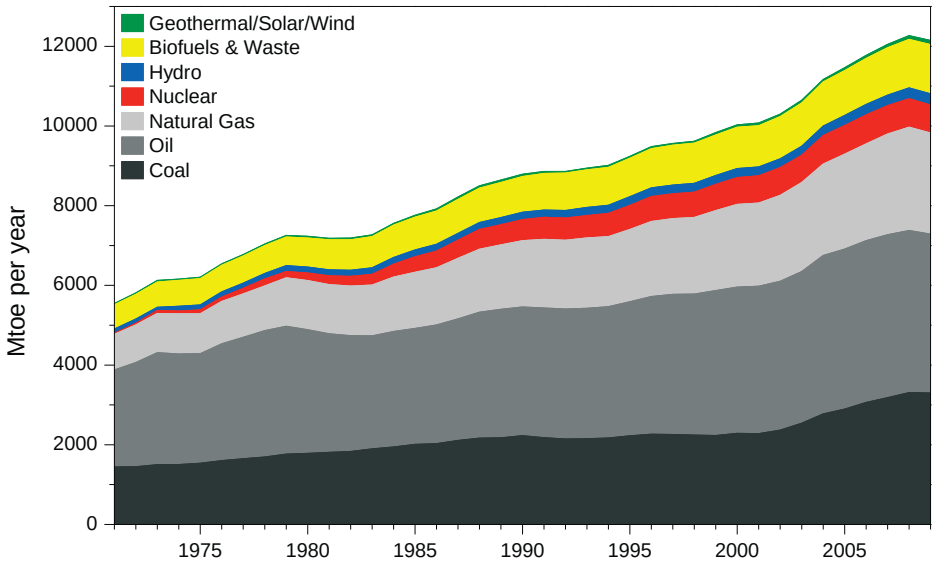

Figure 1.1: The global annual energy production increases almost continuously (shown here over the time span from 1970 to 2009), mostly from fossil fuels.[9]

that they pose a potential threat also in comparatively small quantities[1] through hormone-similar activity or through enrichment in plants and animals.[5]

A multitude of different methods has been proposed to remove such pollutants, such as, filtration, ozonation or photocatalytic processes.[6,7] The latter, which will be discussed in more detail in section 1.2, have the advantage that they can directly utilise light energy from the sun, which reduces the amount of additional energy required for the last cleaning step.

The use of machines powered by external energy sources increases the productivity of a single worker tremendously. As a result, the global energy consumption has increased almost continuously since Watt patented his steam engine in 1769[8]. Figure 1.1 shows the annual world primary energy production over the time interval from 1970 to 2009, broken down into the individual energy sources.

There are several points which are noteworthy about this graph. First, during

[1] In contrast to the "normal" organic contaminants in sewage water, like human and animal feces, paper, etc., which appear in concentrations of up to grams per liter the emerging pollutants are usually observed in quantities below 1 mg/L; therefore they are also referred to as *micro-pollutants*.

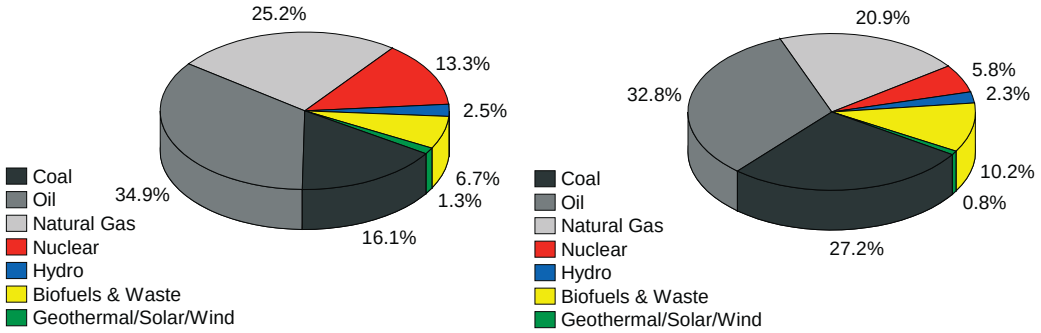

(a) Europe, 100 % = 1'729 Mtoe (b) World, 100 % = 12'150 Mtoe

Figure 1.2: The primary energy supply of 2009 split up by sources, *(a)* for Europe, and *(b)* for the world.[9]

this time period the production of energy has basically doubled from ca. 6'000 to 12'000 Mtoe[2] per year. Second, the increase in energy production stems to a major part from increased use of fossil fuels. This is demonstrated even better by Figure 1.2 where the percentages of the annual energy production in 2009 are compared for Europe and the entire world. In both cases almost 90 % of the production arises from fossil fuels, i.e. coal, oil, natural gas and uranium. In addition, the "biofuels & waste" section contains a considerable (but in the statistics not independently listed) amount of waste which again consists to a significant amount of products produced from fossil carbon sources.

The increasing use of fossil fuels is problematical due to several reasons. One of them is the global climate change induced by massive CO_2 release from fossil fuels. Nowadays the existence of an anthropomorphic climate change is basically unquestioned, and there is more and more evidence that this change actually has already begun.[10,11] Another, less frequently stated issue is the massive impact of fossil fuel production on the ecosystems by large-scale remodeling of the surface as well as pollution due to open-pit mining of coal and uranium[12], pollution from petroleum extraction sites,[13] and finally transport related pollution from oil spills, pipelines and streets through ecologically sensible regions.

Apart from the indirect social and economical challenges posed by climate

[2] *toe* is the abbreviation of *tonne of oil equivalent*; by IEA 1 toe corresponds to 11'630 kWh and 1 Mtoe equals to one million toe.

change there is also a very direct reason for the development of renewable energy sources. At the same rate as the productivity of single workers increased by the use of machines, the dependency of the industry on cheap energy to run these machines has increased. Namely, productivity increases through "technological progress" are mostly caused by increasing the level of automatisation, that is, increasing the amount of work done by machines using cheap energy while decreasing the amount of expensive labour.[14,15] Therefore the price of primary energy more and more determines the production costs and as a consequence the prices of goods and the profitability of companies.

From an economical point of view it is therefore dangerous to rely solely on fossil fuels which are estimated to run out within the next 50 – 150 years. Recent estimates predict production peaks to occur about 2009 – 2021, 2024 – 2046, and 2042 – 2062 for oil, natural gas, and coal, respectively.[16] Of course, this is just an estimate for the occurrence of the peak, and there will still be time before virtually the last source has run dry. On the other side, the sudden surge of prices which will occur when it comes apparent that the peak has actually been passed will make life very difficult for companies which are still solely dependent on fossil fuels. An interesting quote in that context comes from reference 17:

> "*(. . .) the changes caused by the oil price shocks in the 1970s and the resulting energy policies did considerably more to control growth in energy demand and reduce CO_2 emissions than the energy efficiency and climate policies implemented in the 1990s.*"

Fortunately there are solutions to these issues: The so-called *renewable energies* comprise several techniques to harvest the energy of the sun or other energy sources which are "powered" by solar energy, for example wind, biomass, or waves.[3] There are two main advantages of renewable energy sources: They do not increase the CO_2 content of the atmosphere and are therefore *climate neutral*. Moreover, they provide an almost unlimited source of energy:

The sunlight which reaches the earth in one hour carries more energy than was consumed during the whole year 2001;[18] even more, the solar energy arriving on desert surfaces during one year exceeds the total fossil fuel consumption of 2005

[3]Tidal energy, on the other hand, is powered by the rotation of the moon around earth. It still can count as a renewable energy source.

by a factor of 750[19]. Finally, covering 0.16 % of earth's land surfaces by solar panels with 10 % efficiency would yield the projected world energy demand by 2050.[20] In comparison, about 13 % of Germany and about 7 % of Switzerland are covered by settlements and streets;[21,22] and in the United States, an average of 3 % of the states' area counts as urban area[23].

1.2 Heterogeneous photocatalysis for energy production

As outlined in the previous section there is a large interest in techniques which can generate energy from sunlight. Solar energy is usually associated with photovoltaics, where a p-n junction in a semiconductor (usually Si) is used to produce electric energy from sunlight.[24] As the intensity maxima of the sunlight often do not coincide with the peak times of energy use, the generated energy needs to be stored efficiently. One frequently proposed method for this would be to store the energy in chemical form by electrolysis of water, producing H_2 and O_2 which can be used in fuel cells at a later time to produce electric energy.

Hydrogen is also a valuable base chemical for chemical synthesis, nowadays generally produced from non-renewable sources. Millions of tons of ammonia (NH_3) are synthesised annually from hydrogen and nitrogen using the Haber-Bosch reaction (equation (1.1)), as ammonia is a reactant for the synthesis of a multitude of other compounds.[25,26] Another important raw chemical is methanol (CH_3OH) which is mainly produced from natural gas or coal today. Alternatively, hydrogen from renewable sources and carbon dioxide from the atmosphere or captured from major industrial emission sources[27] could be used to produce methanol according to equation (1.2).[28]

$$N_2 + 3H_2 \xrightarrow{cat.} 2NH_3 \tag{1.1}$$

$$CO_2 + 3H_2 \xrightarrow{cat.} CH_3OH + H_2O \tag{1.2}$$

1.2.1 Basics of heterogeneous photocatalysis

Photocatalysis or photoelectrocatalysis are the most direct mechanisms to directly utilise the energy of light to split water into H_2 and O_2 while reducing the overpotential for electrolysis. In *heterogeneous* photocatalysis this is achieved with a

solid photocatalyst (either an electrode or an insoluble catalyst powder) while *homogeneous* photocatalysts are in solution. Although homogeneous photocatalysis is also a highly interesting topic it will not be further discussed here.[29]

Most studies on heterogeneous photocatalysis were inspired by a publication of Fujishima and Honda in 1972.[30,31] The authors describe electrochemical measurements on a TiO_2 electrode under light and in darkness and also state that it is possible to split water without external potential using a combination of an illuminated titania electrode and a Pt counter-electrode, observing oxygen production at the former and hydrogen production at the latter.

The working principle principle of a heterogeneous photocatalyst is rather straightforward: The applied semiconductor materials display a separation between their fully filled *valence band* and their empty *conduction band*, the so-called *band gap*.[4] If a semiconductor is irradiated with light energy exceeding the band gap, electrons can be activated through photon absorption to move from the valence band to the conduction band.[32] The activated electron and the hole remaining in the valence band are then free to move through the semiconductor or can even be transferred to a material in close contact with it. The separated charges can cause redox reactions (preferably) on the surface of the photocatalyst, for example the oxidation and reduction of water.[35]

Since the initial publication of Fujishima and Honda, considerable research has been done to improve the titania catalyst[36,37] and to find other photocatalytic (oxide) materials with visible-light-driven activity.[35,38] Sections 1.3.2 and 1.3 (below) will shed some light on the strategies behind such improvements and on the search for new photocatalysts, respectively. Although it is also possible to use heterogeneous photocatalysis to synthesise or derivatise organic molecules, the following sections will exclusively focus on its application for water splitting or degradation of organic pollutants. Information about the the former topic can be found (among others) in the reviews of Izumi or Ravelli *et al.*[39,40]

[4] For more information about (semi)conductors and band structures please refer to literature, e.g. West[32] or Müller[33]; a very detailed discussion is provided by Duffy[34].

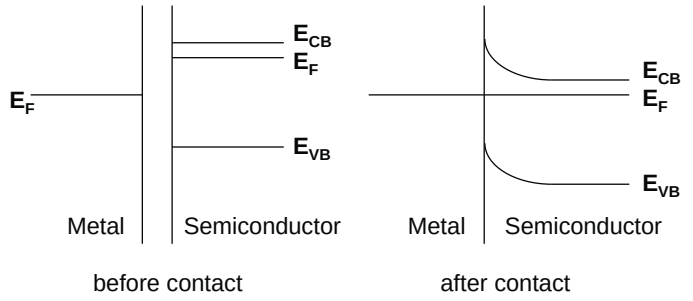

Figure 1.3: Schematic energy diagram of a metal and a n-type semiconductor before and after interface formation. Adapted from reference 41.

1.2.2 Bands and interfaces

The band structure of a photocatalyst is one of its most important characteristics. However, as a general rule in catalysis, the surface or interface region is decisive for the actual reactivity of a heterogeneous photocatalyst. Figure 1.3 shows a schematic band diagram of a semiconductor and a metal, before and after contact. Prior to contact, if we neglect the influence of surface states, the bands are flat up to the surface. In this example we consider a n-type semiconductor, which means that the Fermi level (E_F) of the semiconductor is close to the conduction band. In the initial state, the Fermi level of the semiconductor is higher in comparison to the metal. Upon contact electrons will flow from the semiconductor to the metal to equilibrate the Fermi levels, creating a positive space charge in the semiconductor. A charge carrier in the semiconductor approaching the interface will be increasingly influenced by the space charge as more and more of it is "behind it". As the charge carrier density in the semiconductor is rather low, this leads to a noticeable band bending close to the interface.[41]

The so-called *flat band potential* (V_{FB}) is the potential which needs to be applied to the semiconductor to achieve flat bands again. Although the band bending was illustrated for the example of a metal-semiconductor interface, the concept can easily be transferred to the semiconductor-electrolyte interface. Some complications arise from the fact that the Fermi level of the electrolyte and the surface states of the semiconductor generally are pH dependent.

The band bending affects positive and negative charge carriers differently and can thus improve charge separation. For photocatalytic water splitting, the Fermi

level of the electrolyte is usually determined by the H^+/H_2 redox pair. A certain "overpotential" of the conduction band of the photocatalyst over the final Fermi level is therefore in the interest of a better charge separation.[42]

For the sake of clarity, it is important to point out that the band bending is only a consequence of the underlying difference in electrochemical potential on the two sides of the interface.[43] Upon contact, this difference creates a space charge on both sides of the interface, the extent of which is extremely small on the metal side and still almost negligible in an electrolyte, but more extended in semiconductors due to the comparatively low charge carrier density.[41] In fact, under illumination the photogenerated charge carriers improve the screening of the space charge which can reduce the band bending up to the point where it vanishes.[43,44]

1.2.3 Requirements for an *ideal* heterogeneous photocatalyst

Apart from semiconductors properties, there are several other prerequisites for photocatalyst materials. The band gap needs to be adjusted to the working conditions, especially for visible-light-driven photocatalytic activity. Equation (1.3) shows the relation of the wavelength of electromagnetic radiation λ, in nanometers (nm), to the energy of photons of such radiation E_{photon}, in electron volts (eV); therein the constants h and c correspond to Planck's constant and to the speed of light in vacuum, respectively.[45]

$$E_{\text{photon}} = \frac{h \cdot c}{\lambda} \qquad \text{that is} \qquad E_{\text{photon}}[eV] \approx \frac{1240}{\lambda[nm]} \tag{1.3}$$

For example, titania has a band gap of 3.0-3.2 eV which corresponds to 415-400 nm, that is, titania can only be activated by violet and ultra-violet light. Therefore, undoped titania can only utilise approximately 5 % of the solar light, as can be seen from Figure 1.4. A visible-light-driven photocatalyst should therefore have a band gap between 2.7 and 2.2 eV.

Another important point is the position of the band edges, especially the upper edge of the valence band (VB) and the lower edge of the conduction band (CB). These edges determine the redox strength of the activated electrons and holes, and should therefore be more positive than the O_2/H_2O and more negative than

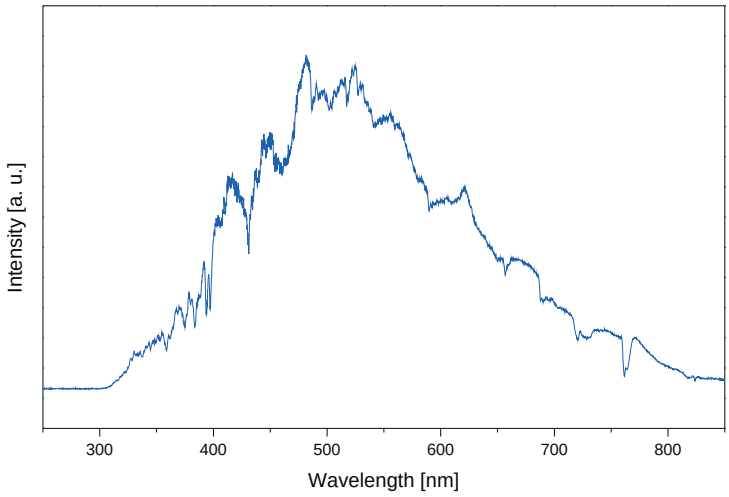

Figure 1.4: The intensity distribution of solar light, measured on a clear day. Typically the range of visible light is defined as 400 to 800 nm.

the H^+/H_2 redox pairs, respectively. Unfortunately, only the size of the band gap can be determined in a straightforward way (see section 1.4.3) while it is rather demanding to locate the exact position of the band edges of powder samples. To establish the band edges, typically one would prepare an electrode from the material in question and determine the so-called *flat band potential*.[46] Figure 1.5 shows band gap values, CB and VB positions for selected photocatalysts.

After the light absorption process, charge carrier separation is of comparable importance to preventing their recombination. This step is strongly affected by crystal structure, particle size, and crystallinity. Defects in the crystal structure can trap charge carriers and act as recombination centres. Furthermore, the smaller the particles are, the shorter is the distance which the charge carriers need to travel to the surface.[35] The delocalisation of the bands, depending on the combination of elemental composition and crystal structure, also plays an important role.[49] Charge separation can be improved by the formation of direct connections between the photocatalyst and another semiconductor, so-called *heterojunctions*. Polar crystal structures with internal dipole moments also help to separate the charge carriers and the distorted perovskites are typical examples for this effect.[32]

Finally, special requirements concern photocatalyst surfaces, which need to

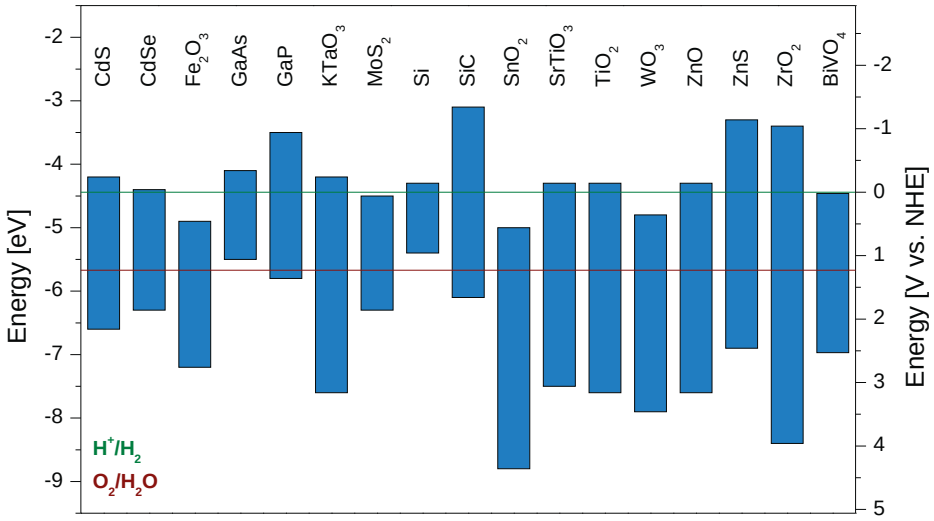

Figure 1.5: Comparison of band gaps of different semiconductors. The green and red lines correspond to the positions of the H^+/H_2 and the O_2/H_2O redox couples, respectively.[35,47,48]

provide sufficient reactive sites for the oxidation and reduction reactions, respectively. The spatial separation of both site types was found to greatly improve the overall efficiency of the water splitting process.[50]

In summary, the criteria for an ideal photocatalyst encompass:

- Stability under reaction conditions; i.e. no dissolution or photocorrosion
- Semiconductor with a band gap width below 3.0 eV, preferably 2.2 – 2.7 eV
- Band edge positions of VB and CB permit oxidation and reduction of water
- High charge carrier mobility; i.e. high crystallinity and delocalised bands
- Quick separation of charge carriers, low recombination rate
- Small particle size, high specific surface area
- Large amount of active surface sites

Given the length of this list, it does not come as a surprise that photocatalytic water splitting is still awaiting its technological and commercial breakthrough in the energy sector — even more so if price as the "most important material property" is added to the above criteria. So-far the number of efficient photocatalysts remains limited, leaving plenty of room for explorations.[51] For a long time, La-doped $NaTaO_3$ reported by Kudo *et al.* in 2003[50] was leading with respect to

quantum yield (QY; 56 % at 270 nm). In comparison, the leader among the visible light active photocatalysts was far behind: A ZnO-GaN solid-solution with a QY of 2.5 % (400 – 420 nm) was reported by Domen *et al.* in 2005.[52] Only recently Ye *et al.*[53] reported Ag_3PO_4 with a QY of over 80 % (470 – 500 nm). Unfortunately the latter catalyst only achieves the O_2-production half reaction, i.e. a lot of research remains to be done to pave the way to commercialisation of clean energy from heterogeneous photocatalysis.

1.3 How to find new heterogeneous photocatalyst materials

In the previous section the various requirements for (ideal) heterogeneous photocatalyst materials were outlined. This section summarises some general strategies in the search for new visible-light active photocatalysts. Currently, this process may better be described as a quest, because reliable prediction of photocatalytic properties from theoretical principles is not fully applicable to date. As a consequence, photocatalyst "design" remains an empirical task to a large extent.

1.3.1 Elements for heterogeneous photocatalysts

The elements which can be used to construct heterogeneous photocatalyst materials are highlighted in Figure 1.6. They can be divided into several categories.

The valence band originates mainly from the anionic sublatice. For pure oxides the valence band derives from O 2*p* orbitals, for sulfides or nitrides the VB derives from S 3*p* or N 2*p* orbitals, respectively. The VB of oxides usually is far more positive than necessary for water oxidation, that is, the band gap becomes unnecessarily wide. Indeed it has been shown, that oxides without partially filled *d*-levels have closely related valence band energies, at approximately 2.9 V vs. SHE, irrespective of the cation.[42] As a consequence, a reduction of the band gap is directly coupled with a shift of the CB level towards more negative values (vs. standard hydrogen electrode (SHE)). Oxides of this type with an absorption edge in the visible range therefore display CB minima more positive than the H^+/H_2 redox pair. In other words, the reduction potential of such oxides is not sufficient for the hydrogen production half reaction of the water splitting reaction. At the same time (cf. section 1.2.2) the band bending depends on the relative positions of

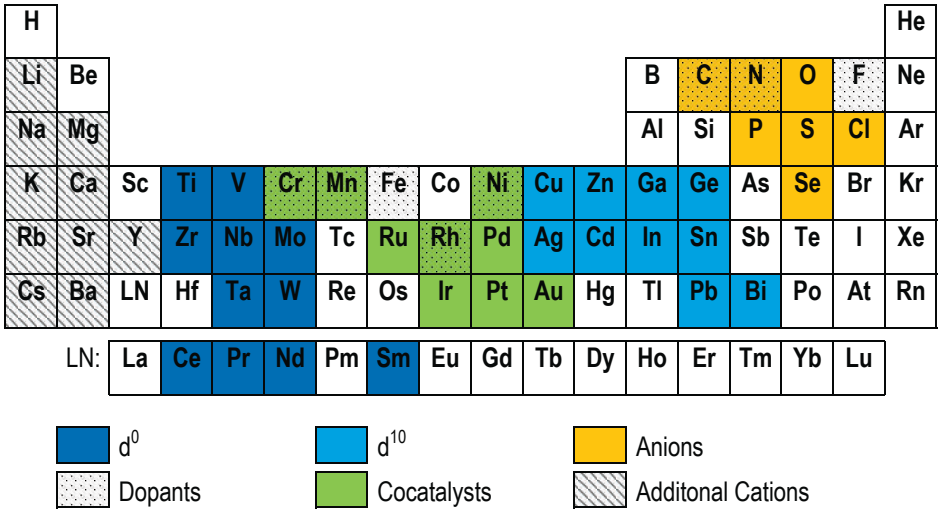

Figure 1.6: Elements used for constructing photocatalyst materials; adapted from reference 35.

the Fermi levels in the semiconductor and in the reaction solution. A Fermi-level of the pristine semiconductor which is lower than that of the solution will lead to a downward bending of the bands, which is unfavourable for the water oxidation reaction.

The energy bands originating from the nitrogen, sulfur, or carbon orbitals generally have a less positive potential, which presents a possibility to reduce the band gap from the valence band side. Another possibility is the combination of several anions into oxynitrides, oxysulfides, etc. which can create a synergism between positive attributes of both anions, such as stability against hydro- or photolysis and an improved VB edge.[54,55]

d^0 and d^{10} *cations* determine the conduction band position, and they are the preferred configuration for photocatalyst construction from multivalent elements. The conduction band consists therefore of d or s states of the corresponding elements.

Recent developments indicate that the delocalisation of the conduction band is very important for the efficiency of the photocatalyst.[49] The spherical symmetry of the s states is highly advantageous for high electron mobility. It is therefore important to minimise the d state contribution to the CB in order to avoid their adverse effect on electron mobility. Increasing the electronegativity of the oxide anions "*by introducing p-block elements with electronegativity closer to that of*

Table 1.1: *p*-block elements for EO_x-cluster formation and their electronegativity (Pauling, according to reference 56).

Element	Electronegativity	EO_x-Cluster
O	3.44	—
Cl	3.16	ClO_4^-
N	3.04	NO_3^-
S	2.58	SO_4^{2-}
C	2.55	CO_3^{2-}
C	2.55	$C_2O_4^{2-}$
P	2.19	PO_4^{3-}
Si	1.90	SiO_4^{4-}

oxygen" was proposed as a stuitable strategy.[49] Generally, in a compound with EO_x-clusters (where E is an electronegative *p*-block element) the covalent character of the E-O bond lowers the electron density on the oxygen and therefore leads to a higher electronegativity of the corresponding oxygen atoms. In turn, this increases the ionic character of the metal EO_x-cluster interaction.

However, some difficulties in the implementation of this concept become evident from the comparison of some *p*-block elements with respect to their electronegativity and potential EO_x-clusters in Table 1.1. It is well known that nitrates, sulfates, most perchlorates and many phosphates are quite soluble - with some prominent exceptions, such as the sulfates of Ca, Ba, and Cs or $BiONO_3$ and the apatite family. Carbonates are less known for their solubility than for their vulnerability to acids, and while oxalates are generally rather insoluble, oxalic acid can be used as reducing agent (via decomposition of the oxalate), which raises doubts about the photocorrosion stability of such compounds. Silicates, finally, are known for their tendency to form glassy phases and Si has the lowest electronegativity in the series. Therefore, although the approach is scientifically interesting, decreasing stability against (photo)corrosion might be expected for more ionic compounds.

However, the intrinsic charge carrier mobility in the photocatalyst material might not play the frequently expected significant role. Especially in nanomaterials, the charge carrier mobility is often determined by the type of defects in the material, as discussed recently.[57] According to this new model, there are so

many defects in a given material and on its surface that trapping of charge carriers becomes inevitable, thus raising the more important question: how strongly are they attached to the traps? So-called *shallow traps* only stabilise the charge carriers to a small extent before they can move on to the next trap, while so-called *deep traps* act as recombination centres. The identification and elimination (or at least reduction) of the deep traps should therefore be of more concern than the optimisation of the charge carrier mobilities of single crystalline materials.

Cations with d^{10} s^2 configuration, i.e. Sn^{II}, Pb^{II} and Bi^{III}, play a special role: their lone electron pair can interact with the valence band forming states and therefore widen the conduction band.[58]

Some photocatalysts contain *additional cations* which mainly the formation of a desired crystal structure or to balance charges, but do not directly contribute to the electronic structure of the material. Additionally, they may help to decrease the electronegativity of the oxygen ions which in turn would raise the VB edge.[34,59,60]

Finally, some elements can be used as *dopants*, to form impurity states in the band gap, or as *cocatalysts*. The latter promote the water reduction or oxidation reaction but do not create their own activated charge carriers under illumination. These options are discussed in detail below.

1.3.2 Improving existing photocatalysts

Several strategies are currently available to increase the visible light absorption of existing photocatalysts, i.e. doping, solid-solution formation, or the use of cocatalysts. Especially the first one, doping, is very popular.[35,37] The principle is the same as for classic semiconductor fabrication: small amounts of impurity atoms should form levels in the band gap to decrease the effective energy needed to activate an electron. Although this generally yields visible light absorption, the photocatalytic activity often drastically decreases.[61,62] If charge balance is not observed, i.e. by multi-element doping, this leads to the formation of defects which can act as recombination centres; furthermore the impurity states in the band gap are generally isolated, which limits the mobility of the charge carriers and again favours recombination. This may be less problematic for dopant ions with d^5 configuration, such as Fe^{III}, Mn^{II}, or Cu^{I}, as this electron configuration is

relatively stable which would allow for the formation of shallow traps.[62,63]

Another technique to improve the separation of photogenerated electron-hole pairs in semiconductors is the formation of composites with heterojunction interfaces between semiconductors with matching band potentials. Cocatalysts materials can as well be used for heterojunction formation. The resulting interface improves the separation of charge carriers and enhances their lifetime - and consequently the photocatalytic efficiency of the material. Further benefits of heterojunctions are possible tuning of the light absorption properties and enhanced interfacial charge transfer efficiency.[35,64–66]

Loading of oxide materials with metal nanoparticles, such as Au, gives rise to surface plasmon resonance, which can also notably improve the photocatalytic activity.[67,68]

1.4 Analytical techniques

1.4.1 Crystal structure determination

As outlined above, the crystal structure of (potential) photocatalysts exerts a considerable influence on their properties. In the course of this thesis, mainly materials with well-determined crystal structure were used. Accordingly it was not necessary to determine new structures and the phase purity of most samples could be verified by comparison of the powder diffraction patterns with reference data from ICDD or ICSD databases.

Powder X-ray powder diffraction (PXRD) patterns were recorded on a STOE STADI P diffractometer in transmission mode (flat sample holders, Ge monochromator and Cu $K_{\alpha 1}$ radiation) equipped with a position sensitive detector. PXRD patterns were refined using the PM2K software[69–71] (Chapter 2) or the Reflex software from the Materials Studio software package (Chapter 4).

1.4.2 Morphology and composition

The morphology of the samples was mainly investigated by scanning electron microscopy (SEM). The SEM images shown throughout this thesis were obtained with a Zeiss Gemini 1530 FEG (“LEO 1530”, acceleration voltage 2 keV) using the secondary electrons detector. Prior to analysis, samples were dispersed in

ethanol and deposited on a Si wafer. Selected images (chapter 3) were taken with a JEOL JSM-6060 SEM (W-cathode) operated at 10 kV. In these cases, samples were dispersed in ethanol and deposited on a conductive carbon plate prior to the measurement.

Investigations with transmission electron microscopy (TEM, TEM-EDX; Chapters 2 and 3) were performed on a Tecnai F30 ST (FEG, 300 kV) at the electron microscopy centre of ETH Zurich (EMEZ).

Specific surface area measurements were performed on a Quantachrome Quadrasorb SI in N_2-adsorption mode. The samples were degassed at 150 °C over night *in vacuo* before the nitrogen adsorption measurements. The adsorption curves were evaluated according to the Brunauer-Emmett-Teller (BET) theory.

Rough elemental composition analysis was done with energy-dispersive X-ray spectroscopy (EDX) on the JEOL SEM (cf. above) operated at 20 – 30 kV with a Bruker Quantax XFlash (133 eV) detector.

Precise Mo contents of the samples in chapter 2 were determined with laser-ablation inductively-coupled plasma mass spectrometry (LA-ICP-MS) at ETH Zurich. A small amount of sample was mixed with Teflon powder, pressed into a pellet and analyzed with a 193 nm ArF excimer laser ablation system (Lambda Physik, Göttingen, Germany) coupled to an ICP-MS (DRC II+, Perkin-Elmer). The samples were ablated for 40 s (5 Hz, 60 μm crater diameter).

Solid state phosphorus nuclear magnetic resonance measurement with magic angle spinning (^{31}P MAS-NMR) was performed on a Bruker DRX-500 spectrometer running at 121.5 MHz at a MAS frequency of 12 kHz under ^{1}H decoupling. The shifts are indicated relative to $(NH_4)_3PO_4$.

Zeta potentials were measured on a Nano-ZS90 device from Malvern Instruments with dispersed powder in milliQ water (70 mg/L) at 25 °C; the pH was adjusted with HCl (0.1 M).

1.4.3 Optical properties and band gap

UV/vis reflectance spectra were measured on a Perkin-Elmer Lambda 650S spectrophotometer with a 150 mm integration sphere. Raman spectroscopy was performed on a Renishaw Ramascope 1000 with a green SpectraPhysics Argon laser

with a wavelength of 524.5 nm and 50 mW capacity.

Band gap values were determined from UV/vis reflectance data using the Tauc-plot method.[72–74] In short, $(\alpha h\nu)^{1/r}$ is plotted against $(h\nu)$, where α is the absorption coefficient, $(h\nu)$ is the energy of the light, and r is 0.5 for a direct and 2 for an indirect band gap. In the case of thick films the following proportionality applies[75]:

$$\alpha \propto \ln\left(\frac{R_{max} - R_{min}}{R - R_{min}}\right)$$

1.4.4 Photocatalytic activity

The performance of the catalysts was tested with two different types of photocatalytic experiments. First, dye degradation experiments with methylene blue (MB) or rhodamine B (RhB), and second, O_2 evolution experiments from water and a sacrificial electron acceptor (iron(III)nitrate). The different setups are briefly outlined in the following.

Dye degradation experiments were carried out with a custom-made lamp arrangement, where 10 commercial 9 W fluorescent lamps (G23 bulb fitting) were arranged around the photoreactor in two half-shells (Figure 1.7). For visible-light degradation experiments "Osram Dulux S 67 blue" lamps were used; Blacklight experiments were performed with "Philips PL-S BLB" lamps. Figure 1.8 shows a comparison of the emission spectra of the lamps and the absorption spectra of the dyes. As can be seen, there is a significant overlap of the emission spectrum of the black light lamps with the absorption spectrum of rhodamine B. This leads to a significantly higher self degradation rate of RhB in comparison to MB under this kind of irradiation which renders this combination of irradiation and dye unsuitable for photocatalytic dye degradation tests (cf. chapter 4).

The photoreactor was equipped with a cooling jacket and a gas dispenser which was used to bubble air through the solution during the reaction at a rate of 100 ml/min. This maintained a constant O_2 saturation in the suspension to avoid reversible reductive bleaching of the dyes.[76] For the black light experiments a quartz glass reactor without cooling jacket was used. The temperature of the suspension was maintained by a cooling finger immersed into the suspension.

In a typical experiment 50 mg of the catalyst was dispersed in 150 mL of

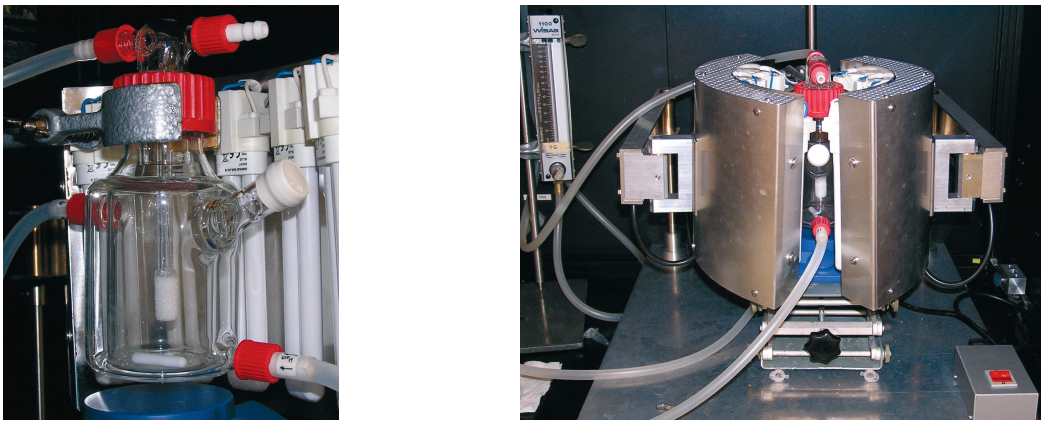

Figure 1.7: Photographs of the photoreactor set-up. Left: from side, one of the lamp half-shells has been moved aside. Right: from front, arrangement for catalytic experiments.

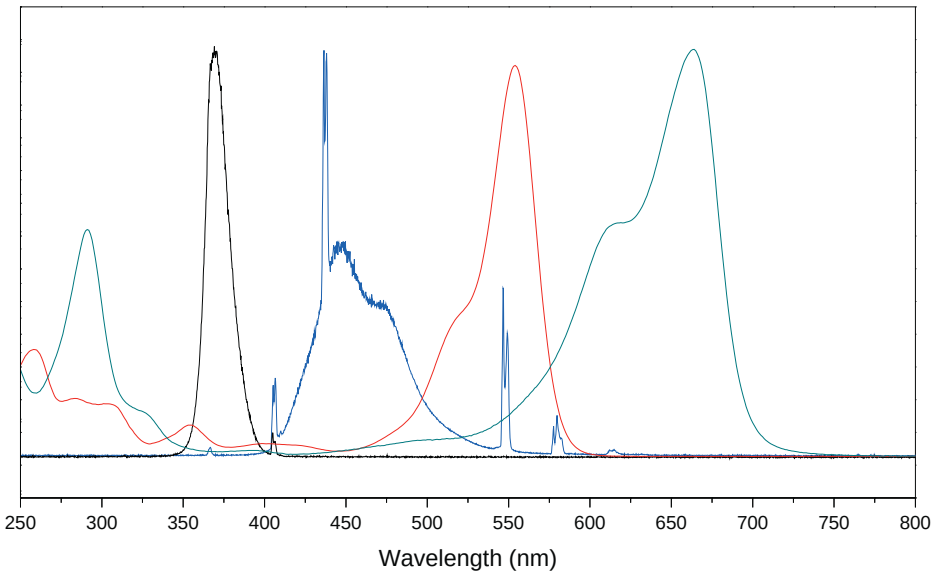

Figure 1.8: Comparison of the emission spectra of the lamps used for the photocatalytic dye degradation experiments (black: black light; blue: blue light) with the absorption spectra of the dyes used (red: rhodamine B, dark cyan: methylene blue).

an aqueous dye solution (5 ppm for MB, 10^{-5} M for RhB) by 10 min ultrasonic treatment. During the reaction, the suspension was thermostatted at 25 °C. At given time intervals 1.5 mL of the suspension was collected, the catalyst separated by centrifugation and the solution analyzed by recording the change of the main peak of the dye with a Perkin-Elmer Lambda 650S spectrophotometer.

Photocatalytic O_2 evolution was carried out in a 20 mL headspace vial (with aluminium crimp cap and rubber septum, BGB Analytik, Switzerland) equipped with a stirring bar and filled with a suspension of 10 mg of the catalyst in 13 mL $Fe(NO_3)_3$ solution (10 mmol/L). The suspension was purged with He to remove all the remaining oxygen from the solvent. The light source was a 476 nm high-flux LED from Rhopoint Components Ltd. (OTLH-0010-BU) with a CPC reflector for Shark LED, operated at usually 4650 lux respectively using a TES 1332A digital lux meter. In regular intervals 100 μL of the reaction headspace were sampled with a gas tight microliter syringe (Hamilton 1825 RN) using a gas chromatograph (Varian CP-3800) with He as carrier gas and a 3 m $\times$ 2 mm column packed with molecular sieve 13X 80 – 100. The gas flow was set to 20 mL/min. The oven was operated isothermally at 100 °C. The gases were detected using a thermal conductivity detector (Varian) operated at 150 °C. Calibrations were performed by the injection of known quantities of pure oxygen diluted in a head space vial containing the same volume of solvent as used for measurements.

Chapter 2

Synthetic Trends for $BiVO_4$ Photocatalysts: Molybdenum Substitution vs. TiO_2 and SnO_2 Heterojunctions

As mentioned in the preceding introductory sections, new visible-light-driven photocatalysts need to be discovered as alternatives to UV-active TiO_2. Among the multitude of possible candidates, bismuth containing oxides have attracted special research interest.[35,77] $BiVO_4$ in particular has shown excellent performance as water oxidation catalyst (WOC) and in the decomposition of organic dyes under visible light irradiation.[78,79] Although its band structure does not support water reduction, $BiVO_4$ can be combined with other photocatalysts into a Z-scheme to achieve overall water splitting.[80]

Synthetic $BiVO_4$ is known in three modifications: the tetragonal zircon type and the monoclinic or tetragonal scheelite structures. The close relation of the tetragonal and the monoclinic scheelite forms has been in the focus of various preparative routes, such as solid state reactions[81], aqueous methods[82,83], or microwave-assisted processes[84]. Ultrasonic[85] and flame spray[86] synthetic pathways to $BiVO_4$ have furthermore been established.

As the actual photocatalytic activity of a given oxide material is not only a function of the given crystal and electronic structure, but also involves a complex interplay of preparative history, crystallinity, surface area and other tuning parameters, the monoclinic scheelite type, which has been identified as the catalytically most active pristine $BiVO_4$ species under visible light irradiation, offers an ideal starting point for further performance optimisation.[83,87] Simultaneous adjustment of parameters, such as stirring, pH, particle shape and subsequent annealing with respect to the resulting photocurrents was illustrated in a recent parameter study on the deposition of $BiVO_4$ films on fluorine-doped tin oxide glass slides.[88] An alternative approach has been implemented by noble metal (Pd, Pt, Ag) deposition on $BiVO_4$, where the enhanced photocatalytic properties were ascribed to improved light absorption as well as to synergistic adsorption processes.[89,90] Doping of $BiVO_4$ with transition or rare earth metals was explored with respect to

metal loading, e.g. Cu-$BiVO_4$,[91] Eu/$BiVO_4$,[92] or Y-substitution of $BiVO_4$[93] which leads to stabilisation of the tetragonal phase in $Bi_{1-x}Y_xVO_4$ catalysts for transformation of carbohydrates.

Heterojunction formation between $BiVO_4$ connected to binary metal oxides has been demonstrated for $BiVO_4/WO_3$[48], $BiVO_4/CuWO_4$[94], and $BiVO_4/WO_3$/cobalt phospate[95] as water oxidation electrode or for functional V_2O_5-$BiVO_4$ composites.[96]

The rich structural chemistry of the $BiMoVO_x$ oxide family has attracted intense research interest,[97,98] whereas surprisingly few studies have been focused on the influence of molybdenum doping on the photocatalytic activity of $BiVO_4$. In the slightly more complex system of $Ca_{1-x}Bi_xV_xMo_{1-x}O_4$ solid solutions, band gap tuning was reported to enhance the O_2 evolution performance with respect to $BiVO_4$.[99] The same authors reported on a productive effect of molybdenum incorporation on the degradation of methylene blue (MB) by $BiVO_4$:Mo under visible light irradiation and they explained the effect through enhanced adsorption affinities of the photocatalyst due to higher surface acidity.[100] These preceding investigations on $BiVO_4$:Mo are based on the hypothesis that Mo(VI) substitutes V(V) in the monoclinic scheelite-type $BiVO_4$ host lattice. The results were further corroborated with studies on $Bi_{1-x/3}V_{1-x}Mo_xO_4$ ($x = 0 - 0.3$) solid solutions.[100,101] In addition, since the publication of the present study a couple of new reports about the use of molybdenum-substituted $BiVO_4$ in photocatalytic and photoelectrocatalytic applications were published.[102–104]

However, even after thorough enquiries no structural database entries could be found for monoclinic Bi(V,Mo)O_4 phases. On the contrary, it has long been established that molybdenum incorporation into $BiVO_4$ leads to the stabilisation of the tetragonal scheelite-type in solid solutions over the entire $Bi_{1-x/3}V_{1-x}Mo_xO_4$ compositional range until an abrupt structural change sets in for the end member $Bi_2(MoO_4)_3$.[105,106] Follow-up studies on $Bi_{1-x/3}V_{1-x}Mo_xO_4$ compounds as oxidation catalysts for organic substrates[107] or as candidates for solid electrolytes[108] have widely confirmed this extended solubility of molybdenum in tetragonal $BiVO_4$ matrices. Furthermore, the proposed monoclinic $BiVO_4$:Mo catalysts were synthesised at rather high calcination temperatures (800 °C) which is significantly above the onset of MoO_3 sublimation (ca. 700 °C)[109]. However, the reported

molybdenum incorporation extent (2 at-%) was not verified by quantitative bulk analysis after thermal treatment to exclude any thermal molybdenum losses.[100] In such cases of thermal instability, thorough analytical characterisations of mixed phases are indispensable, especially as other studies reported on particle melting around 800 °C in Bi/V/Mo/O systems.[101] Accordingly, the first part of the following systematic hydrothermal study focuses on synthesis-structure-activity relationships among $BiVO_4$:Mo solid solutions in order to clarify the influence of V/Mo substitution on phase, particle shape, surface area, thermal stability and catalytic performance of the products.

Reports on $BiVO_4$@TiO_2 heterojunction composites with $BiVO_4$ being the major component were limited at the time of the present investigations,[110,111] and meanwhile the general research state has not changed significantly in this respect. Other attractive targets would be $BiVO_4$@SnO_2 coatings, inspired by previous reports on efficient FTO/SnO_2/$BiVO_4$ water splitting electrodes.[112] The second part of this hydrothermal study is thus focused on the influence of TiO_2 or SnO_2 coating, respectively, on the photocatalytic performance of $BiVO_4$ and $Bi_{1-x/3}V_{1-x}Mo_xO_4$ materials. Finally, the influence of surface tuning vs. substitutional modifications is differentiated with respect to the performance of the emerging catalysts in visible-light-driven decomposition of methylene blue (MB) or water oxidation.

2.1 Preparation of $Bi_{1-x/3}V_{1-x}Mo_xO_4$ and coating procedures

In a typical synthesis of $BiVO_4$ nanoparticles, 97 mg of $Bi(NO_3)_3{\cdot}5H_2O$ and 18 mg of V_2O_5 were dispersed in water by 10 min of treatment in an ultrasonic bath. The suspension was transferred into a Teflon-lined stainless steel autoclave with a capacity of 15 mL, filling it to 10 mL, and maintained at 220 °C for 24 h, followed by cooling down to room temperature naturally. The product was collected by centrifugation, repeatedly washed with water and dried in air at 80 °C.

An analogous procedure was applied for the synthesis of the $Bi_{1-x/3}V_{1-x}Mo_xO_4$ samples where the V_2O_5 was partially replaced by Na_2MoO_4 with a constant 1:1 molar ratio of Bi : (V + Mo) in the reaction mixture. In the following the samples will be referred to as $BiVO_4$_X% Mo, where X refers to the percentage of

vanadium replaced by molybdenum in the as-synthesised products (Table 2.1).

For TiO_2 coating, 150 mg of the nanoparticles were suspended by ultrasonication in 10 mL of a 1:1 water / ethanol mixture before adding 30 mg TiF_4 to the suspension, followed by stirring in a closed vial at 60 °C for 2 h. For the SnO_2 coating, 150 mg of the nanoparticles were suspended by ultrasonication in 10 mL water at pH 2 (adjusted by diluted HNO_3) before adding 6 mg SnF_2 to the suspension which was then transferred to a Teflon-lined stainless steel autoclave with a capacity of 15 mL and maintained under stirring at 160 °C for 5 h. For both coating procedures the reaction vessels were cooled down to room temperature naturally and the products were collected by centrifugation, repeatedly washed with water and dried in air at 80 °C.

To investigate the influence of calcination on the properties of the different products, a part of the products was calcined in air at 500 °C for 5 h.

2.2 Hydrothermal synthesis, characterisation and photocatalytic performance of $Bi_{1-x/3}V_{1-x}Mo_xO_4$ materials

A series of mixed $Bi_{1-x/3}V_{1-x}Mo_xO_4$ ($0 < x < 0.15$) oxides was obtained by hydrothermal synthesis, as described above. Molybdenum contents before and after thermal treatment were determined with LA-ICP-MS analyses to quantify the extent of molybdenum incorporation. The analytically determined degree of molybdenum incorporation in the as-synthesised products agrees well with the initial molybdenum content (Table 2.1). Furthermore, calcination at 500 °C, i.e. well below the onset of MoO_3 sublimation, does not lead to significant molybdenum loss over the investigated compositional range.

The characteristic region between 28° and 36° 2θ of the PXRD patterns of as-synthesised and calcined $Bi_{1-x/3}V_{1-x}Mo_xO_4$ ($0 < x < 0.15$) samples is displayed in Figure 2.1. Whereas as-synthesised pristine $BiVO_4$ consists mainly of the monoclinic scheelite phase, the amount of the tetragonal modification increases continuously with the molybdenum content of the samples as expected from preceding solid state studies[105]. Significant amounts of monoclinic scheelite are present in the $BiVO_4$, $BiVO_4$_2% Mo and $BiVO_4$_4% Mo samples after calcination (Figure 2.1, left), whereas only the tetragonal modification prevails at higher molybde-

Table 2.1: Initial vs. analytically determined compositions of the $Bi_{1-x/3}V_{1-x}Mo_xO_4$ series (values for as-synthesised and calcined samples).

Initial Mo at-% Mo	As-synth. at-% Mo	Composition	Abbreviation	Calcined at-% Mo
2	2.1	$Bi_{0.99}V_{0.98}Mo_{0.02}O_4$	$BiVO_4$_2% Mo	2.1
5	4.0	$Bi_{0.98}V_{0.96}Mo_{0.04}O_4$	$BiVO_4$_4% Mo	4.0
10	7.7	$Bi_{0.97}V_{0.92}Mo_{0.08}O_4$	$BiVO_4$_8% Mo	7.4
15	10.8	$Bi_{0.96}V_{0.89}Mo_{0.11}O_4$	$BiVO_4$_11% Mo	10.3
20	15.1	$Bi_{0.95}V_{0.85}Mo_{0.15}O_4$	$BiVO_4$_15% Mo	13.9

num contents from $BiVO_4$_8% Mo onwards. At first glance, this appears to indicate that molybdenum can be incorporated into monoclinic $BiVO_4$ with hydrothermal methods. However, only the lattice constants of the tetragonal phase displayed the expected significant increase with the molybdenum content[105], whilst the values for the monoclinic phase remained unchanged (Figure 2.2). This indicates that the molybdenum uptake of monoclinic $BiVO_4$ is negligible in comparison with the formation of tetragonal $Bi_{1-x/3}V_{1-x}Mo_xO_4$ compounds.

The influence of hydrothermal molybdenum incorporation on $Bi_{1-x/3}V_{1-x}Mo_xO_4$ particle morphology was newly investigated. Despite the presence of both modifications, all samples display a rather homogeneous particle size distribution as can be seen from the SEM images in Figure 2.3. The particle size of the as-synthesised materials (Figure 2.3, top) decreases continuously with the extent of molybdenum incorporation from 200 – 400 nm in pristine $BiVO_4$ over 70 – 270 nm in $BiVO_4$_8% Mo to an average particle size of 50 nm in $BiVO_4$_15% Mo. This trend is maintained after calcination (Figure 2.3, bottom). Furthermore, increasing molybdenum contents appear to stabilise the exposition of crystal facets after calcination as can be seen from a comparison of the almost spherical $BiVO_4$ particles obtained after heating to 500 °C with the morphologically well-defined calcined $Bi_{1-x/3}V_{1-x}Mo_xO_4$ samples (Figure 2.3).

The above-mentioned decrease of particle size upon molybdenum incorporation goes hand in hand with increasing surface areas (Table 2.2, left). Lower molybdenum contents stabilise the particles against sintering, because a significant loss of surface area can only be observed for samples $BiVO_4$_11% Mo and $BiVO_4$_15% Mo. The latter samples furthermore are the only members of the se-

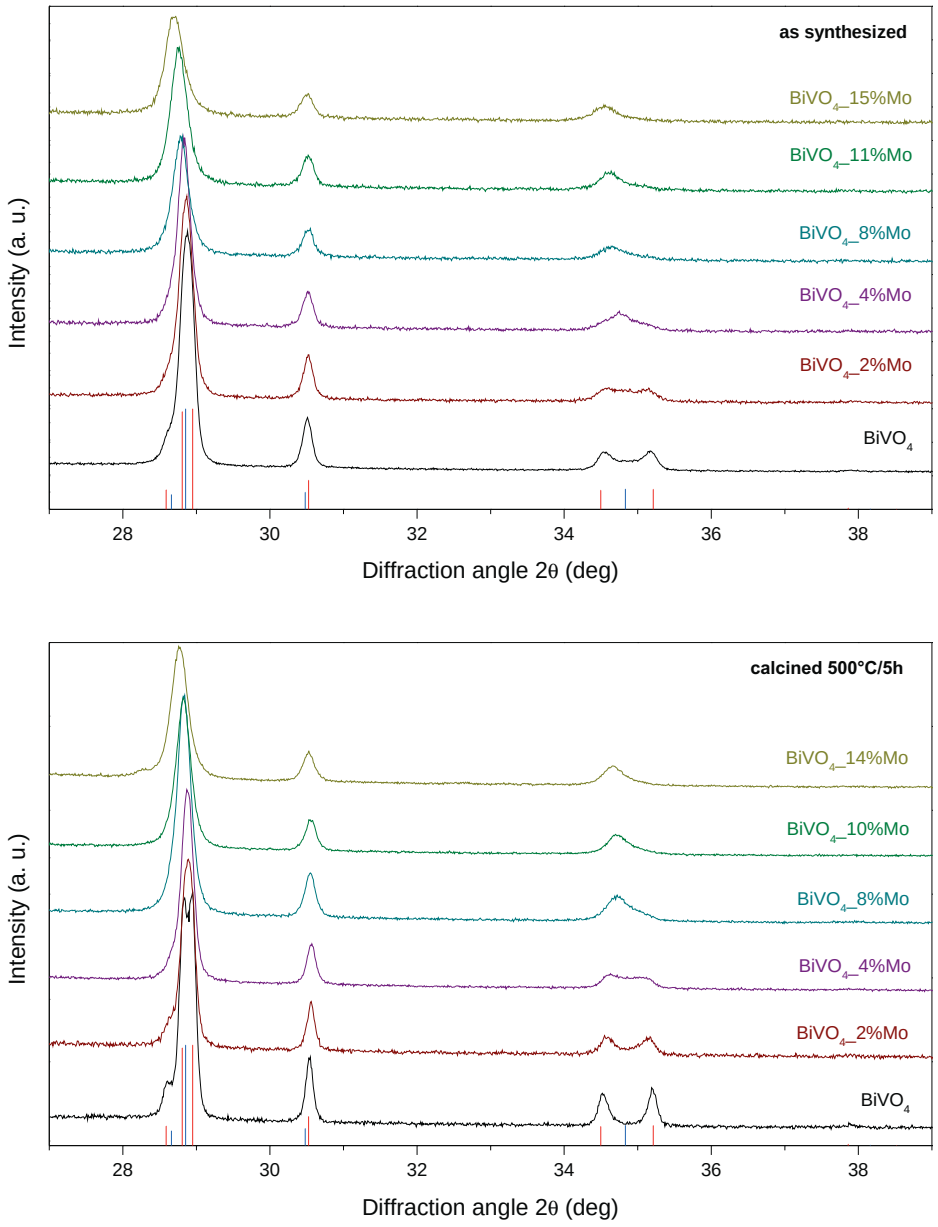

Figure 2.1: PXRD patterns of the as-synthesised (top) and the calcined (bottom) $Bi_{1-x/3}V_{1-x}Mo_xO_4$ samples. Reference patterns of the monoclinic (red, PDF 83-1700) and tetragonal (blue, PDF 83-1696) scheelite structure of $BiVO_4$ are displayed below the measured patterns.

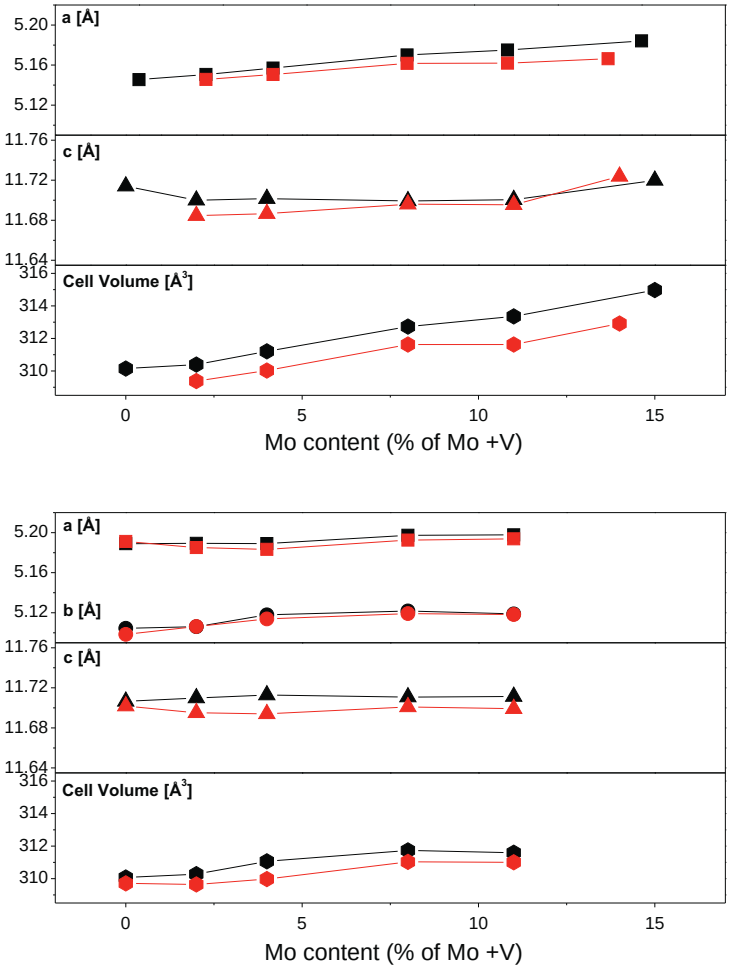

Figure 2.2: Lattice parameters (black: as-synthesised, red: calcined) for the tetragonal $BiVO_4$ phase (top) and for the monoclinic $BiVO_4$ phase (bottom).

Table 2.2: BET surface area values (m^2/g) of the as-synthesised and coated $Bi_{1-x/3}V_{1-x}Mo_xO_4$ samples before (a) and after (b) calcination.

sample	as-synthesised		TiO_2 coated		SnO_2 coated	
	a	b	a	b	a	b
$BiVO_4$	3.4	3.1	6.0	3.9	7.5	5.6
$BiVO_4$_2% Mo	3.3	3.3	7.5	4.0	8.5	5.8
$BiVO_4$_4% Mo	4.4	4.2	9.7	5.9	14.4	8.0
$BiVO_4$_8% Mo	7.4	7.0	14.3	8.4	18.6	12.1
$BiVO_4$_11% Mo	10.1	7.0	15.9	8.2	20.5	14.0
$BiVO_4$_15% Mo	14.4	7.2	20.1	8.1	24.3	15.1

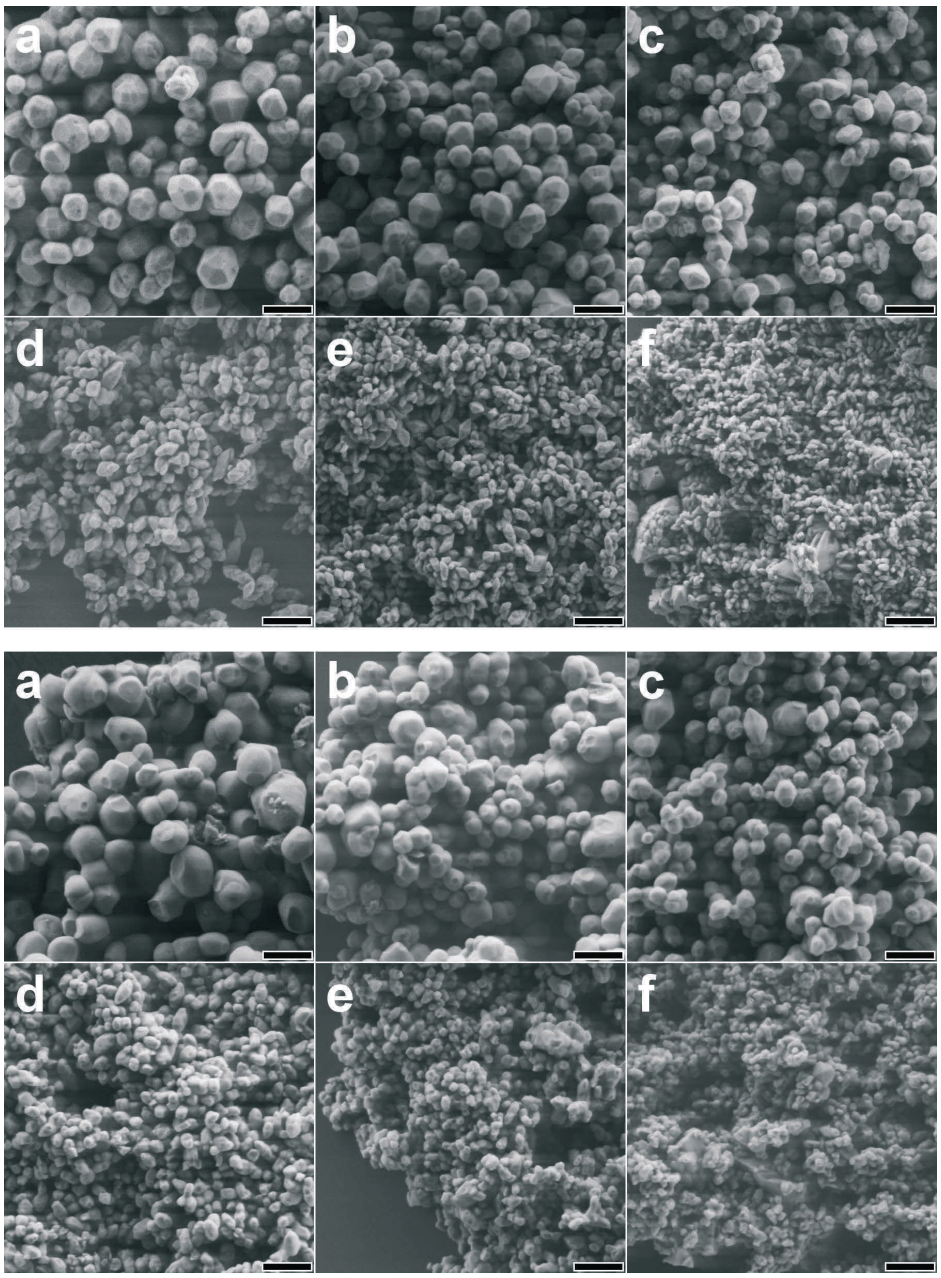

Figure 2.3: Representative SEM images showing the influence of increasing molybdenum content (a: $BiVO_4$, b: $BiVO_4$_2% Mo, c: $BiVO_4$_4% Mo, d: $BiVO_4$_8% Mo, e: $BiVO_4$_11% Mo and f: $BiVO_4$_15% Mo) on the particle morphology (top: as-synthesised, bottom: after calcination (500 °C / 5 h); scale bar = 400 nm).

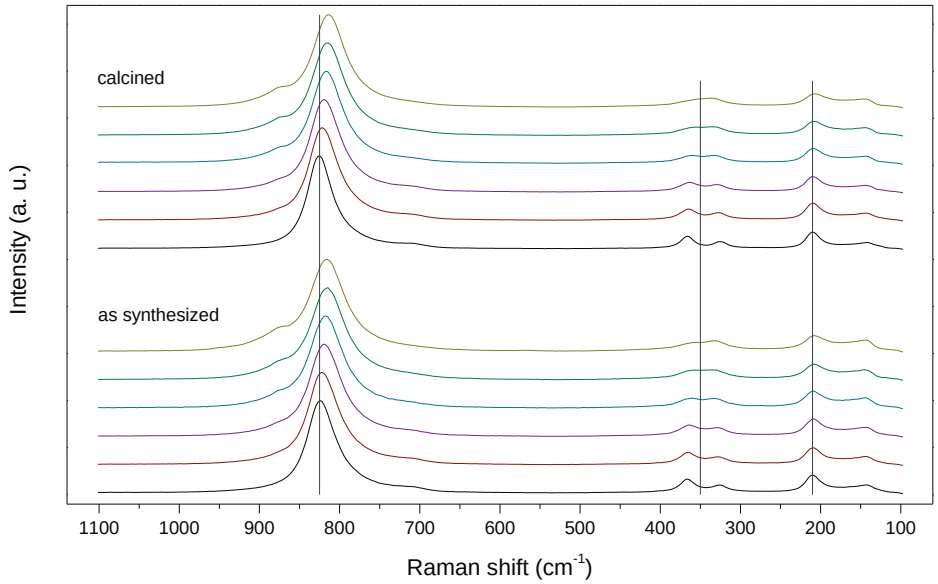

Figure 2.4: Influence of the increasing initial molybdenum content (from black to olive green, same colour code as in Figure 2.1) on the Raman spectra of as-synthesised and calcined $Bi_{1-x/3}V_{1-x}Mo_xO_4$ ($0 < x < 0.15$) samples.

ries that display significant molybdenum loss during calcination (Table 2.1) which is likely to induce surface rearrangements. Interestingly, the BET surface area of pristine $BiVO_4$ remains unchanged after calcination although the crystal facets are less pronounced afterwards (Figure 2.3). This illustrates the dual stabilizing influence of moderate V/Mo substitution (up to 5%) on both surface area and particle shape.

The influence of increasing molybdenum contents on the Raman spectra of the $Bi_{1-x/3}V_{1-x}Mo_xO_4$ ($0 < x < 0.15$) series is evident from Figure 2.4: the characteristic symmetric V-O stretching mode (A_g) is shifted from 822 cm^{-1} for as-synthesised pristine $BiVO_4$ to 814 cm^{-1} for $BiVO_4$_15% Mo. Whereas the value for the undoped sample agrees well with literature data (826 cm^{-1})[84] the observed shift to lower frequencies with increasing content of tetragonal phase among the series is in opposite direction to reference data[113] for the symmetric V-O stretching band of tetragonal $BiVO_4$ at 850 cm^{-1} and must therefore be ascribed to the influence of the molybdenum content. Generally, this explanation is in line with the previous reports on $BiVO_4$:Mo (2 at-%) and with a peak position around 820 cm^{-1} observed for tetragonal $Bi_{0.85}V_{0.55}Mo_{0.45}O_4$.[100,108] In addition, a shoulder near

867 cm^{-1} appears from $BiVO_4$_8% Mo onwards that might be assigned to isolated MoO_4^{2-} tetrahedra which are observed at higher frequencies as shown in key studies on tetrahedral anions as well as in recent investigations on VO_4^{3-} (826 cm^{-1}) vs. MoO_4^{2-} (897 cm^{-1}) moieties in $Mg_{2.5}VMoO_8$.[114,115] Monoclinic phase contents are furthermore evident from lower frequency peaks around 371, 333, and 213 cm^{-1} that are in line with the reported values for the symmetric V-O bending (A_g) modes at 365 cm^{-1} and the antisymmetric V-O (B_g) bending mode at 333 cm^{-1}, respectively, as well as with an external mode at 208 cm^{-1}.[84] All peak positions remain practically unchanged upon calcination. The V-O bending modes converge into a single band which is located at 348 cm^{-1} for the mostly tetragonal $BiVO_4$_15% Mo sample. As the single O-V-O bending mode (A_g) of tetragonal $BiVO_4$ is expected at 380 cm^{-1} from literature data,[116] this shift to lower frequencies is likely to arise from molybdenum incorporation into the crystal lattice, and it follows the trend for the V-O stretching band.

Figure 2.5 illustrates the influence of increasing molybdenum contents on the UV/vis spectra of as-synthesised and calcined $Bi_{1-x/3}V_{1-x}Mo_xO_4$ ($0 < x < 0.15$) materials. Two trends are emerging for both sample series: higher molybdenum contents leads to a blue shift of the absorption edge in all samples and calcination slightly decreases the band gap. Concerning pristine $BiVO_4$, this is in line with the reduction of the tetragonal phase content (band gap of 2.9 eV for the tetragonal zircon phase)[84] in favor of monoclinic $BiVO_4$ (band gap 2.4 eV)[84] upon thermal treatment. Two parameters are involved in the observed blue shift among the $Bi_{1-x/3}V_{1-x}Mo_xO_4$ series, namely the molybdenum-induced stabilisation of the tetragonal phase and a potential influence of molybdenum substitution on the electronic structure. Interestingly, however, previous experimental studies indicate a productive influence of molybdenum incorporation into $BiVO_4$ matrices which is probably a more complex phenomenon that cannot be explained in terms of band gap tuning alone.[99,100]

The photocatalytic performance of the hydrothermally synthesised vs. calcined $Bi_{1-x/3}V_{1-x}Mo_xO_4$ ($0 < x < 0.15$) samples is shown in Figure 2.6. As-synthesised pristine $BiVO_4$ displays the highest activity in the decomposition of methylene blue (MB) under visible light irradiation and all of the as-synthesised mylbdenum containing samples are less active. Obviously, the enhanced surface

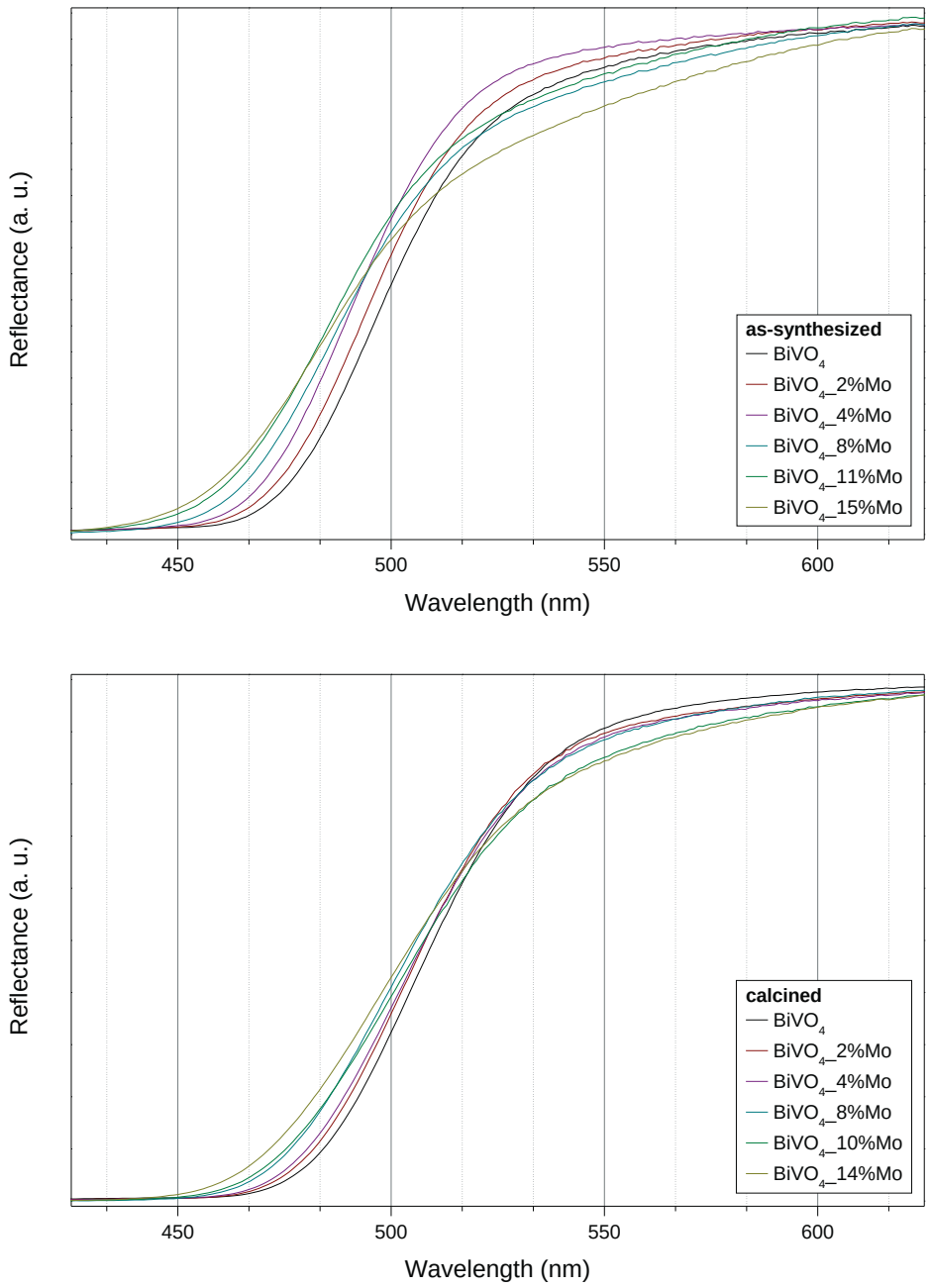

Figure 2.5: Comparison of the UV/vis spectra of as-synthesised (top) and calcined (bottom) $Bi_{1-x/3}V_{1-x}Mo_xO_4$ ($0 < x < 0.15$) samples.

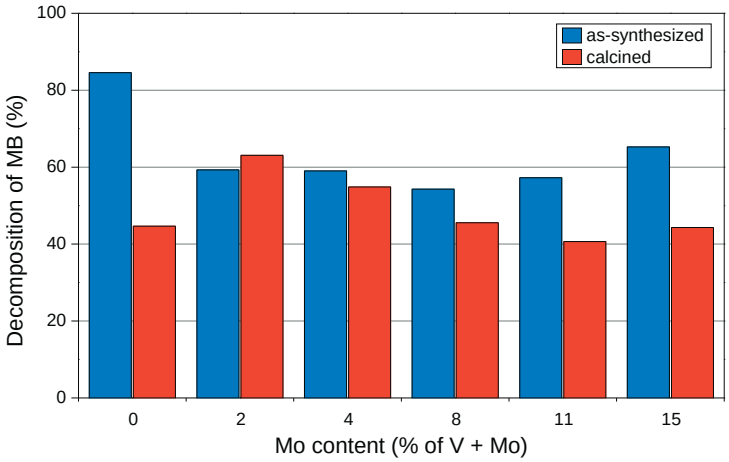

Figure 2.6: Methylene blue degradation of as-synthesised and calcined $Bi_{1-x/3}V_{1-x}Mo_xO_4$ ($0 < x < 0.15$) samples under visible light irradiation (MB degradation after 2 h).

areas of the $Bi_{1-x/3}V_{1-x}Mo_xO_4$ samples and enhanced surface reactivity through molybdenum centres cannot fully compensate the continuous blue shift of the absorption edge (Figure 2.5. At first glance, this suggests a counterproductive influence of molybdenum on the overall photocatalytic activity. Interestingly, however, calcination of pristine $BiVO_4$ significantly reduces its photocatalytic activity — despite a narrowing of the band gap, a higher amount of the more active monoclinic phase and unchanged BET surface area in comparison with as-synthesised $BiVO_4$. It is noteworthy that calcined $BiVO_4$_2% Mo and $BiVO_4$_4% Mo exhibit higher photocatalytic activity than calcined $BiVO_4$, although both samples display higher tetragonal phase contents together with blue shifts of the absorption edge and comparable surface areas (Table 2.2). The performance of the remaining calcined samples ($BiVO_4$_8% Mo to $BiVO_4$_15% Mo) is comparable to pristine calcined $BiVO_4$.

Given that the phase trends among calcined and as-synthesised samples are analogous, which is supported by the powder diffraction patterns (Figure 2.1), the reason for the declined activity of calcined $BiVO_4$ is probably linked to the loss of exposed and reactive crystal facets during calcination as is evident from the comparison of SEM images before and after calcination (Figure 2.3). In comparison, the calcined $Bi_{1-x/3}V_{1-x}Mo_xO_4$ (x = 0.02, 0.04) samples benefit from more pronounced crystal shapes which might also enhance molybdenum-related surface

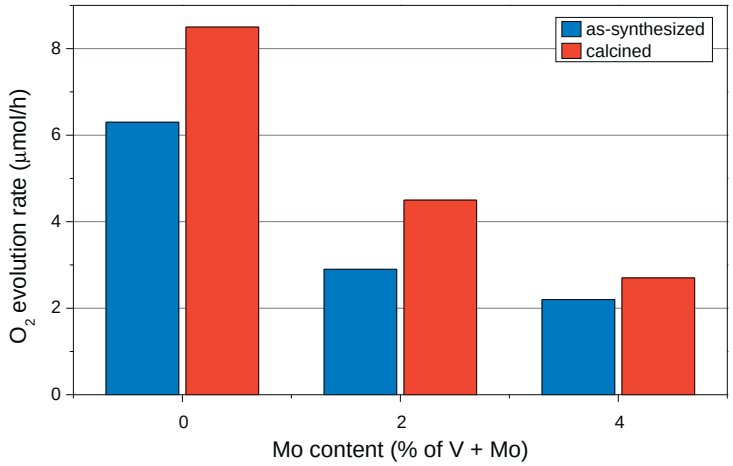

Figure 2.7: Comparison of the photocatalytic O_2 production of as-synthesised and calcined $Bi_{1-x/3}V_{1-x}Mo_xO_4$ ($0 < x < 0.15$) samples under visible light irradiation.

acidity and reactivity. Given that higher molybdenum contents may exert an overall deteriorating effect as indicated from the results on as-synthesised products, replacement of 2-5% V by Mo, followed by calcination under mild conditions (500 °C) is an optional procedure to generate $Bi_{1-x/3}V_{1-x}Mo_xO_4$ photocatalysts for the decomposition of organic compounds.

Figure 2.7 compares the photocatalytic O_2 production performance of calcined and as-synthesised $BiVO_4$ to the above selected $Bi_{1-x/3}V_{1-x}Mo_xO_4$ (x = 0.02, 0.04) samples. Other than in MB decomposition, the pristine $BiVO_4$ sample displays enhanced activity after calcination as expected from phase contents and absorption edge trends. In sharp contrast to the aforementioned productive influence of molybdenum incorporation and calcination on MB degradation (Figure 2.6), the O_2 evolution rate of the Mo-containing samples decreases notably in comparison with calcined $BiVO_4$.

These observations are fully in line with the UV/vis trends for all catalyst samples as shown in Figure 2.5: band gap widening lowers O_2 production efficiency. This agrees with a preceding study on different parameters trends among hydrothermally $BiVO_4$ synthesised particles with respect to MB decomposition and water oxidation: Degradation of organic compounds requires optimised particle morphologies and high surface areas, whereas band gap as well as overall crystallinity are more important for O_2 evolution.[117] Mo^{VI} ions are furthermore

potential recombination centres that can diminish O_2 production: this may explain the considerable differences between the present results and the previously reported[100] enhanced O_2 evolution performance of $BiVO_4$:Mo. The emerging overall trends for the hydrothermal synthesis of photocatalytic $Bi_{1-x/3}V_{1-x}Mo_xO_4$ ($0 < x < 0.15$) materials can be summed up as follows:

- The applied template-free hydrothermal technique is preferable over sintering pathways to $BiVO_4$ based photocatalysts for the degradation of organic compounds, because calcination above 500 °C bears the risk of molybdenum loss and permits less control over morphology and surface area.
- Molybdenum incorporation generally stabilises the less active tetragonal $BiVO_4$ modification and this effect cannot be circumvented by "soft" hydrothermal strategies.
- The advantages of hydrothermal synthesis over classic solid state formation of $Bi_{1-x/3}V_{1-x}Mo_xO_4$ materials lie in the decrease of particle size with increasing molybdenum content, accompanied by larger surface areas and, most importantly, enhanced morphological stability of the samples against calcination.
- Unfortunately, the blue shift of the absorption edge through stabilisation of the tetragonal scheelite structure and the presence of possible recombination centres outweigh these benefits of molybdenum incorporation.

As a result, preceding studies on enhanced O_2 evolution with monoclinic $BiVO_4$:Mo catalysts[100] could not be confirmed and molybdenum-doping of $BiVO_4$ can neither be recommended for MB degradation nor water oxidation catalysis at the present stage. Calcination of the hydrothermally obtained $BiVO_4$-based catalysts is not essential for MB degradation but increases the O_2 production activity. Only if special thermal post-treatment of wastewater treatment catalysts is required, e.g. to guarantee long-term stability under demanding conditions, moderate hydrothermal V/Mo substitution (up to 4%) can be productive for the performance improvement of $Bi_{1-x/3}V_{1-x}Mo_xO_4$ photocatalysts.

2.3 Influence of TiO_2 and SnO_2 coating on the photocatalytic performance of $Bi_{1-x/3}V_{1-x}Mo_xO_4$ materials

TiO_2 nanoparticles were deposited on the surface of $Bi_{1-x/3}V_{1-x}Mo_xO_4$ ($0 < x < 0.15$) materials with a mild one-step procedure, like described above, in order to investigate the effect of nanoscale heterojunction formation on the emerging products. Figure 2.8 displays representative SEM images of the composites before and after calcination. The freshly deposited TiO_2 particles have diameters of 10 – 20 nm and they are preferentially deposited on specific crystal facets where their size remains constant after thermal treatment.

Unfortunately, the degree of coating was too low to permit a differentiation between rutile and anatase in the Raman spectra (Figure 2.10) and the powder diffraction patterns did not even show the presence of TiO_2. HRTEM investigations confirm the small particle size and the crystallinity of the deposited TiO_2 particles as well as the presence of TiO_2-free facets (Figure 2.9).

TiO_2 coating notably enhances the BET surface area of the as-synthesised composites by a factor of 1.5 to 2 (Table 2.2). Although these values are basically reduced to those of the pristine oxides after calcination, the morphology and crystal facets of the calcined products are maintained quite well (Figure 2.8) and this applies especially in comparison with pristine calcined $BiVO_4$ (Figure 2.3 a, bottom).

Other than the facile TiO_2 deposition under ambient conditions, hydrothermal treatment was required to obtain SnO_2 coating from the SnF_2 precursor. SEM images show that the $BiVO_4$ substrates are covered with a dense layer of rather small SnO_2 particles (Figure 2.11). HRTEM investigations (Figure 2.9) demonstrate that their maximum diameters are around 15 nm and that they are distributed without any morphological preferences all over the $BiVO_4$ substrate.

The presence of Ti and Sn, respectively, on the $BiVO_4$ surface was confirmed with STEM-EDX measurements. The morphology of the coating TiO_2 and SnO_2 particles, respectively, are maintained during calcination so that the bismuth vanadate based core particles are protected against further agglomeration. The BET surface areas of the as-synthesised $BiVO_4$_X% Mo@SnO_2 (X = 0, 2, 4, 8, 11, 15) composites exceed those of the TiO_2 analogues as a consequence of the smaller

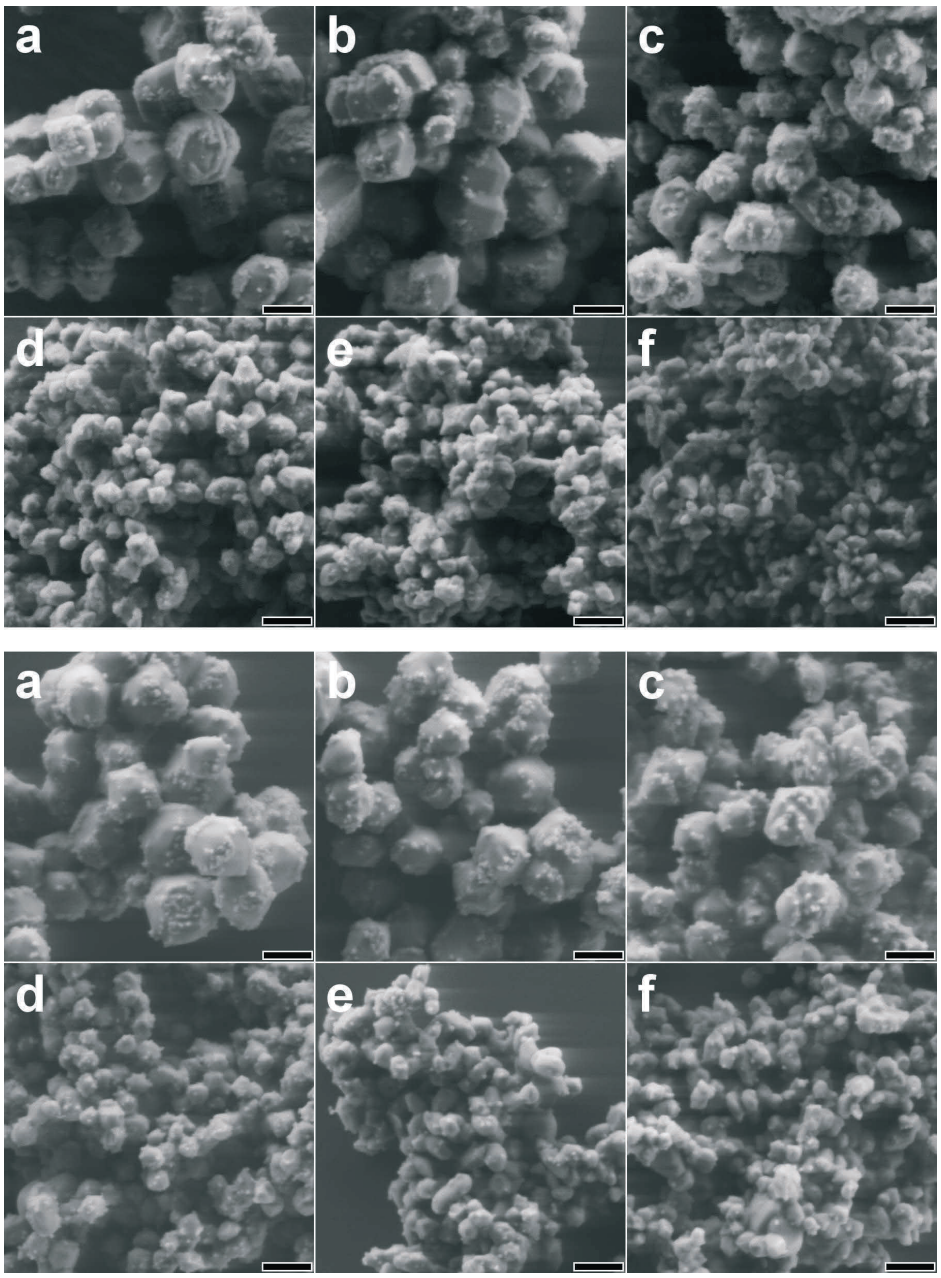

Figure 2.8: Representative SEM images of TiO_2 coated $Bi_{1-x/3}V_{1-x}Mo_xO_4$ nanoparticles (a: 0%, b: 2%, c: 4%, d: 8%, e: 11% and f: 15% Mo content), before (top) and after (bottom) calcination (500°C / 5 h); scale bar = 200 nm.

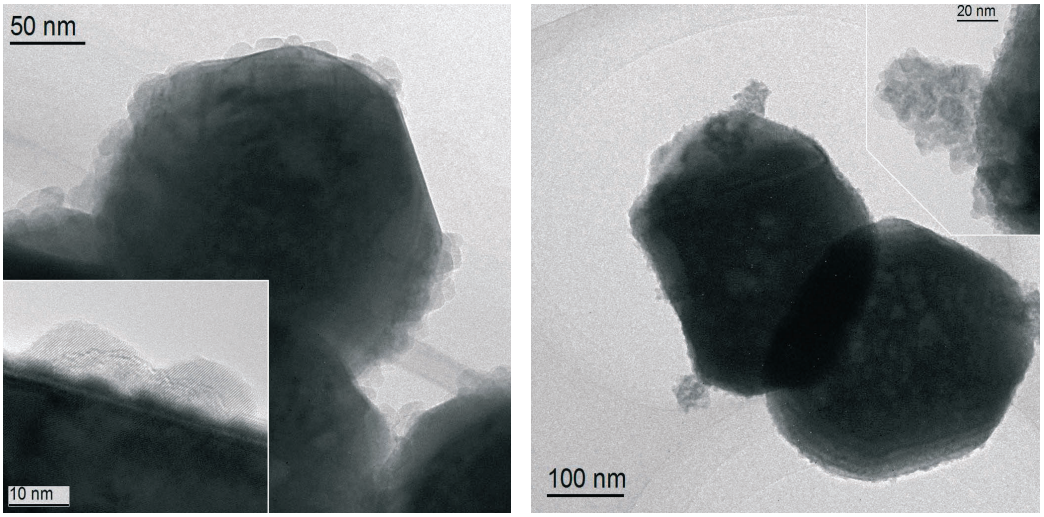

Figure 2.9: HRTEM images of the coated and calcined samples. Left: $BiVO_4$_2% Mo@TiO_2 particles (inset: close-up of TiO_2 coating). Right: $BiVO_4$_2% Mo@SnO_2 particles (inset: close-up of SnO_2 coating).

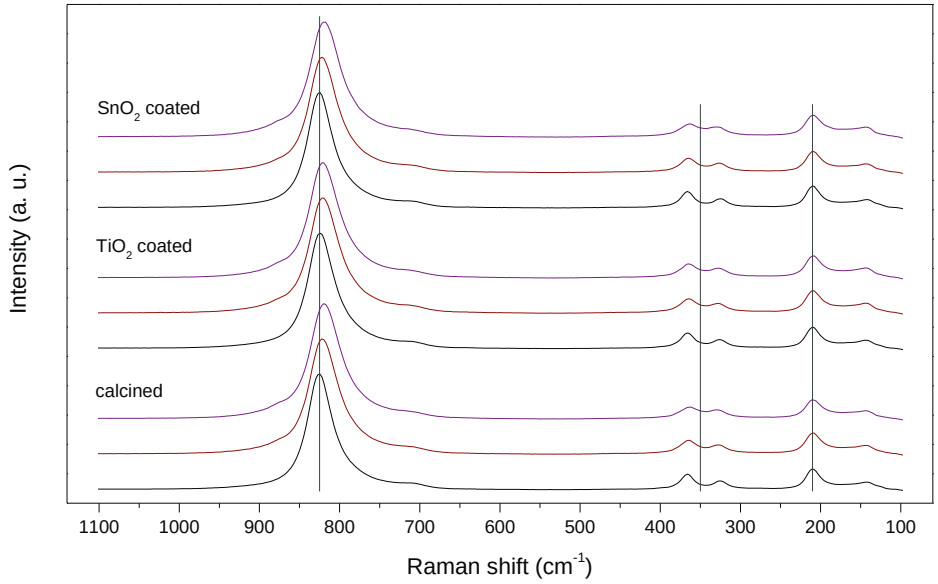

Figure 2.10: Comparison of the Raman spectra of the calcined vs. the TiO_2 and SnO_2 coated and calcined $Bi_{1-x/3}V_{1-x}Mo_xO_4$ ($0 < x < 0.04$) samples.

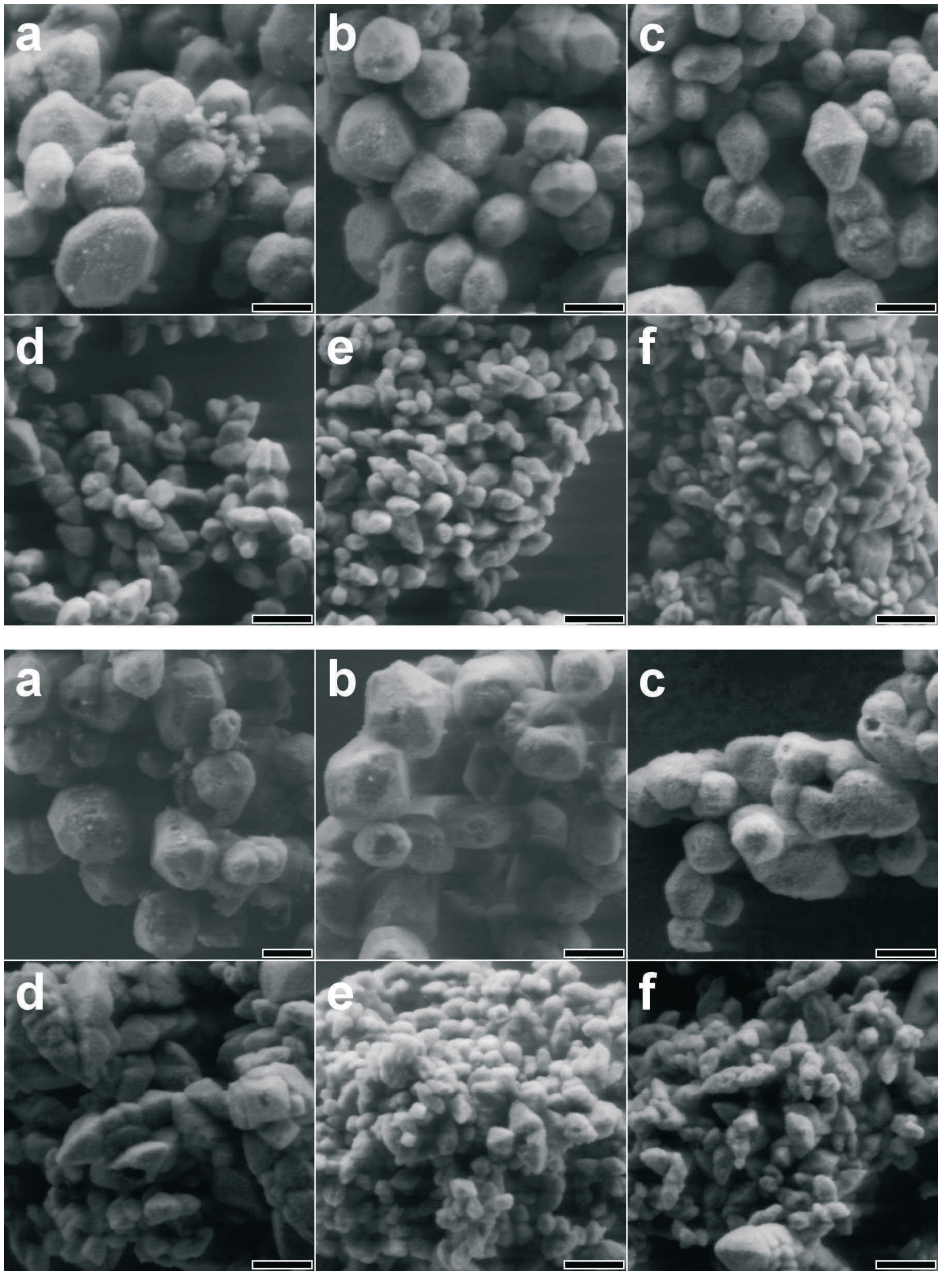

Figure 2.11: Representative SEM images of SnO_2 coated $Bi_{1-x/3}V_{1-x}Mo_xO_4$ nanoparticles (a: 0%, b: 2%, c: 4%, d: 8%, e: 11% and f: 15% Mo content), before (top) and after (bottom) calcination (500°C / 5 h); scale bar = 200 nm.

particle sizes and higher coating densities. In contrast to the TiO_2 heterojunctions, the surface enlargement is partially maintained in the SnO_2-based composites after calcination (Table 2.2). Nevertheless, no indications of SnO_2 were detectable in Raman spectra prior to and after thermal treatment (Figure 2.10) or in the powder diffraction patterns.

The productive influence of both TiO_2 and SnO_2 coating on calcined pristine $BiVO_4$ samples is illustrated in Figure 2.12: the photocatalytic activity in MB degradation is doubled for $BiVO_4@TiO_2$ and $BiVO_4@SnO_2$. The emission spectrum of the blue light source used for visible light irradiation shows very little overlap with the absorption spectrum of MB (Figure 1.8), hence minimizing the possibility of dye sensitizing of TiO_2. Pristine $BiVO_4$, $BiVO_4@TiO_2$ and $BiVO_4@SnO_2$ samples display high catalytic performance in MB degradation, thus confirming the above trend that calcination is not an essential prerequisite for $BiVO_4$-based catalysts (Figures 2.6 and 2.12). Interestingly, however, the high catalytic activity of the $BiVO_4$ heterojunction compounds is maintained upon calcination — other than for pristine $BiVO_4$. Furthermore, thermal treatment significantly improves the performance of the $Bi_{1-x/3}V_{1-x}Mo_xO_4@TiO_2$ materials with molybdenum contents up to 4%. As observed above for the pristine $Bi_{1-x/3}V_{1-x}Mo_xO_4$ series, the calcined $BiVO_4$_2% Mo@TiO_2 and $BiVO_4$_4% Mo@TiO_2 samples display the highest activity and the overall MB decomposition rate decreases again upon further molybdenum incorporation.

SnO_2 coating and calcination deteriorates the photocatalytic performance of the hitherto most active $BiVO_4$_2% Mo and $BiVO_4$_4% Mo members of the solid solution series, indicating that any moderate surface activity and acidity enhancement gained from 2–4 % Mo doping is concealed by the dense SnO_2 layer. Related trends are observed for O_2 production with SnO_2-based heterojunctions (Figure 2.13).

Calcined $BiVO_4$ and as-synthesised $BiVO_4@TiO_2$ display maximum O_2 production rates among the series and their catalytic activity in water oxidation is comparable (Figure 2.13). While hydrothermally synthesised pristine $BiVO_4$ water oxidation catalysts benefit from thermal post-treatment, this is not the case for their $BiVO_4@TiO_2$ heterojunctions. However, $BiVO_4$_2% Mo@TiO_2 performs better in water oxidation after calcination than the as-synthesised composite. This

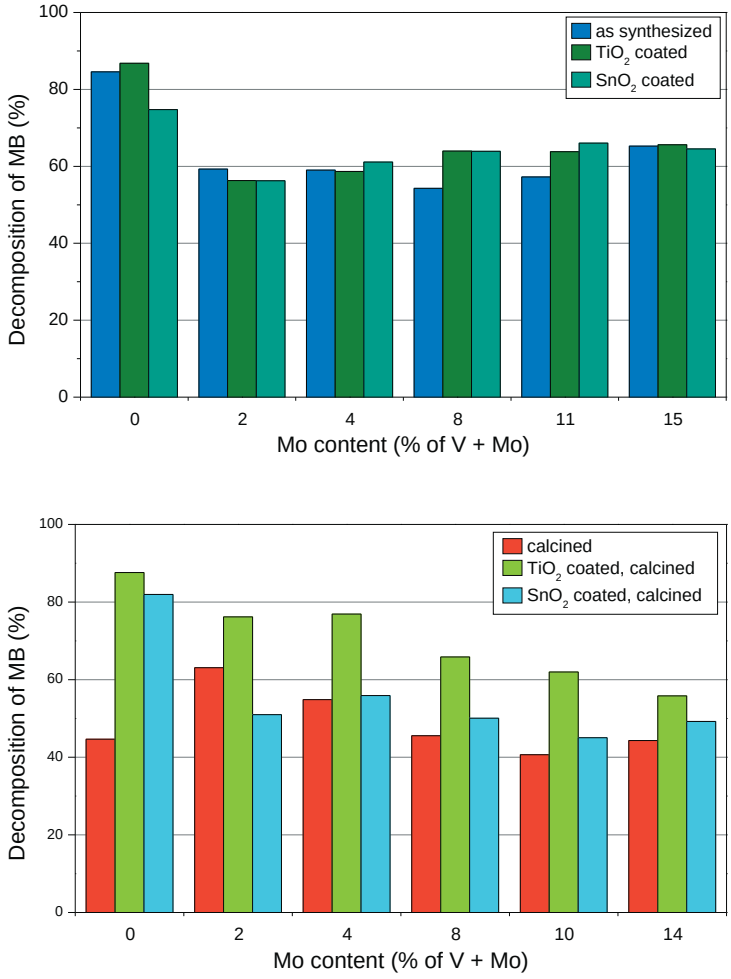

Figure 2.12: Methylene blue degradation with TiO_2- or SnO_2-coated as-synthesised (top) and calcined (bottom) $Bi_{1-x/3}V_{1-x}Mo_xO_4$ ($0 < x < 0.15$) under visible light irradiation (MB degradation after 2 h).

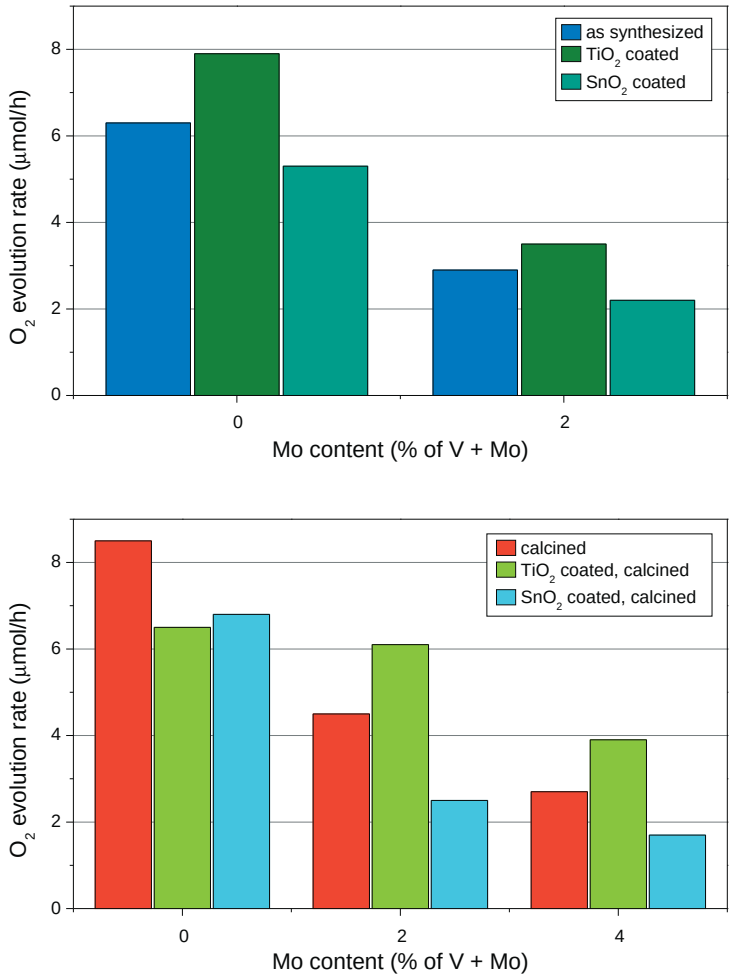

Figure 2.13: Water oxidation with TiO_2- or SnO_2-coated as-synthesised (top) and calcined (bottom) $Bi_{1-x/3}V_{1-x}Mo_xO_4$ ($0 < x < 0.15$) under visible light irradiation.

sums up to the following trends for composites of $BiVO_4$ with TiO_2 and SnO_2:

- MB degradation performance of pristine $BiVO_4$ is only slightly improved by TiO_2 heterojunction formation.
- O_2 evolution with $BiVO_4$ can either be improved through calcination of the pristine material or *via* $BiVO_4$@TiO_2 heterojunctions. Unexpectedly, the combination of calcination and TiO_2 heterojunction formation does not add up to higher O_2 evolution rates for $BiVO_4$-based catalysts.
- The almost equally high O_2 evolution rates of calcined $BiVO_4$@TiO_2 and $BiVO_4$_2% Mo@TiO_2 catalysts suggests that thermal post-treatment of TiO_2 heterojunctions compensates the adverse effects of molybdenum-doping.

2.4 Conclusions

The influence of molybdenum content, particle morphology, surface area and thermal treatment on the photocatalytic activity of hydrothermally synthesised $Bi_{1-x/3}V_{1-x}Mo_xO_4$ ($0 < x < 0.15$) materials in MB degradation and water oxidation, respectively, was investigated. Catalytic activity results are different from previously reported productive effects of molybdenum-doping on $BiVO_4$ catalysts obtained from high temperature methods.[100] Neither calcination nor molybdenum-doping were found to improve the photocatalytic activity of pristine hydrothermally synthesised $BiVO_4$ in MB degradation, whilst calcined molybdenum-free $BiVO_4$ samples showed maximum oxygen production activity. All in all, the adverse effect of molybdenum substitution, i.e. stabilisation of the catalytically less active tetragonal phase of $BiVO_4$, outweighs the benefits of surface acidity and morphology enhancement.

Next, the catalytic tuning potential of TiO_2 and SnO_2 heterojunctions was explored for the above-mentioned photocatalyst series. Pristine $Bi_{1-x/3}V_{1-x}Mo_xO_4$ ($0 < x < 0.15$) samples were subjected to a mild TiO_2 coating process for the deposition of highly crystalline TiO_2 nanoparticles (around 10 nm). SnO_2-coated catalysts were obtained from brief hydrothermal treatment that led to denser overall coatings. As-synthesised $BiVO_4$@TiO_2 performs just slightly better than un-

coated $BiVO_4$ in MB degradation, and the calcined TiO_2-coated samples showed clearly superior performance over the pristine calcined samples despite reduced surface areas after thermal treatment of the composites. This points to the formation of a productive $BiVO_4/TiO_2$ interface for MB decomposition that compensates the drawbacks of calcination. Concerning O_2 evolution, positive influence of TiO_2 coating on $BiVO_4$ catalysts was either observed for as-synthesised $BiVO_4@TiO_2$ samples or for calcined $Bi_{1-x/3}V_{1-x}Mo_xO_4$ (x = 0.02, 0.04)@TiO_2 composites. Finally, SnO_2 coating is only applicable for the activity tuning of calcined $BiVO_4$ photocatalysts for MB degradation whilst it is far less efficient in combination with molybdenum-doping for water oxidation catalysts.

The present systematic investigations demonstrate that the optimisation of multi-component oxide catalysts for wastewater treatment or water oxidation, respectively, requires different strategies. This is due the different pathways of MB decomposition and O_2 production that remain challenging to control. As a result, the net effects of doping, heterojunction formation and thermal post-treatment on a given catalyst are difficult to predict and have to be individually investigated. In the case of hydrothermally synthesised $BiVO_4$ photocatalysts, a compensating effect of TiO_2 coating on the otherwise adverse V/Mo substitution process was found. This points to a complex interplay of doping and heterojunction formation which merits further in-depth investigations and can pave the way to new dual tuning strategies for photocatalysts.

Chapter 3

Morphology Control of $BiVO_4$ Photocatalysts: pH Optimisation vs. Self-organisation

In the previous chapter, mainly "external" approaches to improve the photocatalytic activity of $BiVO_4$ were discussed: the substitution of vanadium by molybdenum on one hand, and on the other hand the formation of junctions with another oxide. A more "intrinsic" approach to improve a photocatalyst would be to enhance its crystallinity and specific surface area, as well as to address the type of exposed crystal facets. For this purpose, hierarchical nanostructures have turned out to be favorable, because they combine reactive nanoscale architectures with high surface areas.[118] However, their synthesis so-far needs to be optimised again for each new system, because profound mechanistic insight into these processes remains difficult to obtain and requires the use of in situ approaches.[119] As a result, even though remarkable progress has been made in the understanding of the underlying principles of self-organisation over the past years,[120] serendipity and self-organisation phenomena play a major role in accessing hierarchically structured materials,

Generally, surface tuning of photocatalysts is performed either via stabilisation of surfaces with optimal catalyst-reactant interactions or through optimisation of their light absorption properties to enhance their performance.[121] Recently, surface etching of colloidal particles has been reported as another promising technique to access otherwise inaccessible surface features.[122] Two fundamentally different approaches in template-assisted syntheses of photocatalysts can be differentiated. "Hard" templates function similar to molds used in industry and shape pure catalytic compounds on their surface, but they are often difficult to remove afterwards. On the other hand, "soft" templates are additives which stabilise certain crystal facets — they are more flexible, whilst incorporation and catalyst poisoning are their major drawbacks. Mesoporous silica (KIT-6) has been used for hard templating of $BiVO_4$,[123] and a wide variety of additives and surfactants has proven useful to bring forward new morphologies of $BiVO_4$

particles: CTAB (cetyltrimethylammonium bromide) for the formation of microspheres,[124,125] ethanolamine or SDBS (sodium dodecyl benzene sulfonate) direct towards platelets,[126,127] and the triblock copolymer P123 ($PEO_{20}PPO_{70}PEO_{20}$) and related compounds assist the growth of star-shaped $BiVO_4$ particles[128].

Due to its facile handling and parameter flexibility hydrothermal synthesis is a prominent method for both template-free and surfactant assisted formation of crystalline oxide materials.[129] The drawback of hydrothermal processes are certain difficulties in synthesis optimisation or upscaling, because small variations of a given conventional protocol often exert a remarkable influence on the particle shape and surface area of the emerging products, thereby deciding about their photocatalytic performance. Especially for pH control in hydrothermal processes and for the introduction of organic templates the optimisation pathway is often not straightforward.[130]

The following study investigated the influence of pH values on the formation of nanostructured $BiVO_4$ in a selected parameter window. In contrast to the results presented in chapter 2, the synthesis is based on a different vanadium precursor, namely NH_4VO_3.[83,131] $BiVO_4$ materials are synthesised under different pH conditions and in presence of additives, and quenching studies serve as basis for the discussion of different formation mechanisms. The dissolution-crystallisation pathway observed under acidic conditions is furthermore selected as a starting point to introduce alkylphosphonates as new phosphorus-based templates for the formation of hierarchically structured $BiVO_4$ architectures. Finally, the materials are compared with respect to their performance in the decomposition of organic model dyes for wastewater treatment and for water oxidation, and the influence of the pH on the decomposition pathways of different organic test dyes is discussed.

3.1 Preparation of the $BiVO_4$ catalysts

3.1.1 Template-free synthesis

In a typical synthesis, $Bi(NO_3)_3{\cdot}5H_2O$ (97 mg, 0.2 mmol) and NH_4VO_3 (23 mg, 0.2 mmol) were dissolved in HNO_3 (0.2 mL, 65% (w/w)) or NaOH (0.2 mL, 6 M), respectively, at room temperature. Under stirring, the Bi solution was slowly added to the V solution and magnetically stirred over night. The slurry was trans-

ferred to a Teflon-lined stainless steel autoclave with a capacity of 15 mL, followed by dilution to an overall volume of 5 mL and adjusting the pH with NaOH (6 M and 0.06 M). The autoclave was maintained at 160 °C for 5 h and subsequently cooled to RT naturally. The precipitate was collected by centrifugation, washed with H_2O (three times, 13 mL) and dried at 80 °C in air.

3.1.2 Template-assisted synthesis

The same procedure as for the template-free synthesis (section 3.1.1) was applied. The surfactants DMMP (dimethyl methylphosphonate) or TBPB (tetrabutyl phosphonium bromide) were added and parameters were adjusted as indicated above prior to hydrothermal treatment. The samples were additionally washed with EtOH followed by a 5 min ultrasonic treatment during work-up. Time-dependent reaction monitoring was performed by quenching the autoclaves in ice-water, followed by quick isolation and work-up of the products as described above.

3.2 Properties of the template-free catalysts

The initial pH value during the synthesis of $BiVO_4$ from VO_4^{3-} and Bi^{3+} precursors significantly influences the morphology and crystal structure of the obtained products. Figure 3.1 displays the phases emerging from pH screening in the range between 1 and 9. Phase pure monoclinic $BiVO_4$ was obtained at pH $\leq$ 4 with increasing crystallinity from pH 1 to 4. Traces of tetragonal $BiVO_4$ appear at pH $>$ 5 and a mixture of all three modifications (monoclinic/tetragonal scheelite and tetragonal zircon types) is obtained for initial pH values $\geq$ 6. Although zircon-type $BiVO_4$ has been reported as a hydrothermal precursor phase that undergoes transformation into the monoclinic form,[125] prolonged reaction times of 12 h did not change the phase relations obtained at pH 9.

The PXRD pattern of $BiVO_4$ synthesised at pH 4 was indexed to a pure monoclinic phase with lattice constants of a = 5.197(4) Å, b = 5.091(7) Å, c = 11.701(7) Å and β = 90.39(7)° that agree well with the reference data for monoclinic scheelite-type $BiVO_4$ (ICDD 014-0688).

The morphology of the as-synthesised $BiVO_4$ samples also depends on the pH of the reaction mixture (Figures 3.3 and 3.2). Whereas spherical agglomerates of

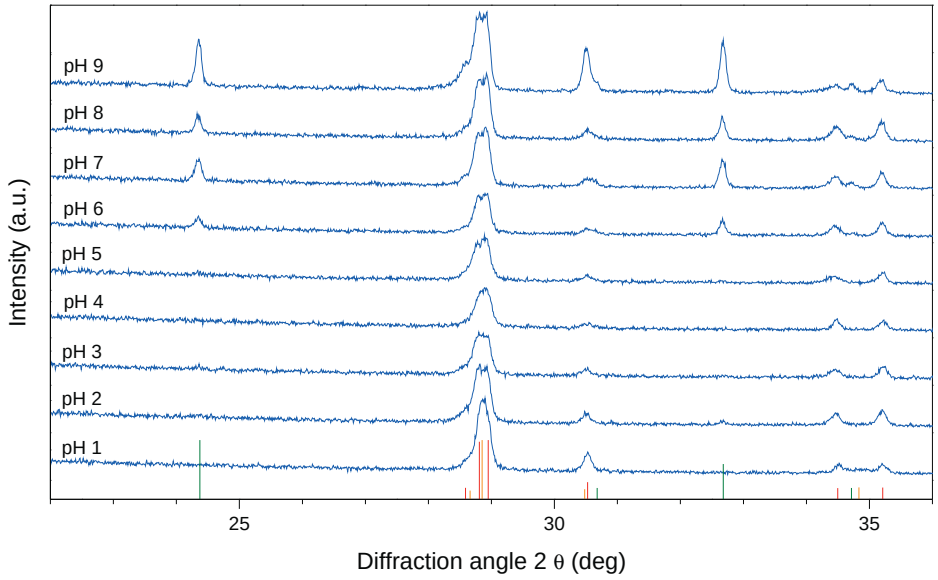

Figure 3.1: PXRD patterns monitoring the pH dependent template-free hydrothermal formation of $BiVO_4$. Red: monoclinic scheelite-type (ICDD 83-1700), orange: tetragonal scheelite-type (ICDD 83-1696), green: tetragonal zircon-type (ICDD 83-1812).

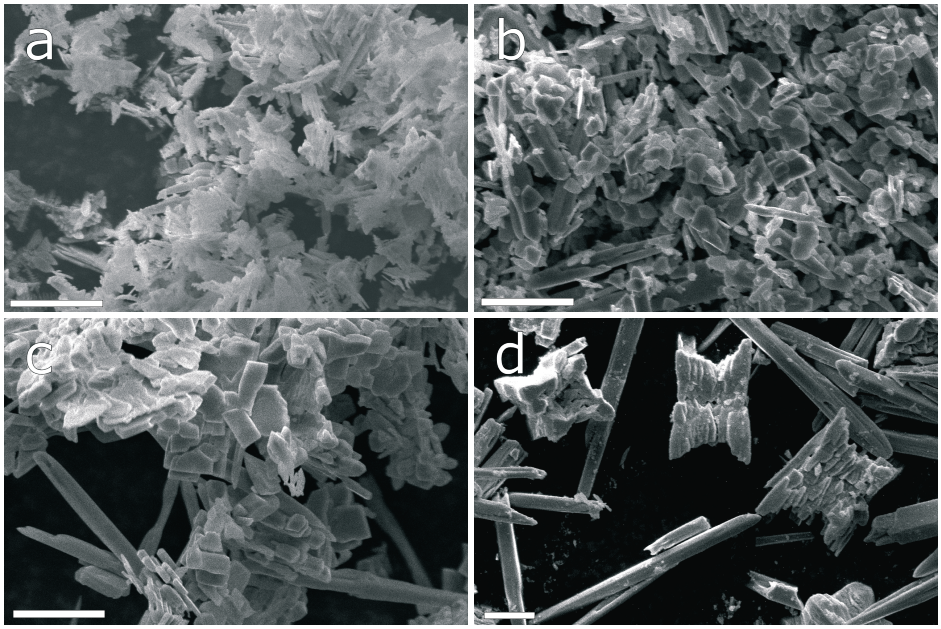

Figure 3.2: Representative SEM images of $BiVO_4$ samples synthesized hydrothermally at different pH values: a: pH 2, b: pH 7, c: pH 8, d: pH 9; scale bar 5 μm.

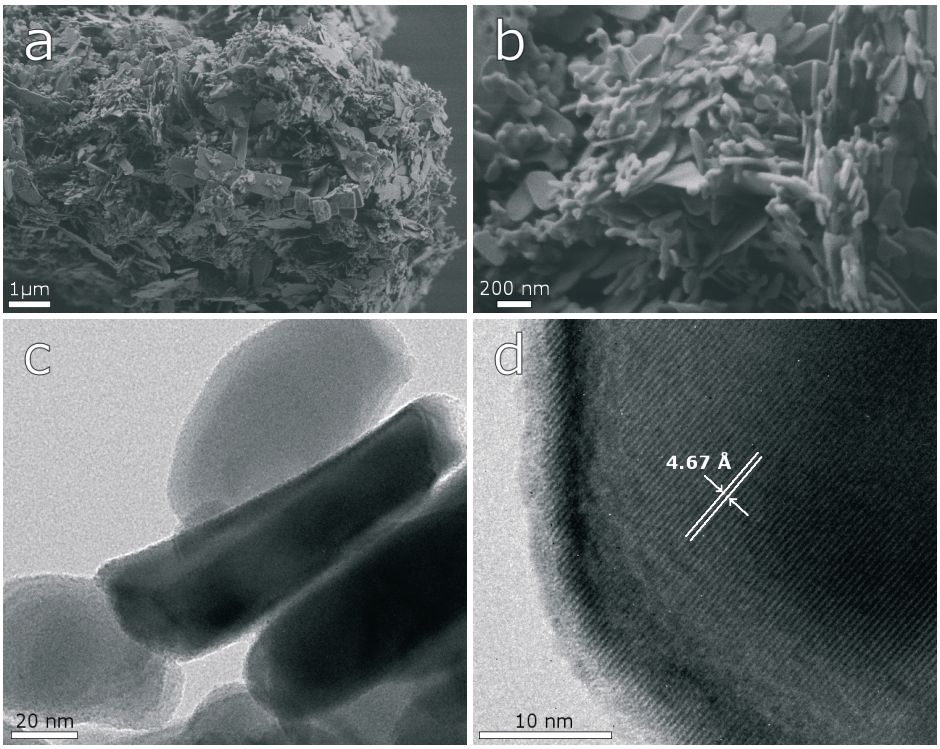

Figure 3.3: Representative SEM (a, b) and TEM (c) images of $BiVO_4$ nanoplatelets synthesised at pH 4 together with HRTEM image (d) of the same material.

$BiVO_4$ platelets with diameters of ca. 5 μm are obtained at pH 1 (Figure 3.6f), dendrite-like shapes are formed at pH 2 (Figure 3.2). Hydrothermal syntheses between pH 4 and 7 afford nanoplatelets with increasing and pH-dependent size (Figures 3.3 and 3.2b). Higher pH values of 8 and 9 favor formation of platelets and their star-shaped aggregates together with characteristic needles of the tetragonal zircon $BiVO_4$ polymorph exhibiting lengths around 10–20 μm (Figure 3.2c, d).

SEM and TEM images of phase pure monoclinic $BiVO_4$ synthesised at pH 4 (Figure 3.3) demonstrate that the surfactant-free route affords platelets that are ca. 20 nm thick with lateral dimensions of 40–500 nm. The BET surface area was determined as 7.4 m^2/g. Although a detailed interpretation of HRTEM images was impossible due to the instability of $BiVO_4$ under the electron beam, the 4.67 Å fringe spacing of the (011) plane could be clearly assigned (Figure 3.3d).

$BiVO_4$ formation processes at pH 4 were quenched after 15 and 45 min re-

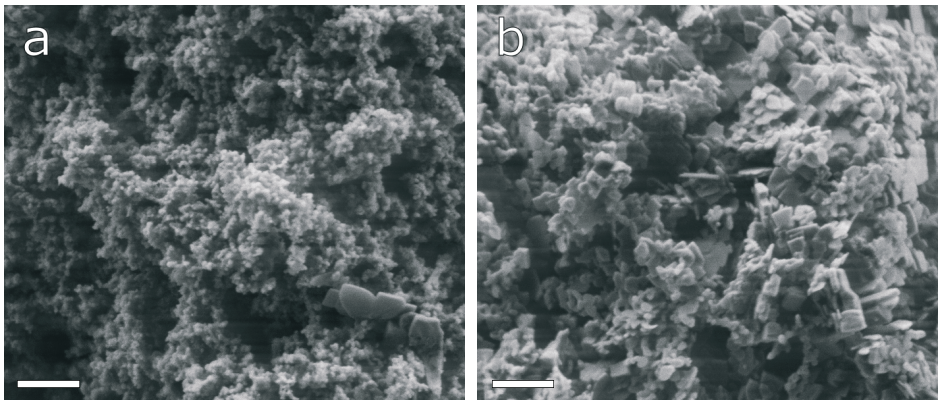

Figure 3.4: Representative SEM images of quenched intermediate products of $BiVO_4$ synthesis at pH 4 after 15 min (a), 45 min (b); scale bar 400 nm.

action time, respectively, and granular aggregates with diameters below 100 nm were obtained after 15 min (Figure 3.4). PXRD patterns show residual amounts of tetragonal zircon $BiVO_4$ at this stage, thereby indicating a fast initial crystallisation process. Prolonged treatment for 45 min enhances both phase purity and particle shape. Given that the precursor solution after the co-precipitation step is highly acidic (pH = 0.8), the formation of a macromolecular amorphous precipitate from BiO^+ and VO_3^- is likely to occur. As the solubility of tetragonal zircon-type $BiVO_4$ is lower under mild acidic conditions than at pH 1, the $BiVO_4$ platelets shown in Figure 3.3 might have been formed via a quick dissolution-recrystallisation process over a short length scale.

The UV/vis reflectance spectra of samples synthesised in the pH 1–9 range are shown in Figure 3.5 and the band gap energies for the respective monoclinic phases are compared. A maximum value of 2.58 eV for the monoclinic $BiVO_4$ phases is observed at pH 4, followed by a decrease to 2.49 eV at pH 9. Such differences in the optical properties can be due to a variety of reasons including quantum confinement effects for particles with dimensions below 50 nm or internal lattice distortions.[132]

Raman spectroscopy investigations of all samples did not display significant shifts of the absorption bands at 826, 720, 366, and 320 cm^{-1} assigned to the asymmetric and symmetric stretching and deformation modes of the VO_4^{3-} tetrahedron.[133] Consequently, the preparative parameters do not exert a significant

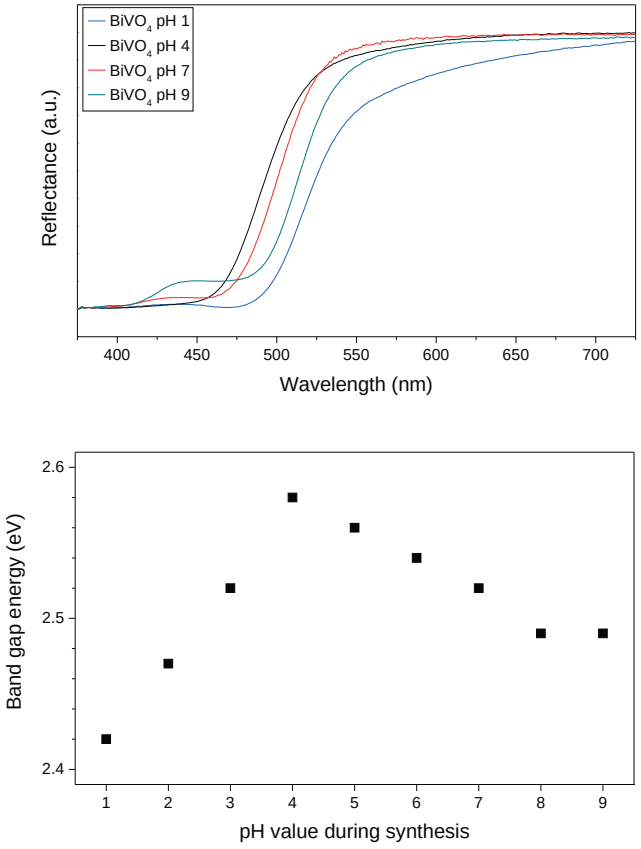

Figure 3.5: Left: Normalised UV/vis reflectance spectra of $BiVO_4$ samples synthesised at different pH values. Right: Band gap values of the monoclinic $BiVO_4$ products as a function of pH value during the hydrothermal synthesis.

influence on the local structure of the $BiVO_4$ materials. Therefore, the blue shift of the band gap is most likely due to the decreasing platelet thickness for $BiVO_4$ (pH 4). Samples synthesised at pH $\geq$ 6 display the characteristic band gap of zircon-type $BiVO_4$ at 428 nm that is formed at higher pH values as a side product (Figure 3.5).

3.3 Properties of the template-assisted catalysts

The above surfactant-free protocol was subsequently used as a starting point for the screening of new phosphorus-containing templates for $BiVO_4$ morphology control. Whereas tetrabutylphosphonium bromide (TBPB) gives access to microscale hierarchical samples under specific conditions (Figure 3.6e), the majority of $BiVO_4$ products did not display enhanced morphologies. Furthermore, the deposition of bromine species on the sample surface was determined from EDX measurements and affected the optical properties through colour change from yellow to dark purple.

While several phosphate derivatives, including different tri- and dialkyl phosphites, neither afforded improved morphologies nor phase pure products, dimethyl methylphosphonate (DMMP) emerged as the best phosphorus-containing surfactant. DMMP provides a variety of $BiVO_4$ particle shapes (Figure 3.6), such as microspheres of hierarchically arranged rectangular crystals and dumbbell-shaped spheroids. Neither morphology nor structure of the $BiVO_4$ products was changed in the temperature range between 120 and 180 °C. The DMMP/metal precursor ratio is more influential: values below 5 afford no special morphologies and ratios above 12 induce an intergrowth of the spherocrystals. The filling volume of the autoclave (for constant reactant vs. surfactant concentrations) was identified as another key reaction parameter: filling levels of 2 and 5 mL in the absence of DMMP led to the formation of spherical microcrystals that are composed of platelets or large crystals, respectively.

The role of DMMP in the growth process was subsequently tracked with time-dependent SEM and PXRD investigations (Figure 3.7) after quenching in ice water (filling level 2 mL, DMMP 1.8 mmol). The primary amorphous precipitate was found to crystallise as a mixture of zircon-type and monoclinic $BiVO_4$

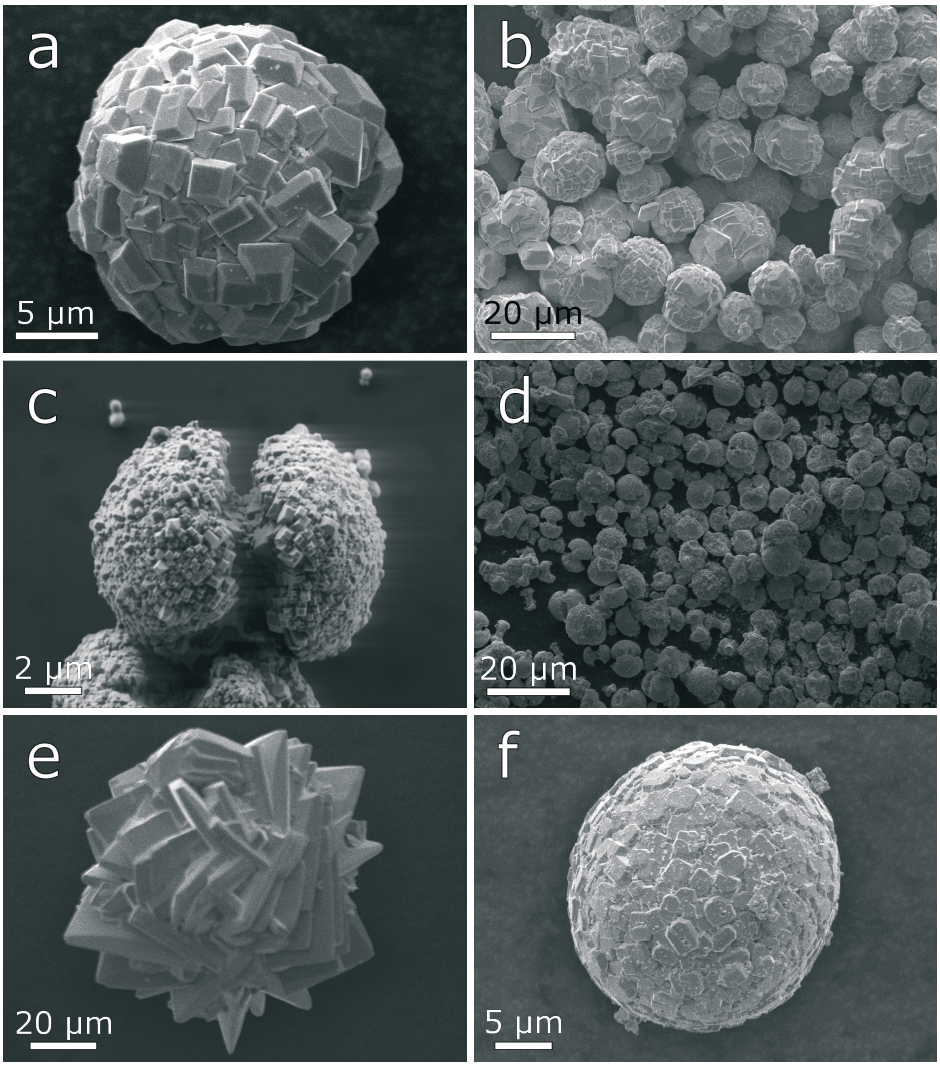

Figure 3.6: Characteristic SEM images displaying the influence of autoclave filling level for the reaction of 0.2 mmol Bi/V precursor with 1.8 mmol DMMP. a & b: 2 mL, c & d: 5 mL, e: 2 mL with 1.8 mmol TBPB instead of DMMP, f: 2 mL without surfactant.

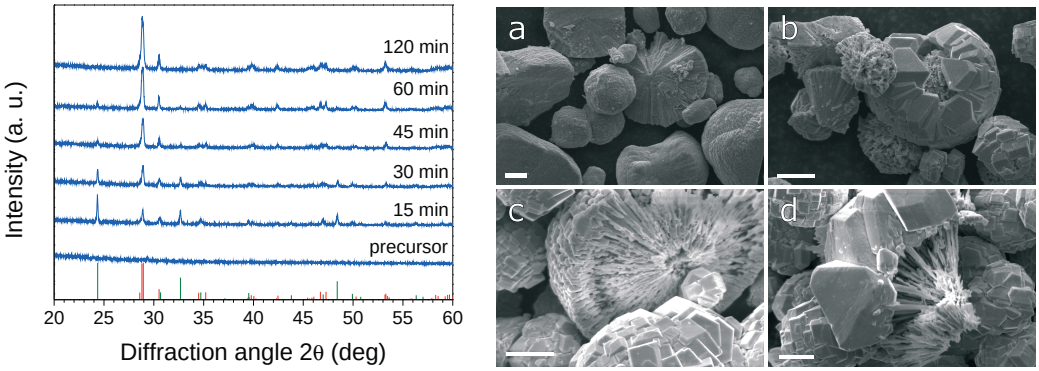

Figure 3.7: Left: PXRD patterns monitoring the time-dependent transformation of zircon-type $BiVO_4$ into the monoclinic form, red: monoclinic scheelite-type (ICDD 83-1700), green: tetragonal zircon-type (ICDD 83-1812). Right: Representative SEM images of samples isolated after (a) 15 min, (b, c) 30 min, and (d) 60 min; scale bar 5 μm.

within 15 min. Phase pure monoclinic $BiVO_4$ was obtained after a reaction time of 120 min. As no additional phases could be detected in the course of the reaction, it proceeds via a gradual transformation of both modifications.

The corresponding morphological transformation is reflected in the SEM images of quenched samples (Figure 3.7). Densely packed microparticles of the zircon/monoclinic phase mixture are observed after 15 min, whereas mesoporous spheres that are partially or completely covered with capped octahedral crystals emerge after 30 min. Their fibrous centers are connected to the outer crystalline parts which cover the spherical samples almost entirely after 60 min reaction time.

Analogous studies on the formation process of dumbbell-shaped $BiVO_4$ particles (higher filling level of 5 mL, 1.8 mmol DMMP) display the presence of nearly phase pure zircon-type $BiVO_4$ after 15 min and slower transformation into monoclinic $BiVO_4$ (Figure 3.8). Firstly, microspheres with a modulated surface are formed together with precursor particles of ca. 2 μm in size (Figure 3.8). They are already pre-structured around a core fragment and the final dumbbell morphology is then achieved through lateral growth of petal-like crystal fragments around the particle core.

Based on PXRD and SEM investigations on quenched samples, different growth mechanisms for the hierarchically structured spherical and dumbbell-shaped $BiVO_4$ morphologies are proposed. Spherical particle formation sets

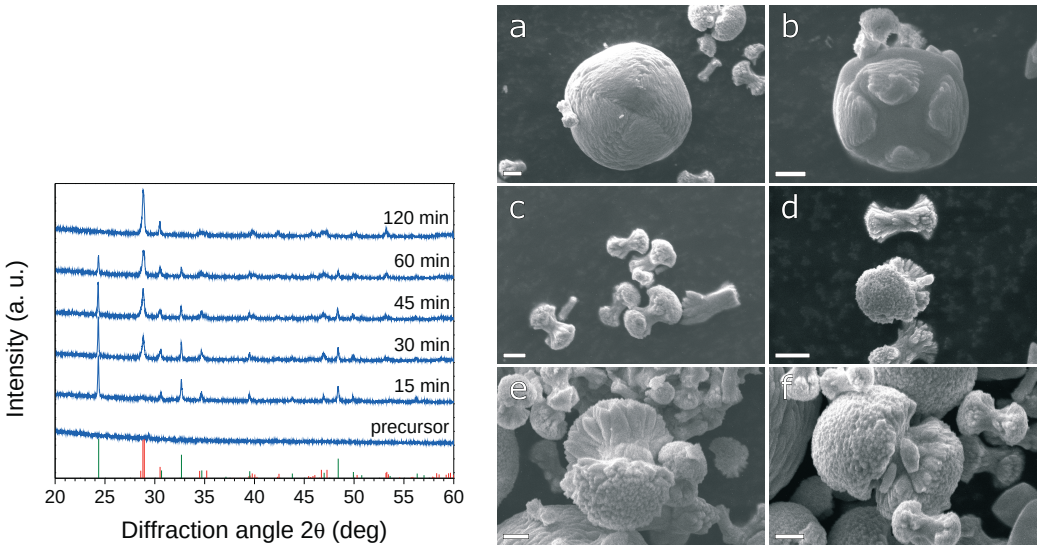

Figure 3.8: Left: PXRD patterns monitoring the formation of $BiVO_4$ dumbbells (red: monoclinic scheelite-type (ICDD 83-1700), green: tetragonal zircon-type (ICDD 83-1812). Right: SEM images monitoring the time-dependent formation of dumbbell-shaped hierarchical $BiVO_4$ architectures after 30 min (a-d) and 45 min (e, f); scale bar 2 μm.

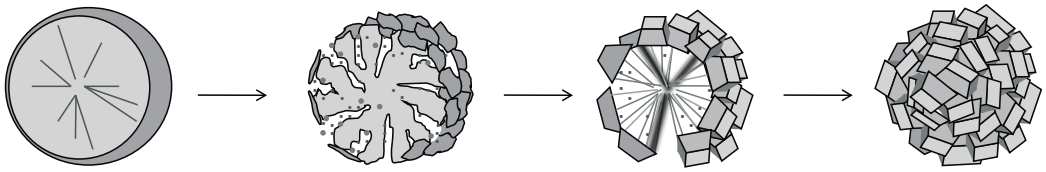

Figure 3.9: Proposed growth mechanism of hierarchically constructed spherical $BiVO_4$ particles.

in with self-assembly of the amorphous precursor and its crystallisation into densely packed zircon-type $BiVO_4$ spheres at the beginning of the hydrothermal treatment. They are converted into spongeous microspheres above a certain temperature/pressure threshold by partial dissolution, followed by a recrystallisation into monoclinic $BiVO_4$ crystals on the surface of the spheres (Figure 3.9). The morphology of the newly formed monoclinic $BiVO_4$ crystals is probably directed by the surfactant. On the other hand, the partial intergrowth of the spherical core with the reconstituted surface might also support a direct local transformation process. Although the detailed role of DMMP is difficult to assign, comparisons with reference samples clearly show that it is essential for the three-dimensional arrangement of the monoclinic $BiVO_4$ subunits (Figure 3.6).

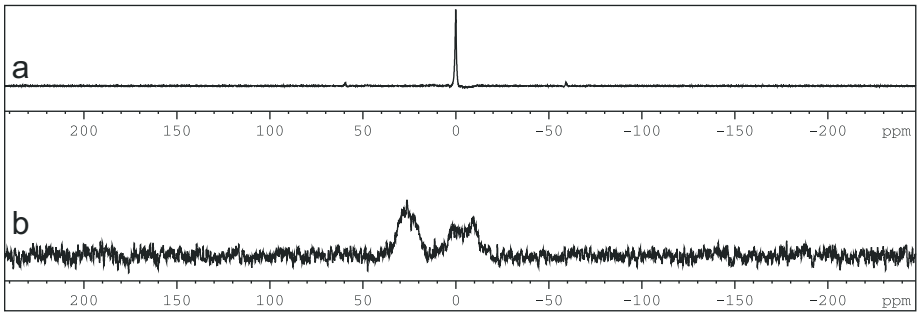

Figure 3.10: ^{31}P MAS-NMR spectra of a: $(NH_4)_3PO_4$ and b: $BiVO_4$ dumbbells.

The different morphological and structural conversions during the formation of dumbbell structured $BiVO_4$ indicate that they grow via a different pathway. Generally, this interesting morphology has been found in different chemical systems under a variety of reaction conditions, e.g. for hydrothermally prepared ZnO[134], for $CaCO_3$ obtained from carbonation[135] and also for fluoroapatite grown from double diffusion crystallisation[136,137]. It is therfore proposed, that the outer shell of initially formed densely packed spheres becomes porous in the course of hydrothermal treatment, accompanied by the decollation of seed crystals. They grow in lateral direction through the attachment of new fragments.

The superior templating properties of DMMP among the phosphorus-containing surfactants are probably due to its stability under hydrothermal conditions. Whereas acid catalyzed hydrolysis and P-O cleavage of trialkyl phosphites into dialkyl hydrogen phosphonates was reported,[138] protonation on the phosphorus is impossible in the case of DMMP and protonation on the phosphor ester moiety is unfavorable as well due to the higher stability of the phosphoryl group[139]. Given that surfactants may affect the photocatalytic performance of the emerging materials, EDX, FT-IR, Raman spectroscopy and elemental analyses were performed. None of the methods showed the presence of significant amounts of organic compounds within the products. Two different phosphate species emerged in MAS-NMR spectroscopy of the dumbbell structures at 0 ppm and 50 ppm (relative to $(NH_4)_3PO_4$), however, only weak signals were obtained after long-time measurements (12 h, Figure 3.10).

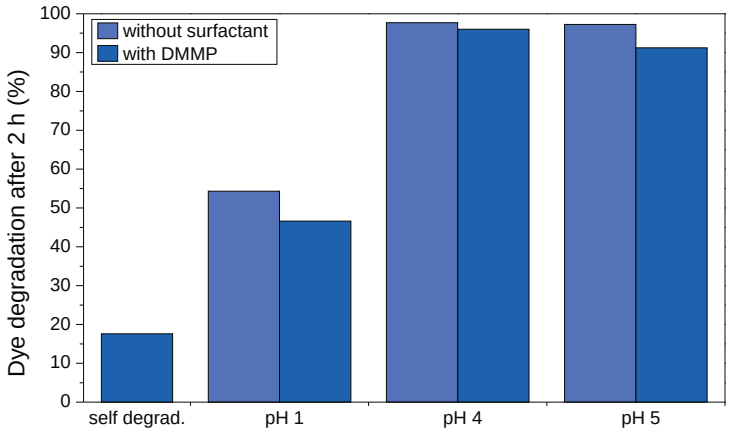

Figure 3.11: Comparison of the MB degradation properties (at pH 7) of $BiVO_4$ catalysts synthesised at different pH values with and without DMMP.

3.4 Photocatalytic activity of $BiVO_4$ nanocatalysts: parameter study

3.4.1 pH value during hydrothermal synthesis

The initial pH value during hydrothermal $BiVO_4$ synthesis does not only influence the morphology, but it also has a significant effect on the photocatalytic activity of the emerging products in the degradation of methylene blue (MB). In acidic media, there is a considerable difference between samples synthesised at pH 1 and those obtained under moderate acidic conditions (pH 4–5), which perform better. Figure 3.11 provides a comparison of the activity of template-free $BiVO_4$ samples and their analogues obtained with DMMP. $BiVO_4$ synthesised in alkaline media (pH 9) is considerably less active in MB degradation

All in all, the initial pH during template-free $BiVO_4$ synthesis should be moderately acidic for maximum photocatalytic activity of the products in MB degradation. Lower pH values around 1 significantly reduce the catalyst performance, probably due to the larger particle sizes that reduce the surface/bulk ratio and give rise to sedimentation effects. The adverse effects of higher pH values are linked to the formation of a mixture of zircon-type and monoclinic polymorphs (Figure 3.1).

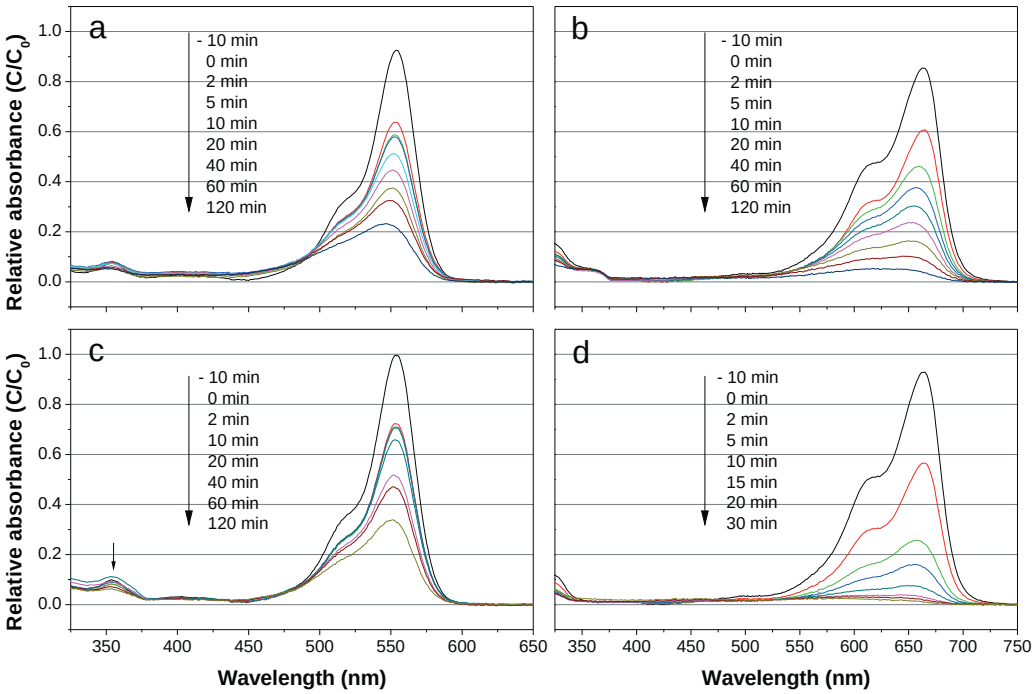

Figure 3.12: Time dependent UV/vis spectra of photocatalytic degradation at different catalytic pH values. a: RhB at pH 7; b: MB at pH 7; c: RhB at pH 9; d: MB at pH 9.

3.4.2 pH value during photocatalytic dye-degradation

Next, the influence of the pH value during photocatalytic MB and RhB degradation was investigated. Pristine MB solutions containing dispersed $BiVO_4$ catalysts display pH values around 5. Figure 3.12 shows dye degradation experiments with dye solutions of different initial pH values. Alkaline solutions promote the catalytic activity of $BiVO_4$ so that complete MB removal under visible light irradiation was observed after 20 min at pH 9, thereby inducing a considerably faster decomposition than observed in the presence of the TiO_2 P25 reference (Degussa). During the reaction, the pH of the catalyst suspension dropped to ca. 7. Interestingly, higher rates for rhodamine B (RhB) degradation were obtained at pH 7 than at pH 9 (Figure 3.12).

The observed optimum catalytic performance at pH 9 can be explained with different hypotheses. Suspensions of small particles are stabilised under alkaline conditions, because aggregation is prevented by electrostatic repulsion. As a consequence, dye absorption is not only favored by negative surface charge of

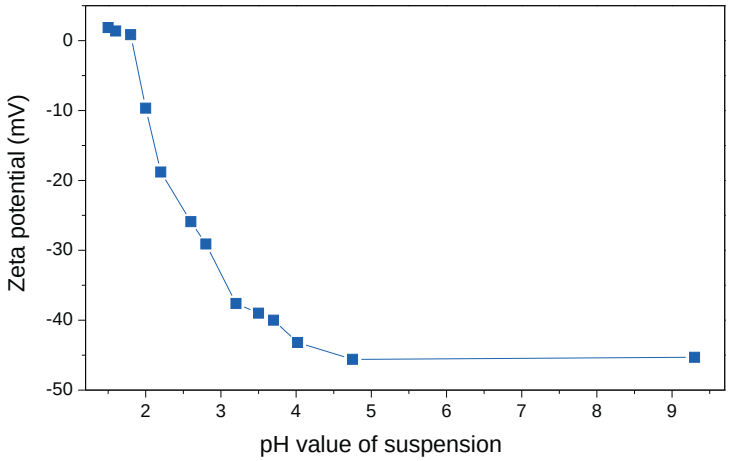

Figure 3.13: Zeta potential measurements of $BiVO_4$ nanoplatelets synthesised at pH 4 without additives.

the particles, but also through maximizing the accessible surface. pH dependent zeta potential measurements show that the isoelectric point of the nanostructured $BiVO_4$ sample synthesised at pH 4 is 1.5 (Figure 3.13). Therefore, the particles are equally negatively charged at pH values ≥ 5 ($\zeta \geq -45$ mV) and additional electrostatic stabilisation of the suspension at higher pH values is not to be expected. However, particles in a solution adjusted to pH 9 did not precipitate within seven days in contrast to precipitation onset within 1 day in suspensions kept at pH 7 or pH 5.

Previous studies showed that two photo-oxidative pathways in the degradation of MB and RhB can be distinguished from the respective time dependent changes of the UV/vis spectra. Whereas the main peak (MB 664 nm, RhB 554 nm) decreases linearly by direct oxidation of the chromophore, de-alkylation causes a blue shift of the main absorbance band (hypsochromic effect).[140,141] Time-dependent UV/vis spectra of MB and RhB decomposition at pH 7 and 9 indicate that de-alkylation is the less important reaction pathway, because no significant shift of the respective absorption bands is observed (Figure 3.12). Decolourisation proceeding by reversible reduction of the cationic dye to its protonated analogue can be prevented by purging the solution constantly with oxygen.[76] Nevertheless, the irregularities within the decreasing absorbance peak of RhB at pH 9 might still originate from such reversible protonation (Figure 3.12c, little arrow). The direct

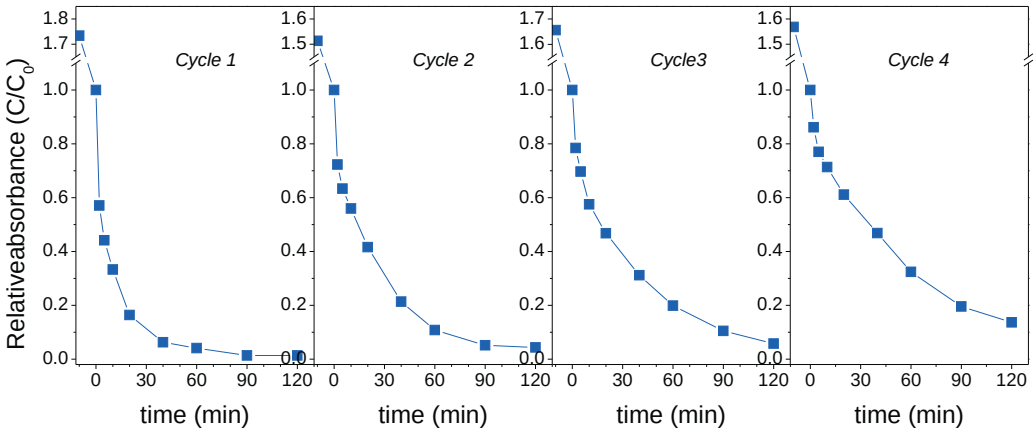

Figure 3.14: $BiVO_4$ MB degradation catalyst recycling experiments (30 mg catalyst synthesised at pH 4).

catalytic oxidation of OH^- is rather ambiguous and controversially discussed.[142] Alternatively, better degradation of the oxidised ($MB^{\cdot+}$) is reported in alkaline solutions that prevent back reduction of the chromophore. This is in line with the observed decrease of the solution pH from 9 to about 7 indicating consumption of hydroxyl ions. The enhanced catalytic performance of $BiVO_4$ in alkaline media can thus be interpreted as a "synergistic process" involving good dispersion of negatively charged nanoparticles, fast processing of the oxidised dye species and other aspects.

3.4.3 Optimal catalyst concentration

Adjusting the optimal catalyst concentration is a compromise between light shielding effects at higher concentrations on the one hand and the presence of more active sites and shorter diffusion pathways on the other hand. Optimal MB degradation rates under the present reaction conditions were obtained for 30–50 mg $BiVO_4$ synthesised at pH 4.

Some experiments regarding the reuseability of the photocatalysts were performed (Figure 3.14) with 30 mg of catalyst which was separated by centrifugation and washed with water and diluted HNO_3 (0.01 mol/L) after each cycle. Color change from yellow to green and decreasing dark adsorption of the catalyst powders after each cycle indicates alterations of the adsorptive properties, although PXRD and electron microscopy investigations showed their structural and mor-

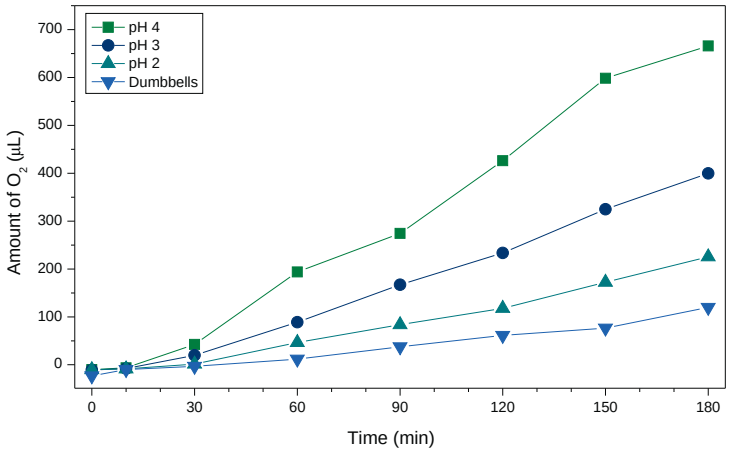

Figure 3.15: Photocatalytic O_2 evolution from aqueous $Fe(NO_3)_3$ solution under visible-light irradiation.

phological stability. Degradation efficiency decreased from 99% (cycle 1) to 86% (cycle 4), but the overall performance is still satisfactory.

3.4.4 O_2 production

A threefold increase of the O_2 production rate is observed when the initial synthesis pH is raised from 2 to 4 (Figure 3.15). This corresponds with the above-mentioned optimum initial pH of 4 for the hydrothermal preparation of $BiVO_4$ photocatalysts for MB degradation. Samples obtained at pH 4 even display a six-fold higher O_2 evolution rate than dumbbell-shaped structures prepared at pH 1 in the presence of DMMP. $BiVO_4$ samples synthesised at pH $\geq$ 5, however, are far less active due to the formation of tetragonal $BiVO_4$ side products.

Interestingly, MB degradation activity and O_2 production efficiency follow the same parameter optimisation trend for the investigated hydrothermal approach to $BiVO_4$, although these two applications usually require different fine-tuning strategies for the catalysts.[117] The sample obtained at pH 4 combines several advantages, such as a large surface area for efficient dye adsorption, high crystallinity and small particle size that suppress the recombination of the photoexcited electron hole pairs and support their diffusion to the surface.

3.5 Conclusions

The initial pH prior to the hydrothermal synthesis of $BiVO_4$ photocatalysts at 160 °C exerts a considerable influence on the phase and morphology of the products. The photocatalytically most active monoclinic scheelite modification of $BiVO_4$ is formed under acidic conditions, whereas higher pH values favor the formation of zircon-type bismuth vanadate products. $BiVO_4$ nanoplatelets with thicknesses around 20 nm, lateral dimensions of 40–500 nm and BET surface areas in the range of 7.4 m^2/g are formed under optimised reaction conditions starting from pH 4. They emerge in a time window between 4 and 15 min, probably from a short-range dissolution-recrystallisation process. Raman spectra indicate that the local structure of the VO_4^{3-} tetrahedra is not influenced by the synthetic conditions but remains unchanged throughout the obtained product range.

Next, the effect of phosphorus-containing templates was screened for the above protocol and dimethyl methylphosphonate (DMMP) emerged as a flexible surfactant to bring forward various nanostructured spherical architectures of monoclinic $BiVO_4$. They can be selectively accessed through hydrothermal parameter adjustment with special emphasis on overall volume and reactant concentrations. Time-dependent monitoring experiments showed that hierarchically structured spheroids and dumbbell-shaped particles are formed via different pathways involving gradual transitions from zircon-type to monoclinic $BiVO_4$. The substructured dumbbell morphology takes longer growth times (ca. 45 min) than the self-organisation of $BiVO_4$ crystallites into microspheres.

Performance tests of all $BiVO_4$ photocatalysts showed that template-free nanoplatelets synthesised at pH 4 exhibit superior performance in both MB decomposition and water oxidation. Alkaline media generally enhance the organic dye decomposition rates of the obtained $BiVO_4$ catalysts due to an interplay of particle dispersion and degradation mechanisms. Cycling experiments demonstrate the stability of the catalyst in alkaline media.

Interestingly, the one-step and template-free synthesis of nanoscale $BiVO_4$ was optimised for water treatment and oxidation in one go, although both photocatalytic processes usually require the tuning of different materials parameters. The results in their entirety illustrate the importance of thorough parameter screen-

ing in template-free and template-directed hydrothermal production of photocatalysts, because minor protocol variations can exert a major effect on the properties and performance of the products.

Chapter 4

Exploring Vanadate Photocatalysts: Prediction vs. Practice

The topic of this chapter will move away from the improvement of previously described photocatalyst materials, aiming towards informed development of new visible-light-active photocatalysts. The predictive design of such materials, however, remains a considerable challenge that keeps attracting worldwide research interest.[35,42,51,143,144] The difficulty of the task arises from the multitude of key performance factors, such as band gaps in the visible light range, position of the band edges, efficient charge separation, small particle size, etc. as well as from the subtle interplay of chemical composition, crystal structure and materials properties.[35,42,144] The introduction of *p*-block elements into oxide-based photocatalysts was recently proposed as a new and promising strategy to enhance their charge carrier mobilities via a reduction of the *d* state contribution to the conduction band.[49] This presents a new opportunity for the targeted optimisation of this important parameter for photocatalytic materials by conducting comprehensive experimental and theoretical studies.

The previous work on $BiVO_4$ (cf. chapters 2 and 3) and $InVO_4$[145] were inspirational to investigate a series of ternary vanadates with visible-light absorbance, namely: $NbVO_5$, $Nb_{10.7}V_{2.38}O_{32.7}$, $VOPO_4$, and ZnV_2O_6. To round off the comparison of experimental and theoretical concepts, $TaVO_5$ and $Zn_2V_2O_7$ with absorption edges towards the UV range were furthermore included. The results of density-functional theory (DFT) calculations for all samples was compared with their respective photocatalytic activity.

The equi-structural compounds $NbVO_5$ and $TaVO_5$[146–148] were found to exhibit negative thermal expansion up to 600 °C[149,150] and were tested as electrode materials for lithium ion batteries.[151,152] Furthermore the application potential of $NbVO_5$ as oxidation catalyst for organic transformations was studied,[153,154] while no reports of photocatalytic investigations with neither of the compounds could be found. The rather complex crystal structure of $Nb_{10.7}V_{2.38}O_{32.7}$ has been fully uncovered only recently,[155,156] and its properties were investigated with respect to

Li^+ and Na^+ intercalation, thermal O_2 release and catalytic oxidation of organic compounds.[157] $VOPO_4$ exists in various modifications, among which the α- and the β-forms have attracted most research attention, i.e. both have been tested as electrode materials in lithium ion batteries[158–160] and as catalysts for selective oxidation reactions[161–163]. Furthermore, layered α-$VOPO_4$ is well-known as a precursor material to intercalation compounds.[164,165] ZnV_2O_6 was investigated as a battery electrode material[166] and for catalytic oxidation of organic compounds[167] Not much is known about application-related materials properties of $Zn_2V_2O_7$, which only recently has been investigated for lithium intercalation.[168]

In the following, DFT calculations on the selected vanadate series as well as on the reference photocatalysts $BiVO_4$ (cf. chapter 3) and Ag_3PO_4[53] are compared. Subsequently, the computational trends are correlated with the photocatalytic performance of the respective materials under standard conditions. Finally, these comparisons are discussed, and guidelines for the application of DFT calculations in future photocatalyst screening are proposed.

4.1 DFT calculations

4.1.1 Calculation parameters

Prior to calculations, structural parameters of the target materials were obtained from refinement of powder X-ray diffraction (PXRD) data using the Reflex module of the Accelrys Materials Studio package. Calculations were performed with the CASTEP program of Materials Studio, which is based on density-functional theory (DFT).[169] Unless otherwise mentioned, experimentally determined structural parameters (lattice and fractional coordinates) were not further electronically optimised for the calculations. Gradient-corrected functionals according to Perdew, Burke and Ernzerhof (GGA-PBE)[170] and ultra-soft pseudo-potentials were applied. Geometry optimisation calculations were done using GGA-PBE functionals with the dispersion correction according to Tkatchenko and Scheffler (TS), if applicable.[171] The following convergence criteria were applied: energy: $5{\cdot}10^{-6}$ eV/atom, max. force: 0.01 eV/Å, max. stress: 0.02 GPa, max. displacement: $5{\cdot}10^{-4}$ Å. Unfortunately, for several elements, including Bi, Nb and Ta, the TS correction is not implemented in the Materials Studio program package. For

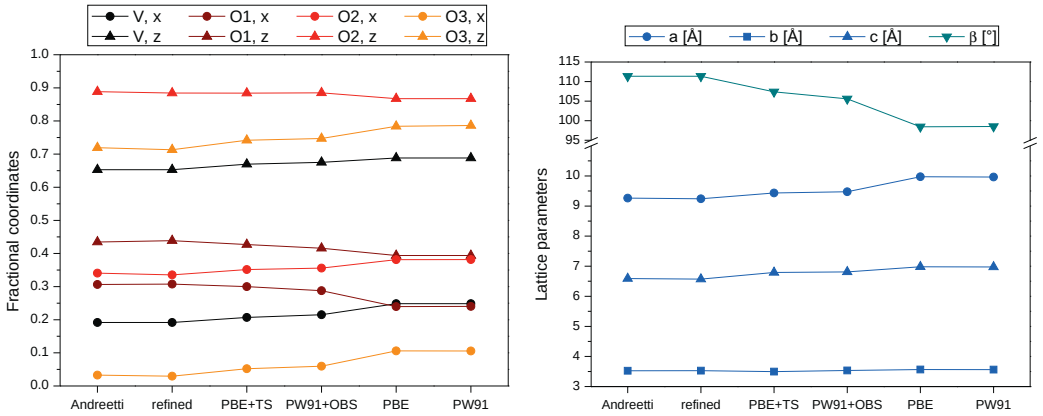

Figure 4.1: Comparison of the structural parameters of ZnV_2O_6: (1) for the structure motif published by Adreetti *et al.*[174], (2) for the refined experimental structure and (3) for the structure optimised with different functionals and with or without dispersion correction. Zn is positioned in the origin (0,0,0), and the y-component of the fractional coordinates of all other atoms equals zero.

geometry optimisation of $BiVO_4$, functionals derived by Perdew and Wang with the dispersion correction established by Ortmann, Bechstedt, and Schmidt were used (GGA-PW91-OBS).[172,173] As shown in Figures 4.1 and 4.2, the different functionals lead to comparable results. The large difference between optimisation with/without dispersion correction can be explained by a "delamination" of the layers when the long-range interactions are neglected. Whereas TS corrections afford better results than OBS, the latter is still preferable over uncorrected calculations. An energy cut-off of 380 eV was used for all calculations, further details on the crystal structures and settings used for individual calculations are given in Table 4.1.

Fractional *d* state contribution to the total density of states (DOS) were calculated from the integrated DOS close the respective band edge; integrations were done over a range of 0.5 eV (Table 4.2).

Exact positions of the valence band maximum and the conduction band minimum, respectively, were required for determination of the effective mass of charge carriers. They were determined from a series of subsequently finer grids of points in k-space, followed by mapping the energy of the respective bands versus the position in k-space. Finally, the effective mass of the charge carriers was obtained from a parabolic fit of the energy surface along the extreme directions of the sur-

Table 4.1: Overview over the parameters used for the DFT calculations for the different compounds. The last two columns indicate modifications of the lattice parameters with respect to ICSD data by either refinement of experimental data or by structure optimisation, in combination with the k-point set used for self-consistent electronic minimisations.

Compound	ICSD / Ref.	S.G.	Lattice parameters (Å or deg)	Mod.	k-point set
Ag_3PO_4	201361 [175]	$P\bar{4}3m$	6.011(1)	No	4×4×4
$BiVO_4$	100604 [176]	*I2/b*	5.198(1), 5.091(1), 11.697(1) γ = 90.399(1)	Ref.	5×5×2
$NbVO_5$	109175 [177]	*$P2_1/n$ $2_1/m$ $2_1/a$*	11.875(1), 5.524(1), 6.926(1)	Ref.	2×5×4
$Nb_{10.7}V_{2.38}O_{32.7}$	420781 [156]	*C2/m 2/m 2/m*	17.345(1), 17.695(1), 3.975(1)	Ref.	1×1×2
$TaVO_5$	202762 [148]	*$P2_1/n$ $2_1/m$ $2_1/a$*	11.867(1), 5.519(1), 6.938(1)	Ref.	2×5×4
α_1-$VOPO_4$	108983 [178]	*P4/n*	6.20(1), 6.20(1), 4.11(1)	No	4×4×6
α-$VOPO_4$	*see α_1 & α_2*	*P4/n*	6.207(1), 6.207(1), 4.318(1)	Opt.	4×4×6
α_2-$VOPO_4$	77598 [178]	*P4/n*	6.014(7), 6.014(7), 4.434(2)	No	4×4×6
β-$VOPO_4$	9413 [179]	*$P2_1/n$ $2_1/m$ $2_1/a$*	7.790(1), 6.136(1), 6.974(1)	Ref.	3×4×4
ZnV_2O_6	30880 [174]	*C2/m*	9.243(1), 3.528(1), 6.572(1) β = 111.354(1)	Ref.	3×7×4
$Zn_2V_2O_7$	2886 [180]	*C2/c*	7.427(1), 8.327(1), 10.089(1) β = 111.297(1)	Ref.	4×3×3

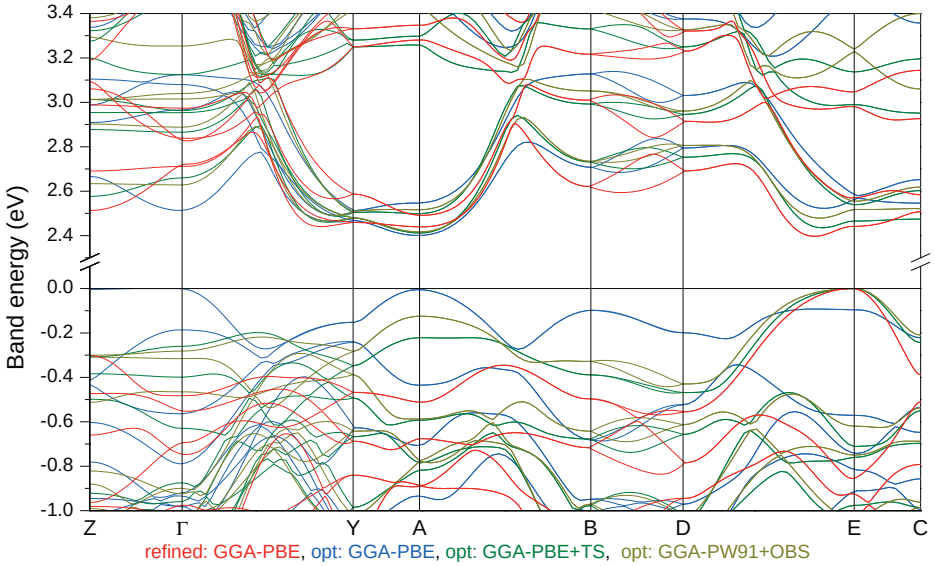

Figure 4.2: Comparison of the band structure of ZnV_2O_6 calculated for the refined structure and for the structure model optimised with different functionals (with and without dispersion correction).

Table 4.2: Calculated contributions of *d* states to the upper part of the valence band and lower part of the conduction band for the different compounds. Contributions were considered over a range of 0.5 eV with respect to the band edge and are indicated in percent.

Compound	upper VB	lower CB
Ag_3PO_4	48	9
$BiVO_4$	1	69
$NbVO_5$	1	92
$TaVO_5$	1	93
α_1-$VOPO_4$	1	77
α-$VOPO_4$	1	77
α_2-$VOPO_4$	6	71
β-$VOPO_4$	2	93
ZnV_2O_6	6	76
$Zn_2V_2O_7$	12	71

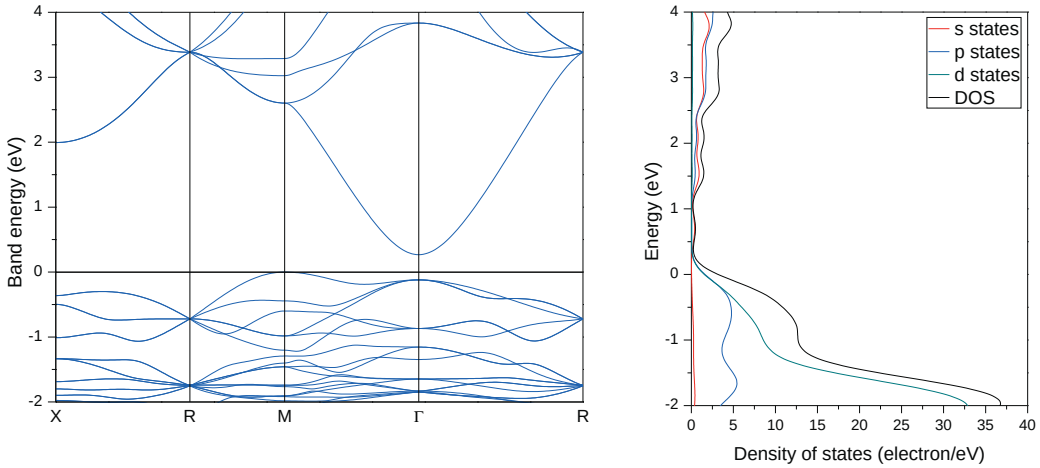

Figure 4.3: Band structure of Ag_3PO_4 close to the band gap (left) and corresponding density of states (right).

faces of equal energy around the extrema.

4.1.2 Ag_3PO_4

Figure 4.3 shows the band structure and density of states (DOS) for Ag_3PO_4, and the crystal structure along with the isosurfaces of the valence and conduction band edges are displayed in Figure 4.5. In line with preceding studies,[49] the conduction band was found to be highly delocalised (Figure 4.3). The partial density of states indicates that it is mainly constituted by *s* and *p* states of silver and oxygen with a minor phosphorus contribution, while the valence band consists of oxygen *p* and silver *d* states (Table 4.2). The band structure shows an indirect band gap (M to Γ) of 0.27 eV which is rather low in comparison with the experimental value (Table 4.10). While the LDA+U formalism has been shown to result in a more accurate value, the overall band shape remained unaffected.[49] Generally, the underestimation of band gap values is a well-known issue associated with DFT calculations.[181] The effective masses of the charge carriers (Table 4.3) indicate a high mobility of the activated electrons in the conduction band and only moderate mobility of the valence band holes.

Table 4.3: Effective masses of charge carriers in the conduction band (CB) and the valence band (VB) of Ag_3PO_4 and $BiVO_4$. The values are indicated as effective masses (e_m^*/e_m).

Ag_3PO_4			
VB (h^+)		VB (e^-)	
(100)	1.89	(100)	0.40
(010)	1.89	(010)	0.40
(001)	1.10	(001)	0.40
$BiVO_4$			
VB (h^+)		VB (e^-)	
(100)	1.13	(100)	2.64
(010)	1.39	($1\bar{1}0$)	0.87
(001)	7.94	(001)	38.1

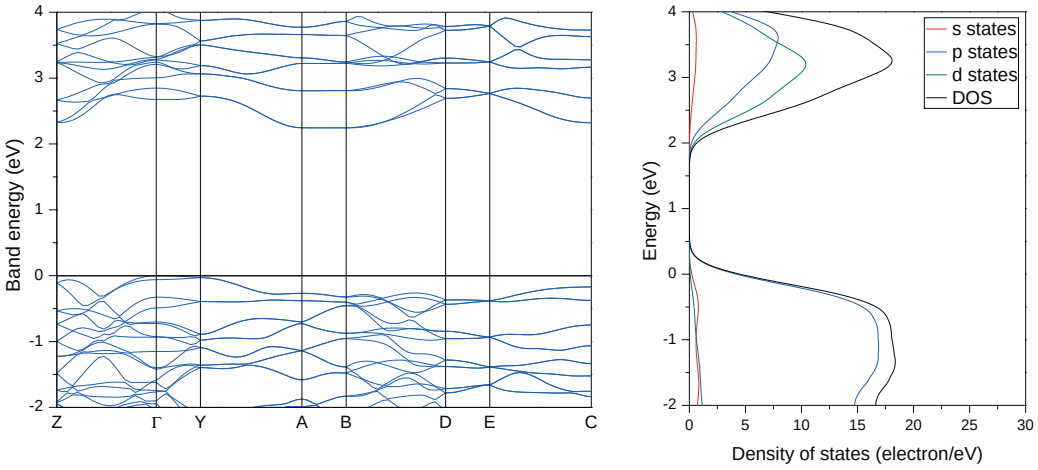

Figure 4.4: Band structure of $BiVO_4$ close to the band gap (left) and corresponding density of states (right).

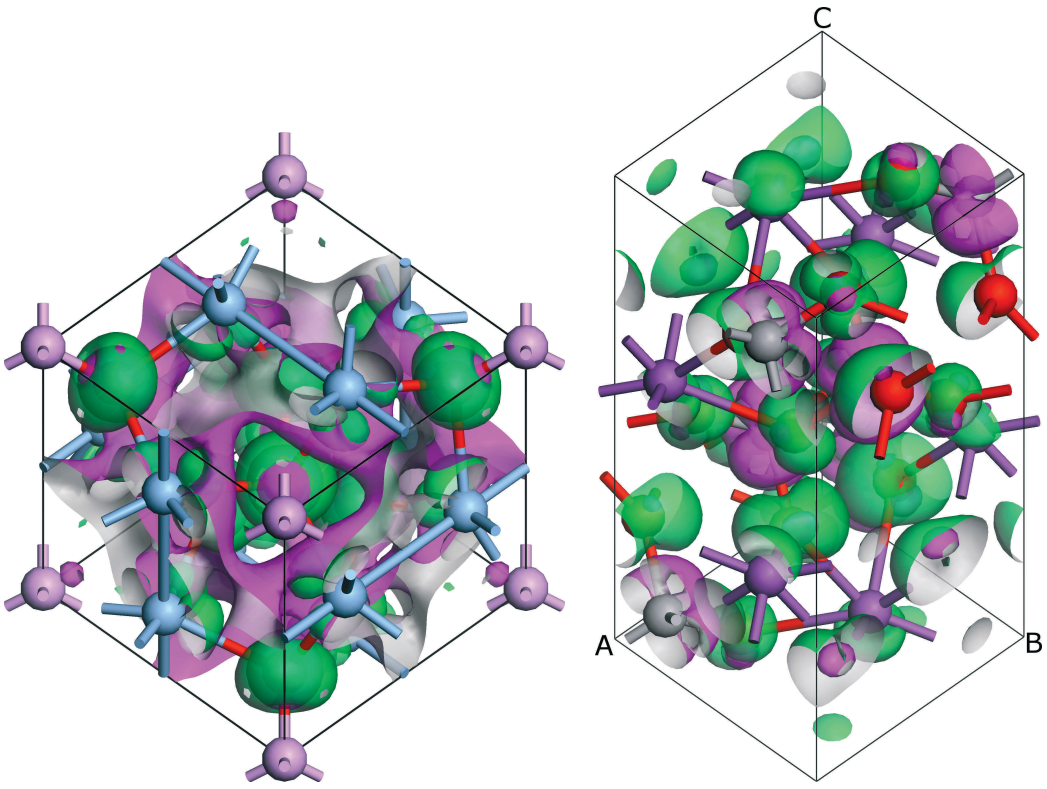

Figure 4.5: Crystal structures of cubic Ag_3PO_4 (left) and monoclinic $BiVO_4$ (right) with isosurfaces of the highest states of the valence band (green) and lowest states of the conduction band (pink) displayed (isovalue: 0.01); red: O, violet: P, light blue: Ag, violet: Bi, grey: V.

Table 4.4: Lattice parameters of the different structure refinements of monoclinic $BiVO_4$ (cf. Figure 4.6). Optimisation was done using the PW91 functionals with OBS correction.

	Sleight-1979 refined	Sleight-1979 ICSD 100604	Sleight-1979 optimised	Liu-1983 ICSD 33243	Liu-1983 optimised
a [Å]	5.198(1)	5.195(1)	5.131	5.197	5.131
b [Å]	5.091(1)	5.094(1)	5.129	5.096	5.129
c [Å]	11.697(3)	11.705(2)	11.586	11.702	11.585
γ [°]	90.399(1)	90.383(1)	90.010	90.400	90.004

4.1.3 $BiVO_4$, $NbVO_5$, $Nb_{10.7}V_{2.38}O_{32.7}$, and $TaVO_5$

The top of the valence band of orthorhombic $BiVO_4$ consists mainly of oxygen *p* orbitals with a minor contribution of bismuth *s* orbitals, while vanadium *d* states are the main constituents of the conduction band with oxygen *p* states contributing considerably less to the DOS (Figure 4.4, Table 4.2). Figure 4.5 displays the crystal structure of $BiVO_4$ along with the isosurfaces of the VB and CB edges. These results are in agreement with previous studies.[182] Table 4.3 displays the effective masses of the charge carriers in conduction and valence band of $BiVO_4$, indicating a moderate to low mobility of the holes in the valence band, while the conduction band exhibits a preferred direction of high mobility. Band structure calculations reveal the presence of an indirect band gap (Γ to B) of 2.24 eV (Figure 4.4), and the present results differ from preceding investigations.[183–185]

Whereas previous calculations showed the presence of a direct or quasi-direct band gap, the approach presented here clearly points to an indirect band gap. This is probably due to different calculation set-ups: the present calculations are based on a refined crystal structure (PXRD data), while all previous reports utilised only electronically optimised structures. A synopsis of calculation results obtained with our refined structure, the unrefined structure and the structural models used by previous authors (Figure 4.6 and Table 4.4) shows that the band edge positions of $BiVO_4$ are very sensitive towards changes of the lattice parameters, thereby demonstrating the advantage of using a refined structure over electronically optimised starting models.

Note that the equivalent body centred setting for $BiVO_4$ in our case in contrast to *c* centred settings and reduced cells used in the preceding studies should not

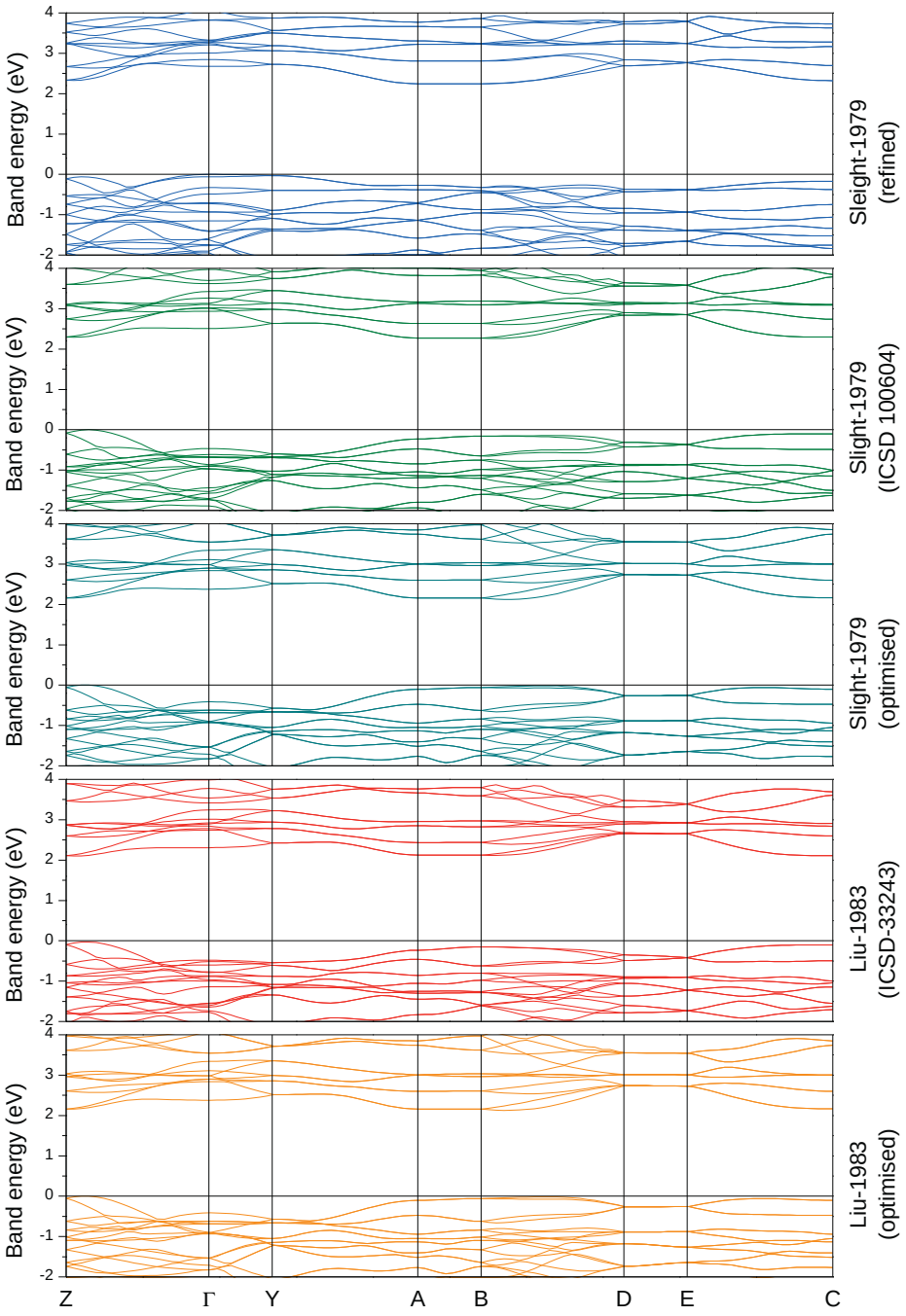

Figure 4.6: Comparison of the calculated band structures for different monoclinic $BiVO_4$ unit cells. The refined structure used in the present work (as shown in Figure 4.4) is based on the structural data of Sleight *et al.*.[176] Optimisation was done using the PW91 functionals with OBS correction.

Table 4.5: Comparison of the lattice parameters and fractional coordinates of the atoms of the *c* centred structures used in the present study and in previous works.

	this work	Zhao-2011 [184]	Park-2011 [185]	Walsh-2009 [183]
a [Å]	7.251	7.224	7.285	7.253
b [Å]	11.697	11.522	11.763	11.702
c [Å]	5.091	5.108	5.123	5.096
β [°]	134.203	135.003	134.180	134.230
Bi	0.000/0.366/0.250	0.000/0.125/0.750	—	—
V	0.000/0.128/0.750	0.000/0.375/0.250	—	—
O1	0.132/0.224/0.637	0.250/0.045/0.359	—	—
O2	0.236/0.056/0.117	0.359/0.205/0.806	—	—

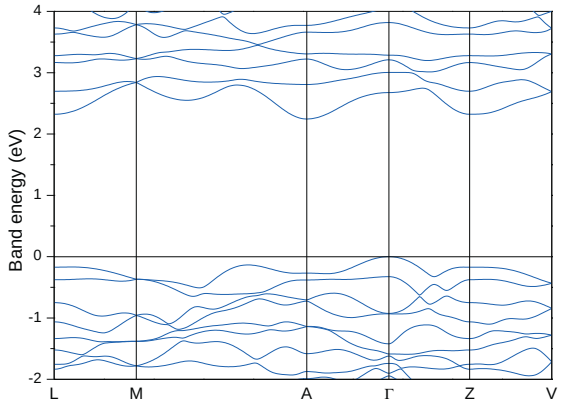

Figure 4.7: Band structure calculated for the reduced cell data of the refined $BiVO_4$ structure.

influence the results (cf. comparison of lattice parameters including data for the transformed refined structure in Table 4.5). Figure 4.7 shows the band structure resulting from reduced cell data for the refined structure of $BiVO_4$, displaying an indirect BG (Γ to A, 2.24 eV).

Band structure calculations point to an indirect band gap (T to Γ) of 1.99 eV for $NbVO_5$ (Figure 4.8). The top of the valence band consists almost exclusively of oxygen *p* orbitals while the bottom of the conduction band consists mainly of the *d* states of niobium and vanadium with a minor contribution of oxygen *p* states (Table 4.2, Figure 4.11). According to the calculated effective charge carries masses (Table 4.6), the holes in the valence band are less mobile, while the electrons in the conduction band display high mobility.

Several crystallographic positions in the structural model of $Nb_{10.7}V_{2.38}O_{32.7}$

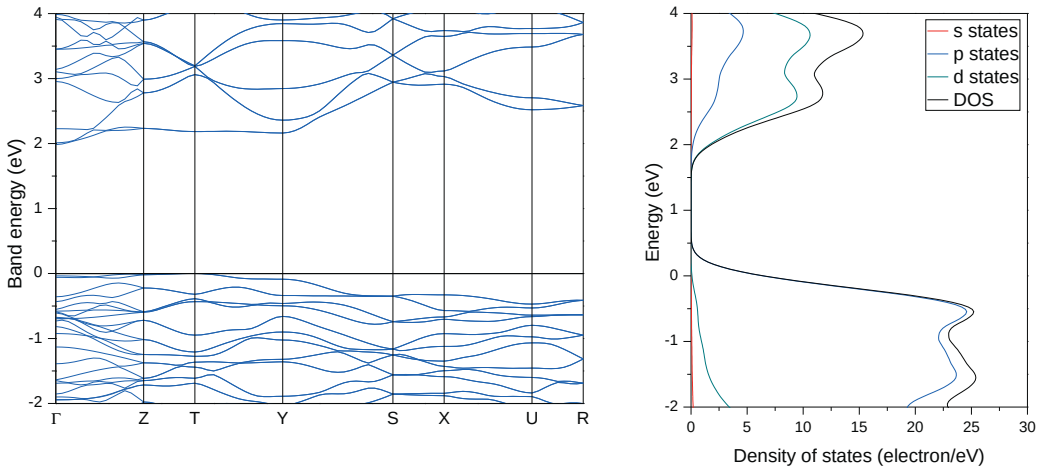

Figure 4.8: Band structure of $NbVO_5$ close to the band gap (left) and corresponding density of states (right).

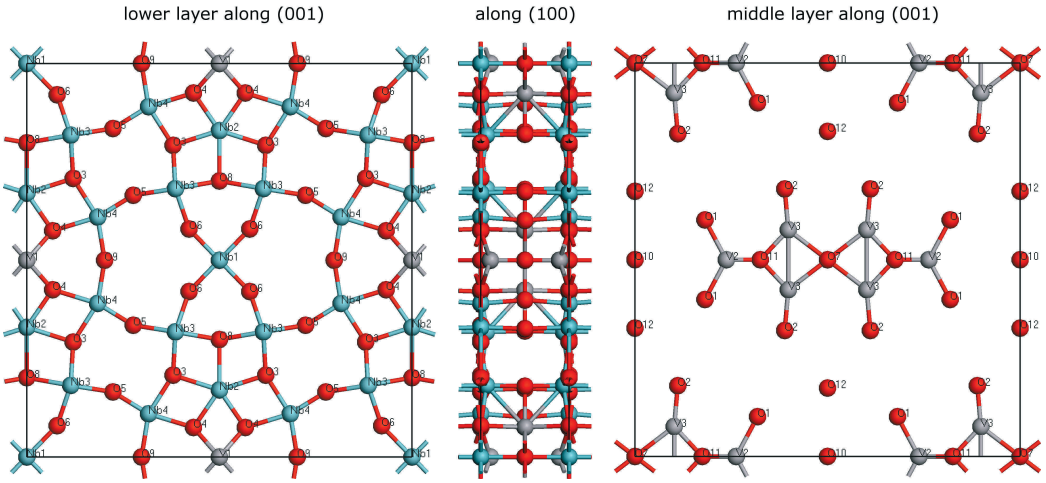

Figure 4.9: Overview of the $Nb_{10.7}V_{2.38}O_{32.7}$ structure. To the left and to the right, the atomic arrangement of the atoms along (001) is shown for the layers at z=0 and z=0.5, respectively. In the middle, a projection along (100) is shown.

display quite low occupancies, including the V^V sites. The DFT code used in the present study cannot be applied on structures with partially occupied positions and super-cell calculations for the large unit cell would have been beyond the available resources. Therefore, a simplified $1\times1\times2$ super-cell was constructed, basing on the reported structure by Börrnert *et al.*[156] (Figure 4.9). The half occupied positions of Nb3 and V1 overlap with one of their symmetry equivalents. In both cases, one part of each overlapping pair was arbitrarily removed. V2 (occupancy 0.35) is located on a position with eight symmetry equivalents in the super-cell. Accordingly, five of these equivalents were removed. Similarly, the 16-fold position of V3 displays occupancy of 0.17 so that 14 of these symmetry related equivalent atoms were arbitrarily removed. Finally all of the O11 equivalents which were not in contact with either a V2 or a V3 atom were also removed from the simplified model (in total 3 out of 8). Finally, three niobium vacancies were required to retain the O:(Nb+V) ratio of 5:2 so that one of the Nb1, Nb2 and Nb4 atoms was omitted per type, respectively. The k-point set used for the electronic minimisation was $1\times1\times6$.

Unfortunately, calculation results based on this model indicated a partially unoccupied valence band, i.e. metallic behavior. And a series of related calculations, as well starting from models with reduced structural complexity, exhibited the same trend. As the empirical materials properties of $Nb_{10.7}V_{2.38}O_{32.7}$ do not indicate metallic behaviour, calculations with a finer k-point set and/or a larger super-cell are probably required to adequately describe this complex system. More detailed structural investigations concerning the position of the vanadium ions and the niobium vacancies might also be helpful.

In close analogy to $NbVO_5$, the valence band of $TaVO_5$ was found to be constituted almost exclusively of oxygen *p* orbitals, while the conduction band consists mainly of the *d* states of tantalum and vanadium with oxygen *p* states as a minor constituent (Figure 4.11). Table 4.6 compares the effective masses of the charge carriers in conduction and valence band, indicating a relatively low mobility of the holes in the valence band in contrast to the high mobility of electrons in the conduction band. Band structure calculations show an indirect band gap (T to Γ) of 2.11 eV for $TaVO_5$ (Figure 4.10).

Tetrahedrally coordinated vanadium centres are a common structural motif of

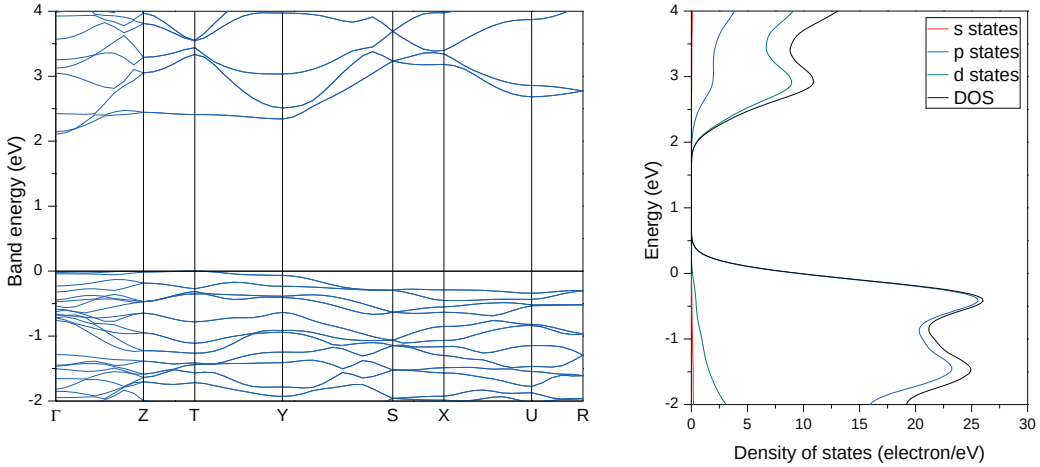

Figure 4.10: Band structure of $TaVO_5$ close to the band gap (left) and corresponding density of states (right).

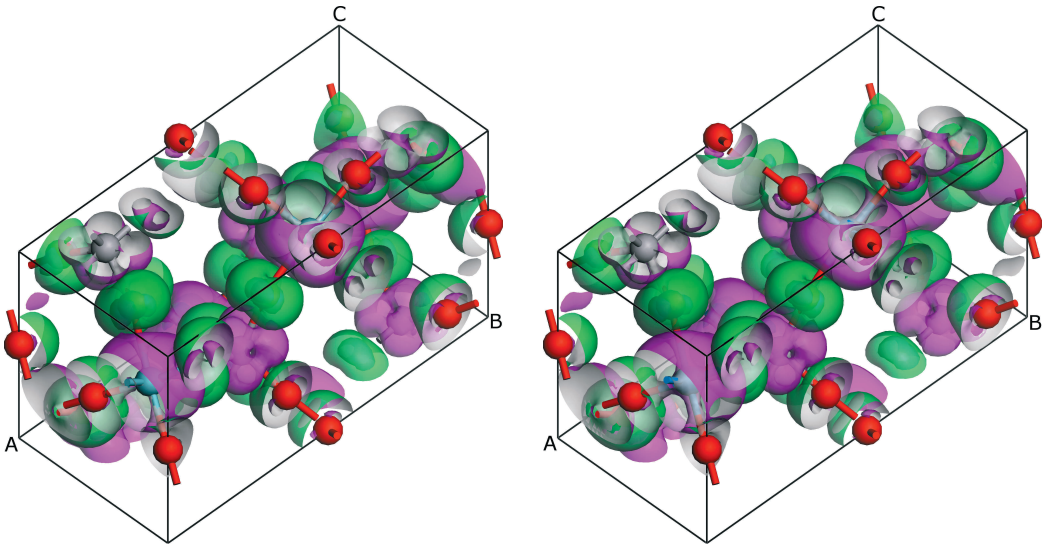

Figure 4.11: Crystal structures of $NbVO_5$ (left) and $TaVO_5$ (right) with isosurfaces of the highest states of the valence band (green) and lowest states of the conduction band (pink) displayed (isovalue: 0.01); red: O, light blue: Nb, blue: Ta, grey: V.

Table 4.6: Effective masses of charge carriers in the conduction band (CB) and the valence band (VB) of $NbVO_5$ and $TaVO_5$. The values are indicated as effective masses (e_m^*/e_m). Both bands are degenerated, leading to two values for each direction.

$NbVO_5$					
VB (h^+)			VB (e^-)		
(100)	6.71	6.71	(100)	0.64	1.23
(010)	1.31	1.31	(010)	0.95	0.43
(001)	2.03	2.03	(001)	0.54	1.13
$TaVO_5$					
VB (h^+)			VB (e^-)		
(100)	8.72	8.72	(100)	0.58	0.93
(010)	1.41	1.41	(010)	0.80	0.39
(001)	2.68	2.68	(001)	0.45	0.84

$BiVO_4$, $NbVO_5$ and $TaVO_5$. In $BiVO_4$, the distorted tetrahedral VO_4 moiety of $BiVO_4$ enables closer contact of O$\cdots$O pairs, thereby enhancing the delocalisation of the valence band. The lone electron pairs of the remaining oxygen atoms are oriented towards the Bi centres. In contrast, the $\{VO_4\}$ tetrahedra in $NbVO_5$ and $TaVO_5$ are not significantly distorted, so that the oxygen orbitals are far less delocalised. Other than in $BiVO_4$, the *d* state contributions of Nb and Ta improve the delocalisation of the conduction band. The slightly more linear connection of $\{VO_4\}$ and $\{TaO_6\}$ polyhedra in $TaVO_5$ in contrast to $NbVO_5$ might account for the mobility differences of CB and VB: the higher V-O-Ta bond angle compared to V-O-Nb leads to a lower extent of interaction between the corresponding oxygen atoms of the polyhedra.

4.1.4 α- and β-$VOPO_4$

Selection of starting data sets for calculations on $VOPO_4$ was less straightforward, because the reported α_1 and the α_2 types differ slightly with respect to their lattice constants (Table 4.1).[178] As the PXRD pattern of the as-synthesised sample did not fit well with either modification (cf. Figure 4.20 below), a geometry optimisation of both modifications via internal energy minimisation was selected as the preferred strategy over structure refinement from PXRD data.

Interestingly, geometry optimisation of both modifications converged to a single structure, which is referred to as α-$VOPO_4$ in the following. The main differ-

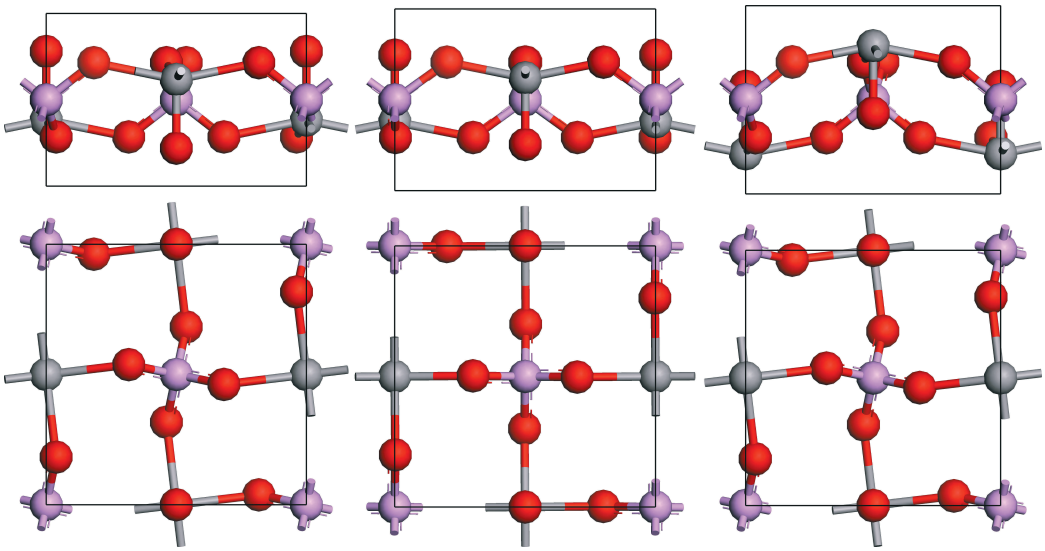

Figure 4.12: Crystal structures of α_1-$VOPO_4$ (left), α-$VOPO_4$ after geometry optimization (middle), and α_2-$VOPO_4$ (right). Structures are projected along (100) (upper row) and (001) (bottom row), respectively.

ence between the α_1- and α_2-type lies in the position and coordination of the vanadium atoms (cf. detailed comparisons in Figure 4.12 and 4.14). The vanadium centres of the α_1-type display square pyramidal coordination polyhedra which are coplanar with the adjacent phosphate tetrahedra. A slight shift of the vanadium positions in α_2-$VOPO_4$ leads to a distorted octahedral coordination through an additional, elogated V$\cdots$O contact to an oxygen atom of the neighboring plane. Geometry optimisation shifts the vanadium coordination sphere back to a square pyramid as present in the α_1 structure. However, the polyhedra in the α-form are connected in a linear fashion along the a- and b-directions, whereas the α_1-/α_2-types display a slight rotation of the VO_5 polyhedra around the *c* axis.

The valence bands of both α_1- and α-$VOPO_4$ consist mainly of the *p* states of the bridging oxygen atoms, whereas oxygen atoms which are exclusively bound to vanadium do not contribute significantly. This agrees with DOS calculations (Figure 4.13, Table 4.2) which indicate a negligible contribution of *d* states to the top of the valence band. The bottom of the conduction bands of both modifications can be described as mixtures of vanadium *d* states as main component together with oxygen *p* states. Note that the linear polyhedra chains of the α- structure lead to a slightly more delocalised conduction band, and this effect is also evident

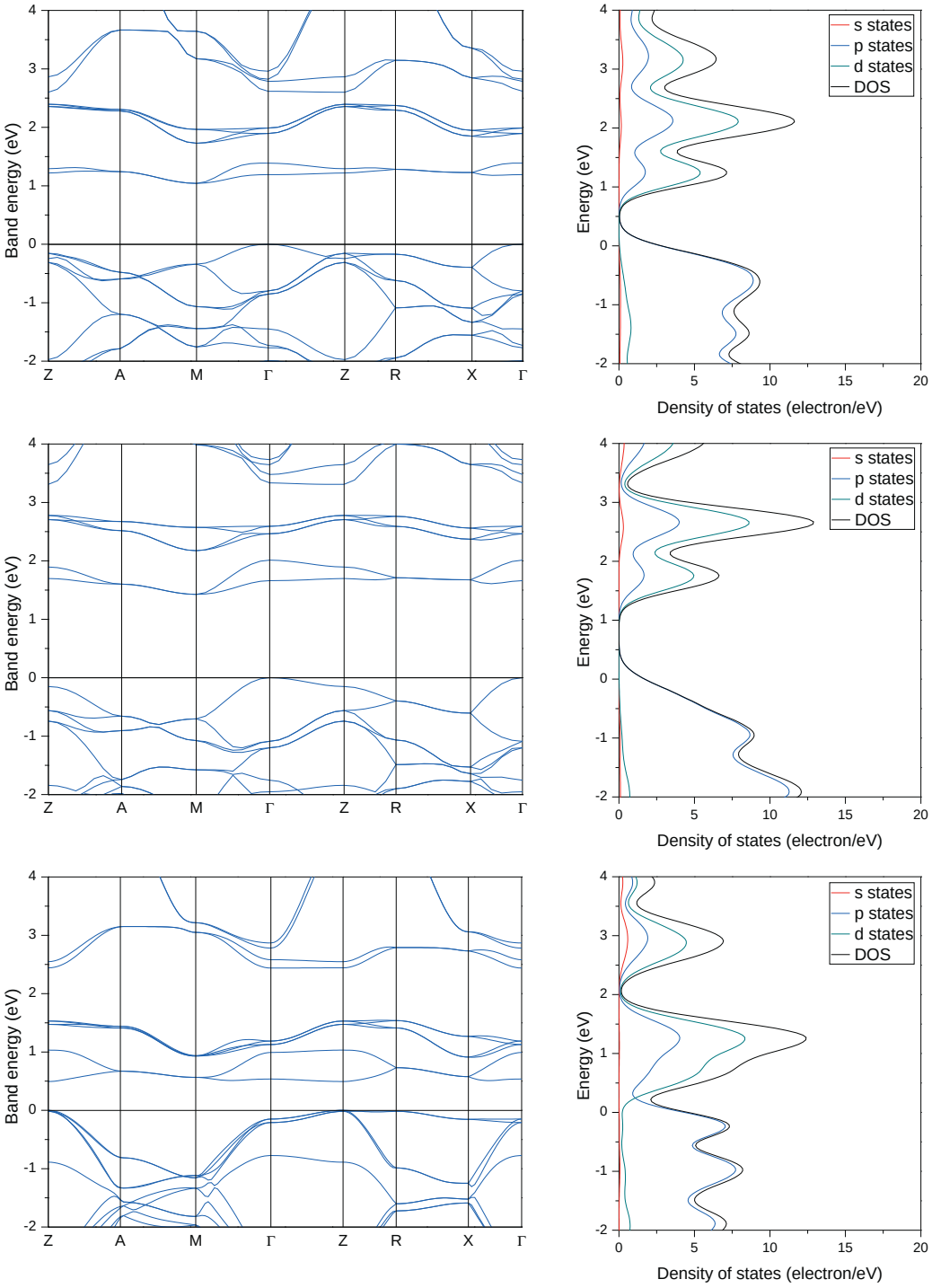

Figure 4.13: Band structures close to the band gap and corresponding densities of states of: α_1-$VOPO_4$ (top row), α-$VOPO_4$ (middle row), and α_2-$VOPO_4$ (bottom row).

Table 4.7: Effective masses of charge carriers in the conduction band (CB) and the valence band (VB) of the α-$VOPO_4$ modifications. The values are indicated as effective masses (e_m^*/e_m). Multiple values are due to band degeneration.

α_1-$VOPO_4$						
VB (h^+)				VB (e^-)		
	(100)	4.20		(100)	2.22	1.49
	(010)	4.20		(010)	2.22	1.49
	(001)	3.36		(001)	4.51	4.51
α-$VOPO_4$						
VB (h^+)				VB (e^-)		
	(100)	1.52		(100)	1.63	1.58
	(010)	1.52		(010)	1.63	1.58
	(001)	5.85		(001)	4.69	4.69
α_2-$VOPO_4$						
VB (h^+)				VB (e^-)		
(100)	0.53	0.51	6.20	(100)	2.64	
(010)	0.89	0.75	1.23	(010)	2.60	
(001)	6.27	10.4	10.4	(001)	21.4	

from the calculated charge carrier masses (Table 4.7). Band gap calculations for α_1- and α-$VOPO_4$ revealed the presence of indirect band gaps (Γ to M) of 1.04 eV and 1.43 eV, respectively (Figure 4.13).

α_2-$VOPO_4$ displays a notably different electronic structure (cf. Figures 4.13, and 4.14). The valence band is more delocalised, and it contains additional contributions of the non-bridging oxygen atoms together with a small fraction of vanadium *d* states. On the other hand, the conduction band is less delocalised than in the other two modifications, even though it stretches out to the non-bridging oxygen atoms and contains a smaller contribution of *d* states. This trend is furthermore reflected in the relative masses of the charge carriers (Table 4.7): While the in-plane mobility of holes in the valence band is clearly highest among the series of $VOPO_4$ modifications, the activated electrons of the conduction band are slightly heavier than in the other types. The band gap of α_2-$VOPO_4$ was found to be direct (Z to Z) with a width of 0.49 eV (Figure 4.13).

Other than the difficulties associated with the selection of α-$VOPO_4$ models, experimental input for β-$VOPO_4$ was available from straightforward synthesis of

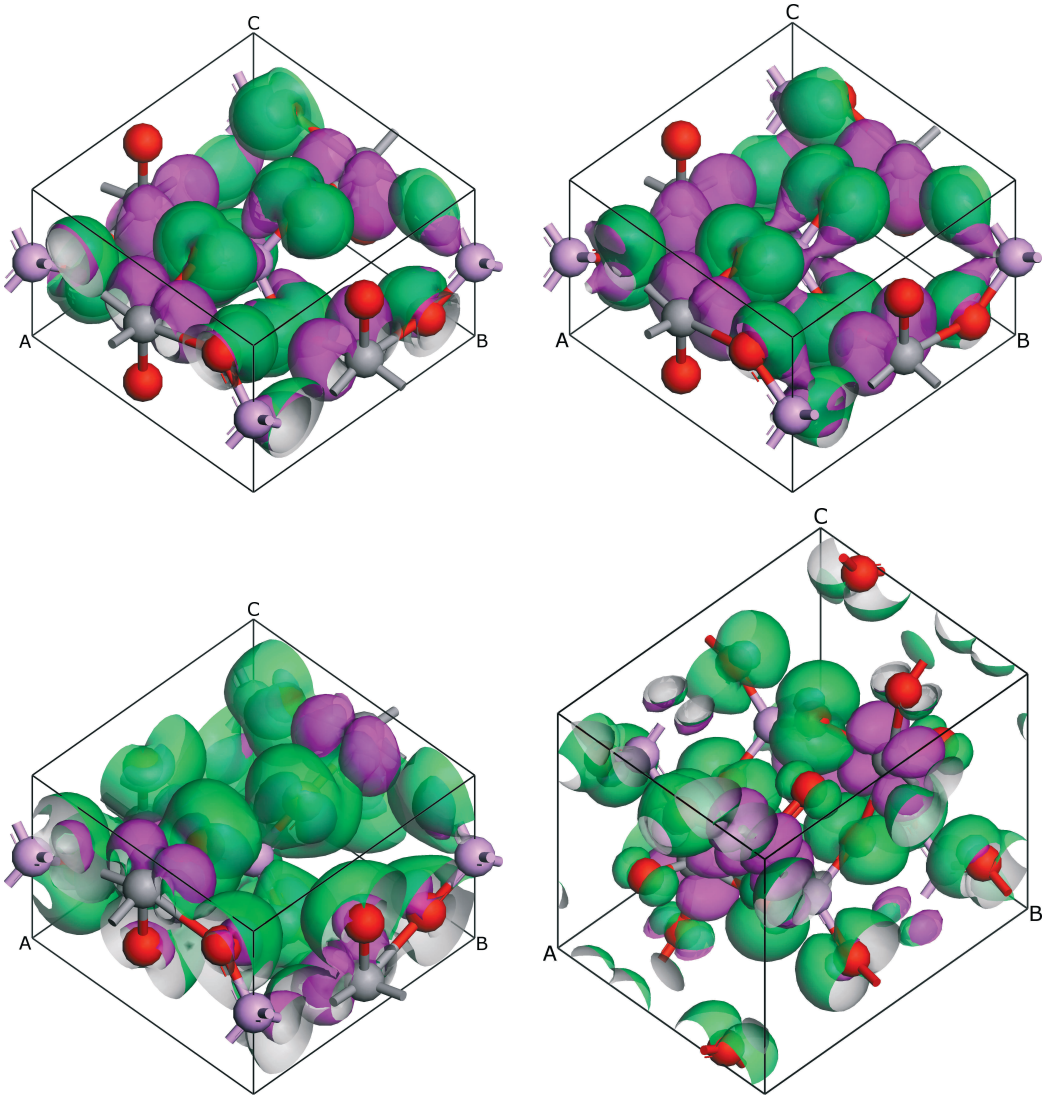

Figure 4.14: Crystal structures of α_1-$VOPO_4$ (top left), α-$VOPO_4$ after geometry optimisation (top right), α_2-$VOPO_4$ (bottom left), and β-$VOPO_4$ (bottom right) with isosurfaces of the highest states of the valence band (green) and lowest states of the conduction band (pink); isovalue: 0.01, red: O, violet: P, grey: V.

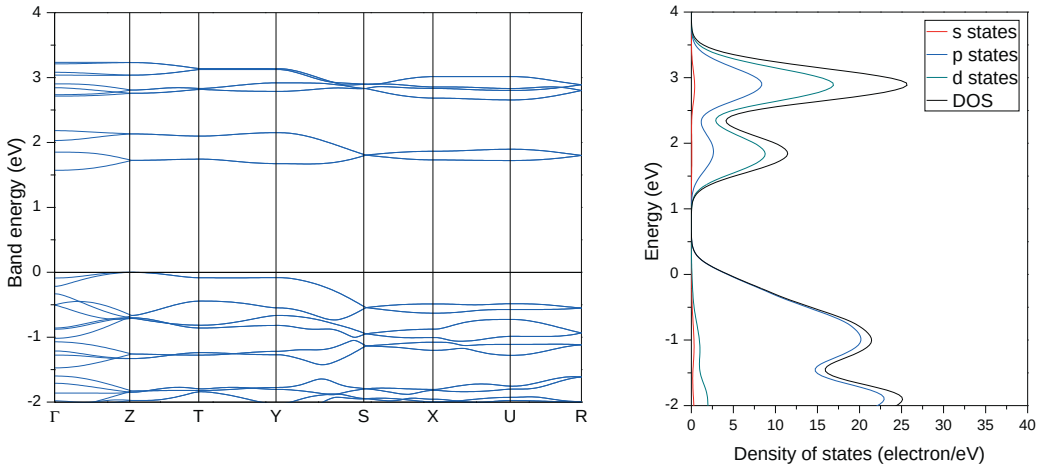

Figure 4.15: Band structure of β-$VOPO_4$ close to the band gap (left) and corresponding density of states (right).

Table 4.8: Effective masses of charge carriers in the conduction band (CB) and the valence band (VB) of β-$VOPO_4$. The values are indicated as effective masses (e_m^*/e_m). Multiple values are due to band degeneration.

VB (h^+)			VB (e^-)	
(100)	4.14	4.13	(100)	5.32
(010)	1.43	1.43	(010)	3.85
(001)	3.18	3.91	(001)	7.11

the phase pure compound. The top of the valence band consists almost exclusively of oxygen *p* orbitals with negligible contribution of *d* states. However, *d* states of vanadium mainly contribute to the bottom of the conduction band together with a small fraction of oxygen *p* states (Figures 4.15 and 4.14 or Table 4.2). Calculated effective masses of the charge carriers in conduction and valence band indicate a relatively low mobility of the holes in the valence band and even lower values for electrons in the conduction band (Table 4.8). Band structure calculations show an indirect band gap (Γ to Z) of 1.57 eV for β-$VOPO_4$ (Figure 4.15).

The different $VOPO_4$ modifications are an excellent model system to study the influence of slight changes in the local geometry of the vanadium centres on the overall electronic structure. The in-plane VB mobility increases with decreasing V$\cdots$O distance from α_1- to α-$VOPO_4$. This goes hand in hand with increasing interplanar distances, which is clearly reflected in the mobility along (001). The

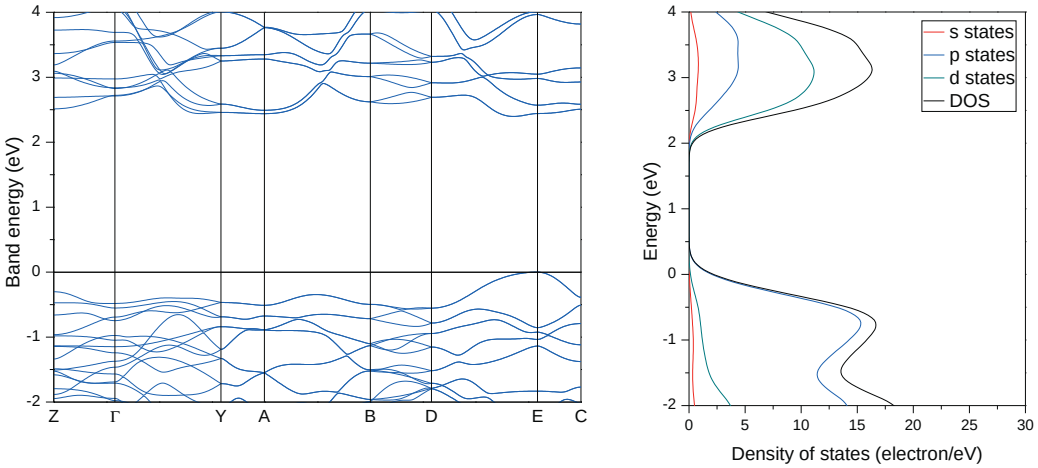

Figure 4.16: Band structure of ZnV_2O_6 close to the band gap (left) and corresponding density of states (right).

oxygen atoms of the distorted $\{VO_5\}$ pyramid in the α_2-structure are squeezed towards one side, resulting in a highly delocalised valence band. Although O$\cdots$O distances of β- and α-phase are comparable to a certain extent, the polyhedra arrangement in β-$VOPO_4$ results in directions of high VB delocalisation which are exclusively parallel to the y-axis. In α-$VOPO_4$, the linear connection between VO_5 and PO_4 polyhedra favors overlap of the vanadium *d* and the oxygen *p* orbitals. This argument is supported by the low CB mobilities for the β-phase, which exhibits a notably stronger relative shift of the polyhedra. High CB charge carrier massed of α_2-$VOPO_4$, however, arise from elongated V$\cdots$V distances.

4.1.5 ZnV_2O_6 and $Zn_2V_2O_7$

Next, the electronic structures of two zinc vanadates, namely ZnV_2O_6 and $Zn_2V_2O_7$, were compared with respect to promising properties for photocatalytic applications. Table 4.9 shows the effective masses of the charge carriers in conduction and valence band of ZnV_2O_6. The top of the valence band consists almost exclusively of oxygen *p* orbitals with only little *d* state contribution, while *d* states of vanadium are the main constituents of the bottom of the conduction band in combination with a minor contribution of oxygen *p* and zinc *s* states (Figures 4.16 and 4.18). Charge carrier masses indicate a relatively high

Table 4.9: Effective masses of charge carriers in the conduction band (CB) and the valence band (VB) of ZnV_2O_6 and $Zn_2V_2O_7$. The values are indicated as effective masses (e_m^*/e_m). Multiple values are due to band degeneration.

ZnV_2O_6					
VB (h^+)			VB (e^-)		
(100)	0.76	0.76	(100)	1.97	1.97
(010)	3.79	3.79	(010)	1.08	1.08
(001)	1.21	1.21	(001)	5.00	5.00
$Zn_2V_2O_7$					
VB (h^+)			VB (e^-)		
(100)	1.73		(100)	1.33	
(010)	18.7		(010)	9.55	
(001)	0.83		(001)	1.22	

mobility of the holes in the valence band compared to less mobile electrons in the conduction band. Band structure calculations for ZnV_2O_6 show a quasi-direct band gap (from (-0.5,0.5,0.5) to (-0.5,0.4,0.5)) of 2.40 eV (Figure 4.16).

Finally, calculations for $Zn_2V_2O_7$ display an upper valence band consisting almost exclusively of oxygen *p* orbitals with negligible *d* state contributions. In line with results for ZnV_2O_6, the bottom of the conduction band consists mainly of the *d* states of vanadium with a minor contribution of oxygen *p* states (Figures 4.17 and 4.18). The effective charge carrier mass values (Table 4.9) indicate a moderate to low mobility of both charge carrier types in valence as well as conduction band of $Zn_2V_2O_7$, which displays an indirect band gap (from Γ to D) with a value of 2.65 eV (Figure 4.17).

The higher coordination number of vanadium, and therefore lower O$\cdots$O distances, improves the delocalisation of the valence band of ZnV_2O_6 in comparison to $Zn_2V_2O_7$. The conduction band is less delocalised in $Zn_2V_2O_7$ due to a combination of longer V$\cdots$V distances and relative positional shifts of the VO_4 tetrahedra.

Key tuning parameters for the electronic structure of oxides with respect to photocatalytic properties can thus be summarised as follows: (1) Dense packing, (2) small cations with high coordination numbers, (3) linear connection of polyhedra to maximise *p* and *d* orbital overlap.

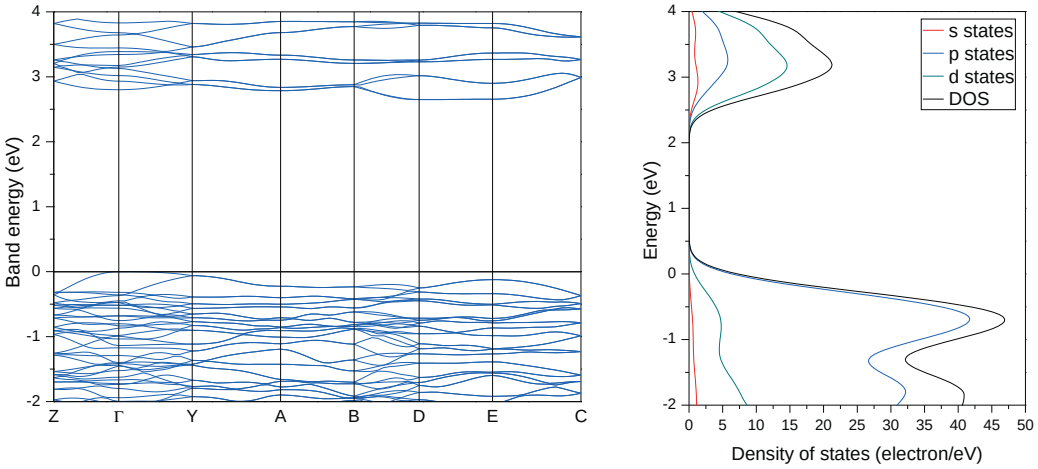

Figure 4.17: Band structure of $Zn_2V_2O_7$ close to the band gap (left) and corresponding density of states (right).

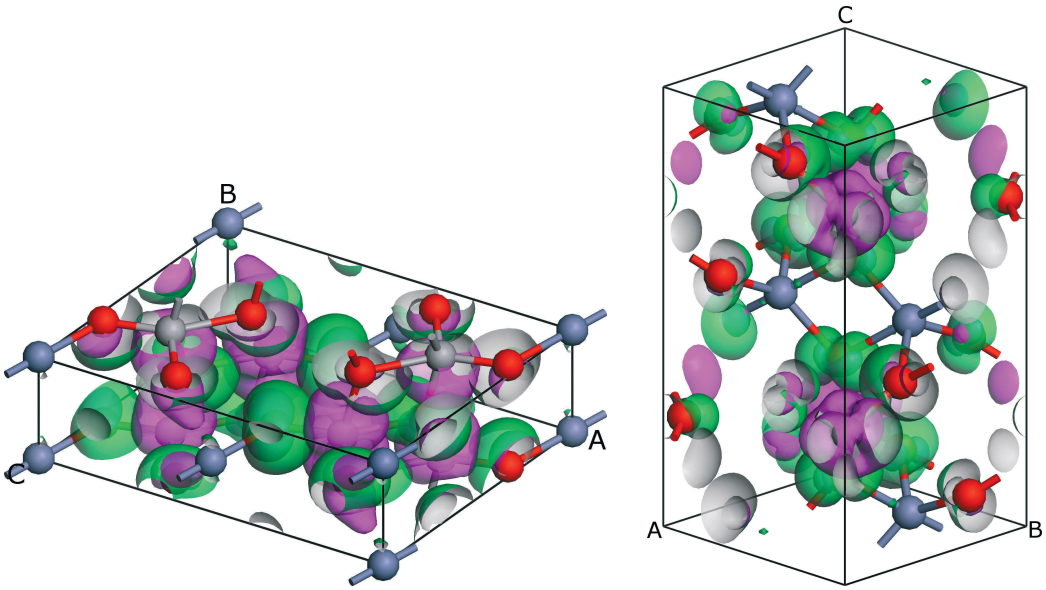

Figure 4.18: Crystal structure of ZnV_2O_6 (left) and $Zn_2V_2O_7$ (right) with isosurfaces of the highest states of the valence band (green) and lowest states of the conduction band (pink); isovalue: 0.01, red: O, steel blue: Zn, grey: V

4.2 Synthesis and materials properties

4.2.1 Synthesis and surface area

Ag_3PO_4 was obtained from a literature protocol:[53] $AgNO_3$ (1.019 g, 2.4 mmol) was thoroughly ground with $(NH_4)_2HPO_4$ (317 mg, 2.4 mmol). The product was washed three times with water and dried at 80 °C. The present study demonstrated that the Ag_3PO_4 yield could be increased using an excess of phosphate.

$BiVO_4$ was synthesised according to the protocol described in the previous chapter (section 3.1.1). For sake of comparison, a low surface area sample was prepared according to literature:[83] $Bi(NO_3)_3{\cdot}5H_2O$ (485 mg, 1 mmol) and NH_4VO_3 (117 mg, 1 mmol) were thoroughly mixed and ground, dried at 120 °C over night and calcined at 700 °C for 8 h.

The structurally related vanadates $TaVO_5$ and $NbVO_5$ were both synthesised via citrate gel routes. For $NbVO_5$, $NH_4Nb(C_2O_4)_2{\cdot}9H_2O$ (449 mg, 1 mmol) was dissolved in an aqueous solution of citric acid (600 mg, 3.1 mmol in 10 mL H_2O) while agitating in an ultrasonic bath. NH_4VO_3 (142 mg, 1.2 mmol) was added after dissolution of the Nb-containing precursor. The volume of the solution was subsequently reduced to about 1 mL at 105 °C and dried over night at 110 °C. The resulting green foam was powdered and calcined in air at 580 °C for 3 h. In order to remove an excess of V_2O_5, the product was soaked for 5–6 min with NH_3 solution (40 mL, 50 mM) twice, washed two times with water and dried at 80 °C in air; after each washing step the sample was collected by centrifugation.

As pointed out in preceding studies, phase pure $NbVO_5$ is generally quite difficult to obtain,[146] even from precursor mixtures containing a 20 % excess of vanadium. In addition to $NbVO_5$ and V_2O_5, which could be removed through washing, the powder pattern of the reaction product always showed traces of $Nb_{10.7}V_{2.38}O_{32.7}$ as a side product. Targeted synthesis of this phase could be realised, starting from a solution of $NH_4Nb(C_2O_4)_2{\cdot}9H_2O$ (449 mg, 1 mmol), NH_4VO_3 (26 mg, 0.2 mmol) and citric acid (500 mg, 2.6 mmol) in 10 mL H_2O. Apart from the reactant concentration and the omission of the final washing step, the procedure was identical to the synthesis of $NbVO_5$ described above. The products thus obtained exhibited a BET surface area around 10 m^2/g. In the following, however, the results obtained for $NbVO_5$ samples with accompanying side prod-

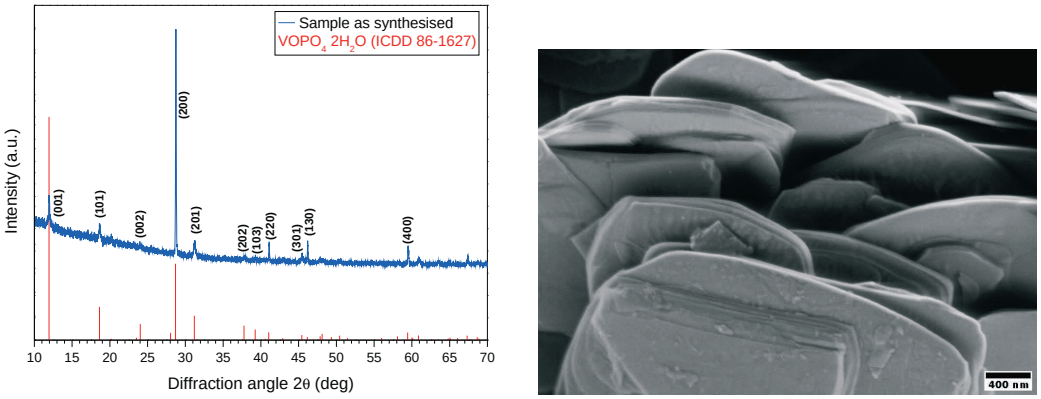

Figure 4.19: Powder diffractogram (left) of hydrothermally synthesised α-$VOPO_4 \cdot 2H_2O$ and representative SEM image (right). Texture effects for reflections of crystal planes containing *l* contributions arise from the anisotropic morphology.

ucts will be included in the discussion for the sake of completeness.

Another slight adjustment of the synthetic protocol gave access to $TaVO_5$, by replacing water as a solvent with ethanol in order to avoid precipitation side reactions. Accordingly, $TaCl_5$ (358 mg, 1 mmol) and NH_4VO_3 (117 mg, 1 mmol) were dissolved in 25 mL of an ethanolic citric acid solution, while otherwise following the procedure as described for $NbVO_5$. The gel-like products obtained from non-aqueous media after drying were powdered and calcined in air at 550 °C for 3 h, and the washing procedure was repeated as described above. Both compounds, $NbVO_5$ and $TaVO_5$, display rather low BET surface areas of 2 m^2/g and 5 m^2/g, respectively.

As mentioned above, the two basic modifications of $VOPO_4$ differ considerably with respect to their structural motifs: α-$VOPO_4$ consists of loose stacking of layers along the *c*-axis, while β-$VOPO_4$ displays a 3D network structure. Whereas various synthetic routes towards α-$VOPO_4 \cdot 2H_2O$ have been established as a first step to its follow-up use in intercalation compounds,[165,186,187] synthesis of the water-free compound was only reported for single crystals.[178] Therefore, α-$VOPO_4$ was first accessed via hydrothermally synthesised dihydrate samples. In a Teflon-lined stainless steel autoclave with a nominal capacity of 23 mL, V_2O_5 (182 mg, 2 mmol V^V) was suspended in an aqueous H_3PO_4 solution (5 mL,

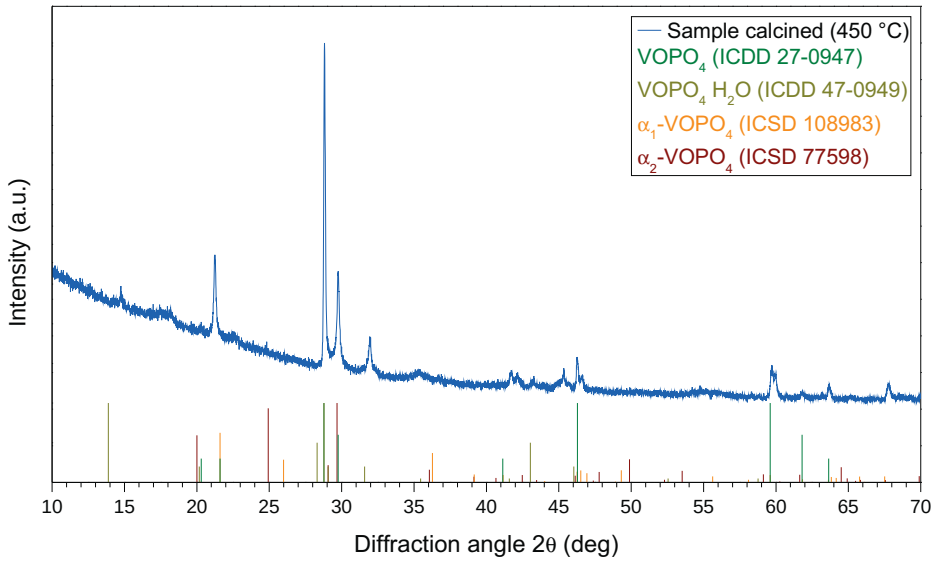

Figure 4.20: Powder diffraction pattern of hydrothermally synthesized $VOPO_4$ after drying at 450 °C showing no unambiguous fit with any of the reference patterns.

20 %) containing $Na_2S_2O_8$ (10 mg, 0.04 mmol).[5] The autoclave was maintained at 100 °C for 24 h and subsequently cooled to RT naturally. The yellow product was collected by filtration, washed with H_2O and dried at 80 °C (Figure 4.19).

However, drying of the dihydrate at different temperatures did not yield any of the reported structures (Figure 4.20).

On the other hand, synthesis of β-$VOPO_4$ by solid state methods as well as of ZnV_2O_6 and $Zn_2V_2O_7$ via citrate gel routes, respectively, was straightforward. For β-$VOPO_4$, $NH_4H_2PO_4$ (230 mg, 2 mmol) and NH_4VO_3 (234 mg, 2 mmol) were thoroughly mixed, pressed and calcined at 650 °C for 18 h. The preliminary product was then reground and calcined a second time under identical conditions.

ZnV_2O_6 and $Zn_2V_2O_7$ were obtained from two very similar synthetic protocols. The former was synthesised by adding $Zn(OAc)_2{\cdot}2H_2O$ (659 mg, 3 mmol) and NH_4VO_3 (702 mg, 6 mmol) to an aqueous solution of citric acid (2.13 g, 11 mmol in 60 mL H_2O). The mixture was treated in an ultrasonic bath until a clear solution was formed, and subsequently dried at 110 °C over night. The resulting foam was ground and calcined at 550 °C for 24 h. $Zn_2V_2O_7$ could be

[5]The sodium persulfate was added in order to avoid reduction of vanadium to V^{IV} (bluish-green product).

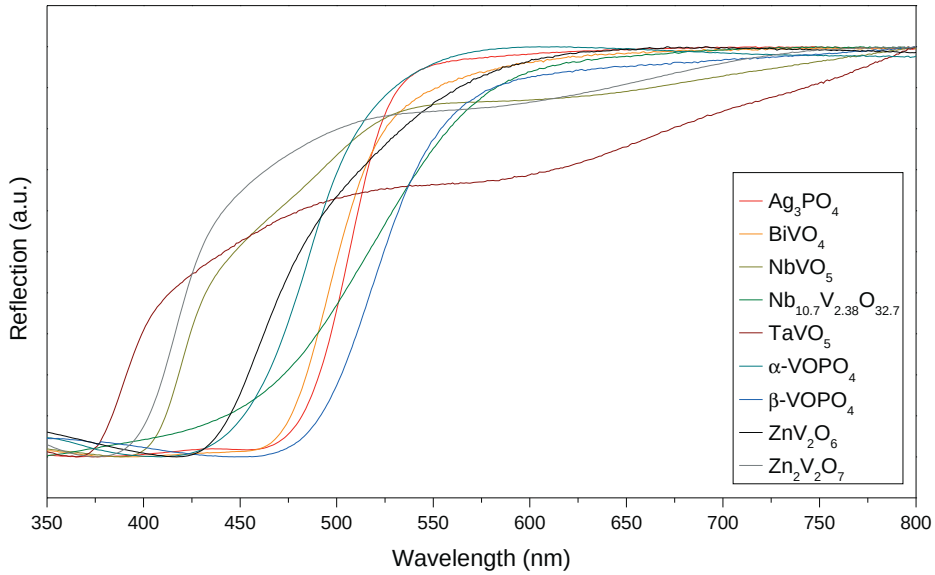

Figure 4.21: UV/vis reflectance spectra of the vanadate photocatalyst series.

obtained following the same procedure while reducing the amount of citric acid (1.5 g, 8 mmol in 60 mL H_2O) and using V_2O_5 (273 mg, 3 mmol V^V) as vanadium precursor.

For sake of comparison, ZnV_2O_6 was accessed also on a hydrothermal route.[166] $Zn(OAc)_2{\cdot}2H_2O$ (364 mg, 1.7 mmol) was added to a warm aqueous solution (75 °C, 18.5 mL) of NH_4VO_3 (281 mg, 2.4 mmol) in a 23 mL Teflon inlay of a stainless steel autoclave. The resulting orange suspension was stirred for five minutes and kept at 200°C for one week. The product was deposited as a yellow felt-like lining on the walls of the Teflon vessel, which was washed with water, centrifuged and dried at 80°C.

β-$VOPO_4$ and ZnV_2O_6 samples exhibited BET surface areas around 1 m^2/g, while the surface area of $Zn_2V_2O_7$ was below this value. The hydrothermally synthesised ZnV_2O_6 achieved a BET surface area of 4 m^2/g.

4.2.2 Theoretical vs. spectroscopic band gap determination

UV/vis reflectance plots for the vanadate series (Figure 4.21) were evaluated with the Tauc-plot method (cf. introduction, section 1.4.3). Differentiation between data plot strategies for direct and indirect band gaps was based on the results of

Table 4.10: Band gaps (in eV) calculated by DFT and derived from UV/vis reflection mode measurements.

Material	Calculated	Observed
Ag_3PO_4	0.27	2.29(2)
$BiVO_4$	2.24	2.32(4)
$NbVO_5$	1.99	2.86(7)
$Nb_{10.7}V_{2.38}O_{32.7}$	—	2.00(10)
$TaVO_5$	2.11	3.06(7)
α_1-$VOPO_4$	1.04	2.31(1)[1]
α-$VOPO_4$	1.43	2.31(1)[1]
α_2-$VOPO_4$	0.49	2.31(1)[1]
β-$VOPO_4$	1.57	2.18(2)
ZnV_2O_6	2.40	2.66(13)
$Zn_2V_2O_7$	2.65	2.85(11)

[1] structure assignment unclear (cf. text)

the above band structure calculations. Experimentally determined optical band gaps are compared with the calculated values in Table 4.10. It is noteworthy that for most of the compounds the calculated band gap is in very good agreement with the experimental values, especially for $BiVO_4$ and both zinc vanadates. Generally, the expected underestimation of the band gap by DFT methods is considerably higher, i.e. around 40 %.[181]

Most of the investigated materials display band gaps in the visible range, with the exception of $TaVO_5$, $Zn_2V_2O_7$, and possibly $NbVO_5$. Note that the band gaps of ZnV_2O_6 and $Nb_{10.7}V_{2.38}O_{32.7}$ are even below those of the reference photocatalysts $BiVO_4$ and Ag_3PO_4. Consequently, all compounds were investigated for their activity in photocatalytic dye degradation.

4.2.3 Photocatalytic tests

The results of the photocatalytic dye degradation tests are summarised in Figure 4.22. As the α-$VOPO_4$ sample dissolved quickly (within 10–15 min) under reaction conditions, the according results are not included. $BiVO_4$ is clearly the most active compound among the tested vanadate series. However, $NbVO_5$, β-$VOPO_4$, $Nb_{10.7}V_{2.38}O_{32.7}$ and ZnV_2O_6 also show activity in rhodamine B (RhB) degradation. The activity of the above-mentioned $NbVO_5$ sample is higher than

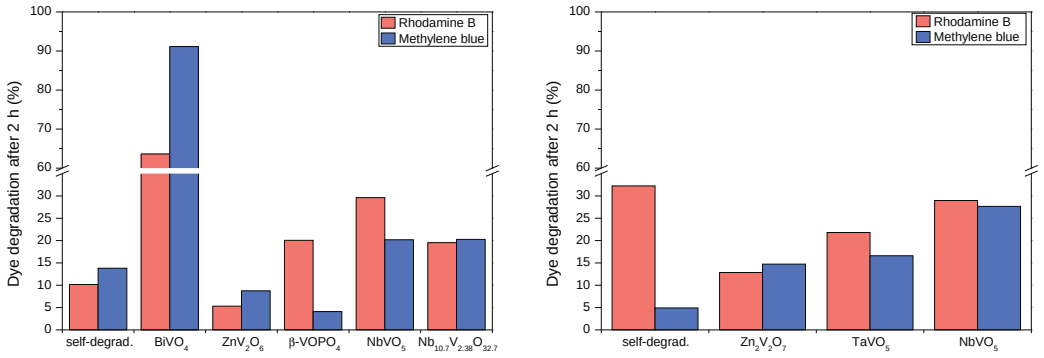

Figure 4.22: Comparison of the dye degradation performance of the vanadate series under irradiation with blue light (left) and black light (right).

the values for phase pure $Nb_{10.7}V_{2.38}O_{32.7}$. Consequently, either $NbVO_5$ itself is more active than $Nb_{10.7}V_{2.38}O_{32.7}$, or heterojunction effects between the different phases might account for the enhanced performance (compare chapter 2). Concerning methylene blue (MB) degradation, only the two niobium vanadates show activity, whereas for all other compounds shadowing effects lead to degradation rates below the self-degradation reference.

Compounds with a band gap > 2.8 eV ($NbVO_5$, $TaVO_5$ and $Zn_2V_2O_7$) exhibited photocatalytic activity in MB degradation under UV irradiation. Note that the self-degradation of RhB under UV light irradiation excludes this test dye from use under the given conditions (cf. section 1.4.4 and Figure 1.8).

Reference tests with Ag_3PO_4, which was recently discovered as a highly active visible-light photocatalyst,[53] led to complete dye bleaching after 5–10 minutes under blue light irradiation. Surprisingly, however, the colour of the Ag_3PO_4 catalysts quickly changed in the course of the reaction from yellow to black. Powder diffraction patterns recorded on samples after different irradiation times indicate that the colour change is due to rapid catalyst decomposition, resulting in the formation of metallic silver (Figure 4.23).

Next, we compared the expected photocatalytic activity on the basis of the above calculations to the experimentally observed performance (Table 4.11). Selection criteria for high expected activity can be summarised as follows: (a) values for relative charge carrier mass should be low in at least one direction and (b) high mobility in both VB and CB was considered favorable over high mobility only in

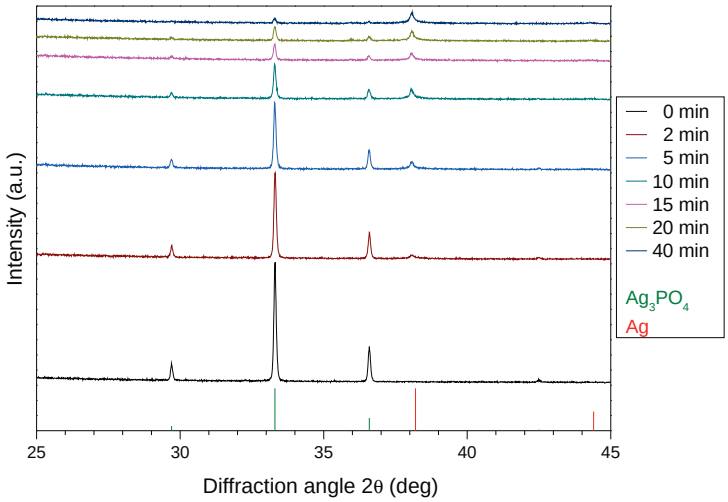

Figure 4.23: PXRD plots of Ag_3PO_4 photocatalyst sampled after different reaction times. All patterns were recorded subsequently and show absolute intensities for the sake of direct comparison. Reference patterns: ICDD 84-0510 (Ag_3PO_4), ICDD 87-0720 (Ag).

Table 4.11: Comparison of predicted and experimentally determined photocatalytic activity sequences for investigated vanadate series.

Measured	Expected
$BiVO_4$	ZnV_2O_6
$NbVO_5$	$BiVO_4$
$Nb_{10.7}V_{2.38}O_{32.7}$	$NbVO_5$
$TaVO_5$	$TaVO_5$
$Zn_2V_2O_7$	$Zn_2V_2O_7$
β-$VOPO_4$	β-$VOPO_4$
ZnV_2O_6	

one of the bands.

Interestingly, predicted and observed activities are almost identical - with one notable exception. ZnV_2O_6, which shows promising high mobility in both VB and CB, displays by far the lowest photocatalytic activity in dye degradation. Given that ZnV_2O_6 catalysts are stable under the reaction conditions (Figure 4.24), the reasons for this low performance are not quite evident. Furthermore, raising the BET surface of ZnV_2O_6 through application of a hydrothermal protocol[166] to 4 m^2/g did not improve the photocatalytic activity. The dark-adsorption of dye to the catalyst was much more pronounced with MB than with RhB for both ZnV_2O_6 and $BiVO_4$, which permits a direct performance comparison of both ma-

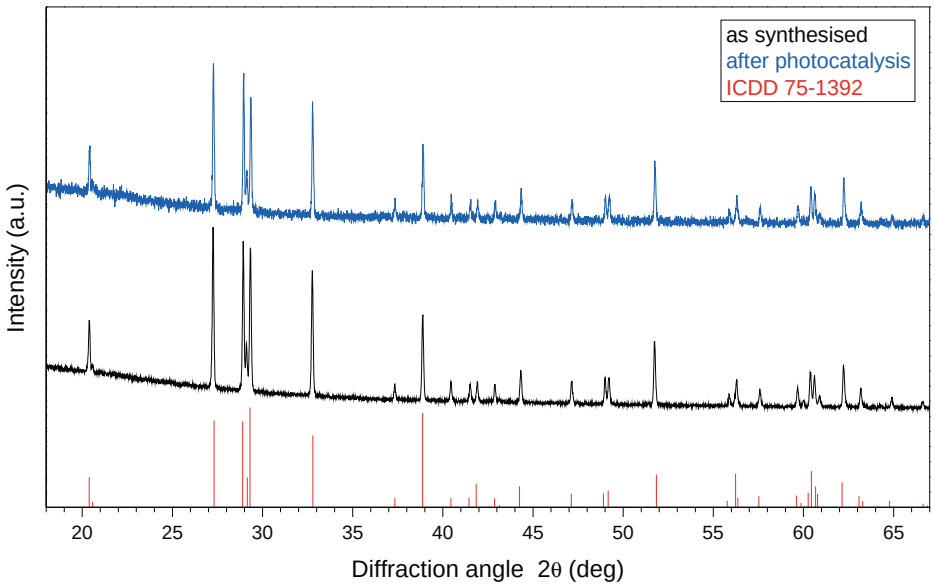

Figure 4.24: Representative powder diffraction patterns of ZnV_2O_6 photocatalyst before and after dye degradation tests.

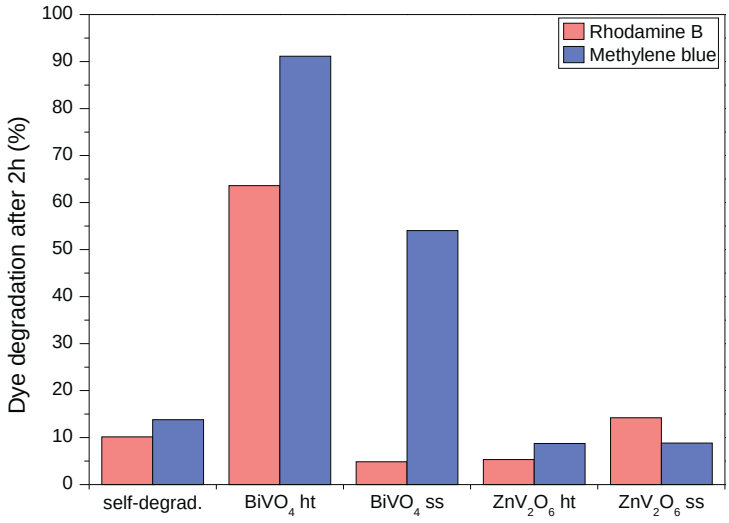

Figure 4.25: Comparison of the dye degradation performance of $BiVO_4$ and ZnV_2O_6 obtained from hydrothermal synthesis (ht) and solid state synthesis (ss).

terials. Interestingly, a $BiVO_4$ reference sample with deliberately low surface area (< 1 m^2/g) obtained from solid state routes[83] showed no activity in RhB degradation, while MB degradation was reduced but still overall significant (Figure 4.25).

All in all, the reasons for the low observed activity of ZnV_2O_6 remain unknown to date and difficult to explain with elementary criteria. In this context, it should be pointed out that the $BiVO_4$ photocatalyst used for the present materials performance comparison was carefully optimised in a previous study (cf. chapter 3). In contrast, synthesis of the remaining compounds was primarily focused on basic requirements, such as phase purity and crystallinity, so that they still leave plenty of room for optimisation of their photocatalytic properties.

Over the past years, several key performance criteria have been emphasised in photocatalyst design. Whereas the importance of band-bending for charge carrier separation has been pointed out,[42] this effect can, however, be reduced or even be cancelled out under illumination conditions.[43,44] In addition, the band bending is less pronounced for small particles with low doping-levels, where the particle size dimensions reach the scale of the charge accumulation layer.[43] Recent theories consider the availability of "shallow traps" more influential than the intrinsic mobilities in crystalline phases for the overall charge carrier mobility of nanomaterials.[57] Even if this issue were reduced through enhanced materials crystallinity, the issue of charge carrier stabilisation would still remain. As the timescales of charge carrier generation and mobility are far below those of the subsequent catalytic surface reactions, efficient charge separation and prolonged charge carrier lifetimes are of the essence to reduce adverse recombination processes.[64] Current strategies for such performance enhancement, which are well suited for follow-up investigations into the above vanadate series, include heterojunction formation with a second semiconductor (photocatalyst or cocatalyst) or the introduction of shallow acceptors to stabilise the charge carriers.[63,65,66,143]

4.3 Conclusions

A series of ternary vanadates as a model system for the quest for new photocatalysts was synthesised and investigated for catalytic activity, followed by correlation of structural and electronic properties.

Most importantly, the present study illustrates that basic DFT calculations with analysis of the charge carrier mobility are a straightforward and useful tool to predictively assign the relative activities of potential photocatalysts. We demonstrate the importance of accurate structural input data, preferably of experimental origin, for various representative compounds, given that the calculated electronic properties may vary strongly with apparently slight changes in the structure model. If accurate experimental structure information is not available, careful electronic structure optimisations may replace them, and application of up-to-date dispersion correction is of the essence.

The niobium-containing representatives of the series ($Nb_{10.7}V_{2.38}O_{32.7}$ and $NbVO_5$) showed promising performance in standard dye degradation tests. This is a good starting point for catalytic performance optimisation of both target compounds, e.g. through targeted adjustment of synthetic parameters or surface treatment. Furthermore, the influence of residual side products on the activity of $NbVO_4$ remains to be clarified, hand in hand with a more detailed investigation of the electronic structure of the accompanying phase $Nb_{10.7}V_{2.38}O_{32.7}$.

Moreover, photocatalytic activity does not solely depend on electronic properties, but remains a challenging multi-parameter problem encompassing synthetic pathways, defects in the crystal lattice, specific surface area, and the nature of the exposed surface on the crystallites as influential factors — just to point out a few key factors. As a consequence, comprehensive simulation of these complex materials parameters is currently too difficult and time-consuming to replace experimental screening in search of new photocatalysts. Straightforward DFT calculations are therefore an efficient tool to preselect promising materials for subsequent preparation, preferably through synthetic methods affording high crystallinity and surface area. As shown for Ag_3PO_4 and α-$VOPO_4$ in the present study, stability of the photocatalyst under reaction conditions is a key prerequisite which should be tested prior to further optimisation strategies.

Comparison of theoretically predicted and experimentally observed photocatalytic activity for the vanadates under investigation further corroborates the efficiency of DFT calculations for preliminary screening among the growing number of photocatalyst candidates. Concerning the low activity of ZnV_2O_6 as the sole exception among the investigated vanadate series, this issue cannot be directly

linked to surface area, adsorption or stability problems so that in-depth inquiries are under way. Investigating the influence of different heterojunction types on the photocatalytic activity of this material would be a promising strategy. Clear-cut identification of the limiting factor for ZnV_2O_6 in comparison to reference catalysts (such as $BiVO_4$) would pave the way towards a more fundamental understanding of key operational principles for visible-light-driven photocatalysts.

Chapter 5

Nitrides and Oxynitrides: An Outlook

The topic of the preceding chapters, namely oxide-based photocatalysts, is in the following extended towards synthetic routes to nitrides and oxynitrides. As discussed in section 1.3, the use of nitride cations can exert a positive effect on the position of the valence band and on the size of the band gap. Due to experimental challenges emerging during the final phase of the thesis, large parts of this chapter remain unpublished. Nonetheless, for the sake of completeness and possible follow-up projects, the approaches taken are described and the more promising ones are briefly discussed.

The high stability of the N_2 triple bond with respect to the O_2 double bond renders the synthesis of nitrides or even of oxynitrides very difficult, because the required reaction conditions are frequently demanding and more harsh than convenient "chimie douce" strategies.[188,189] For example, many syntheses require high temperature treatment in nitrogen or ammonia atmosphere — conditions under which many transition metal ions are easily reduced.

5.1 Nitridation in nitrogen atmosphere

The strategy is based on the prominent ZnO-GaN solid-solution photocatalyst type[54] with the goal to bring forward a different type of Zn^{2+} containing stoichiometric (oxy)nitride. In parallel, alternative nitridation methods were investigated, in analogy to recent reports.[190,191]

5.1.1 First target: $ZnTiN_2$

Encouraged by the results of Antonietti *et al.*,[190,191] the synthesis of $ZnTiN_2$ *via* the urea-gel method was attempted. In the first step, the desired transition metal chlorides are dissolved in an ethanol-based urea solution to form the corresponding urea complexes. The solution is subsequently dried at 80 °C, the resulting gel is transferred to an alumina crucible,[6] and finally calcined under nitrogen at-

[6] It is advisable to do this while the mixture is still hot and viscous, as it solidifies upon cooling.

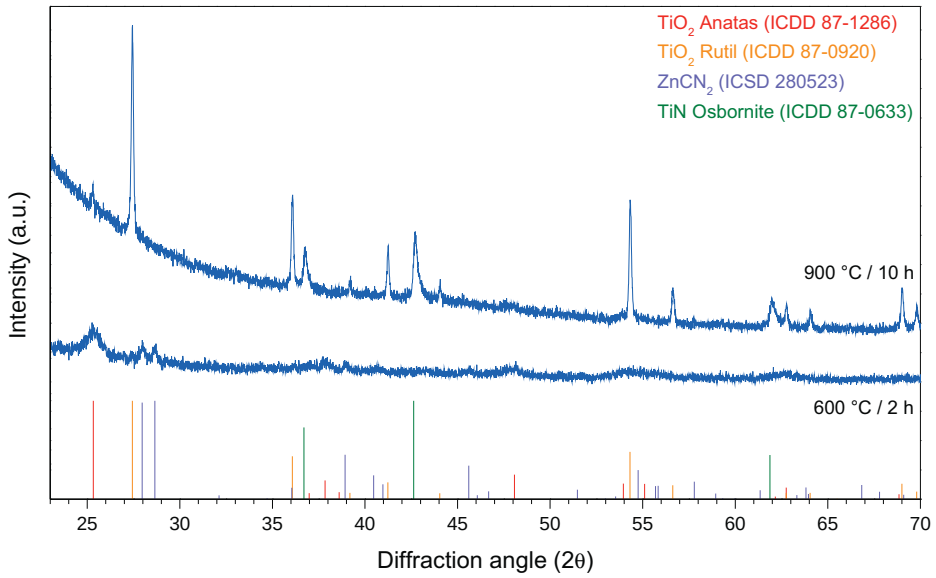

Figure 5.1: Powder diffraction patterns of the Zn-Ti-ureate samples calcined under N_2 atmosphere.

mosphere. The calcination temperatures using this technique were reported to be much lower than for other nitridation reactions.[190,191]

First experiments based on this technique started from $ZnCl_2$ and TiF_4 (later replaced by $TiCl_4$) in a 1:1 molar ratio. Unfortunately, the powder pattern of the calcined (900 °C, 10 h) sample shows only Ti-containing species (Figure 5.1), while EDX measurements of the same sample indicate only traces of Zn. The absence of zinc ions in the product can be explained by evaporation, as the boiling point of metallic zinc is around 907 °C.[192] A similar experiment at 600 °C for 2 h did not afford the desired compound either. Instead, the sample apparently consist of a low-crystalline mixture of anatase and zinc cyanamide ($ZnCN_2$). This interpretation is supported by the reaction of the pure metal powders with urea under the same conditions, where the powder diffraction peaks are better visible (Figure 5.2).

5.1.2 Second target: Nb/N substituted Zn_2TiO_4

The inverse spinel Zn_2TiO_4 contains Zn^{II} on the tetrahedral sites as well as Zn^{II} and Ti^{IV} on the octahedral sites, where the following ionic radii apply:[193] 0.88 Å (Zn^{II}), 0.75 Å (Ti^{IV}), and 0.77 Å (Nb^{V} or Ta^{V}). Accordingly, Nb^{V} or Ta^{V} should

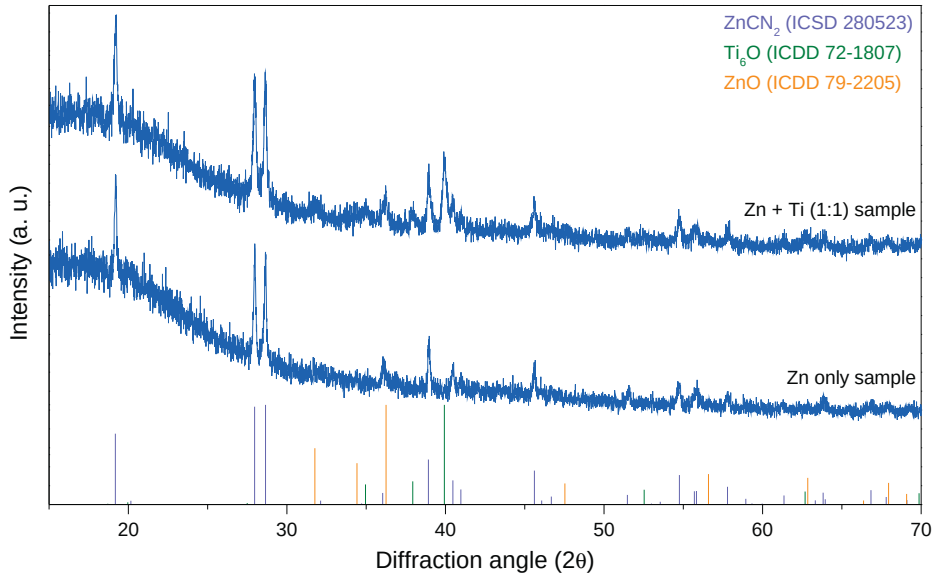

Figure 5.2: Powder diffraction patterns of the samples prepared from pure metal powders and urea.

be ideal co-dopants to stabilise N^{3-} ions in a Zn_2TiO_4 matrix by replacing Ti/O pairs by Nb/N or Ta/N combinations.

In analogy to section 5.1.1, a urea-gel was prepared from a stoichiometric mixture of the chlorides. The resulting gel was calcined under nitrogen at 500 °C, affording an X-ray amorphous product. When the experiment was repeated with a calcination temperature of 600 °C, the powder pattern showed a mixture of TiO_2 and $ZnTiO_3$. The EDX of the samples shows a very low Zn:Ti ratio and no significant nitrogen incorporation.

Next, two different oxide precursors were synthesised using a citrate gel method, namely for the pure zinc-titanate (Prc-1, Zn:Ti = 2:1) and one precursor with 10 % Ti replaced by Nb (Prc-2, Zn:Ti:Nb = 2:0.9:0.1). The precursors displayed strongly broadened peaks of Zn_2TiO_4 and sharper ones of ZnO. When Prc-1 is calcined in air at 1100 °C, the peaks of Zn_2TiO_4 become sharper and no ZnO can be detected in the product (Figure 5.3). The same applies for Prc-2 where a large fraction of Nb seems to be incorporated into a newly formed Zn-Nb-titanate phase, although a slight peak shift to lower diffraction angles indicates some Nb doping of the Zn_2TiO_4 phase. Different attempts at introducing nitrogen into the structure were undertaken, as described in the following.

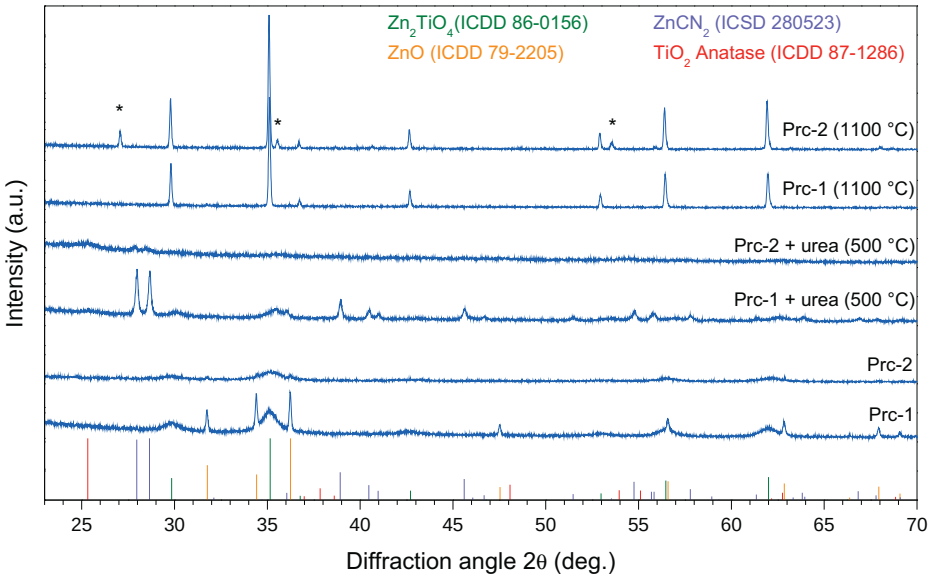

Figure 5.3: Powder diffraction patterns of Prc-1 and Prc-2 as prepared, after calcination under nitrogen with urea, and after calcination in air at higher temperature. Peaks of the newly formed phase $Zn_{0.15}Nb_{0.3}Ti_{0.55}O_2$ (ICDD 79-1186) are marked with stars.

Solvothermal treatment (24 and 42 h, 160 °C) in *n*-butylamine did not change the powder diffraction pattern of the precursors.

Calcining the precursors together with urea in nitrogen atmosphere (1 h, 500 °C) leads to the appearance of broad and low-intensity anatase TiO_2 and $ZnCN_2$ peaks in the powder diffraction patterns (Figure 5.3).

Experiments with melamine (or mixtures of urea and melamine) as nitridation agent led to the formation of carbon nitride. Although photocatalytic activity had been reported for this compound,[143,194] the phase mixtures obtained from the present survey experiments were inactive so that further experiments with melamine were discontinued.

Starting from mixtures of TiN and ZnO (with and without Nb precursors) did not yield mixed nitrides or oxynitrides. TiN decomposes into titania or mixed oxides upon calcination in air in presence of Zn and Nb, while TiN is stable under nitrogen atmosphere, albeit with loss of Zn. Calcination in humid nitrogen affords titania, but although ZnO is stable under these conditions, no coloured mixed phases could be obtained.

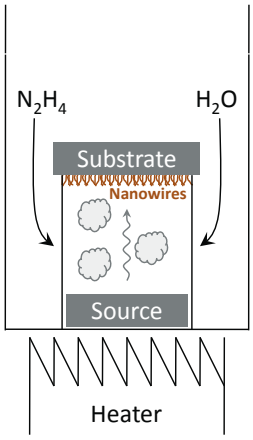

Figure 5.4: Schematic depiction of the reactor used for the hydrazine based chemical transport reactions.

5.2 Hydrazine-based gas phase synthesis of nitride nanowires

A rather innovative and promising method for the low-temperature synthesis of nanostructured nitrides was furthermore available through a SNF-SCOPES collaboration with the group of Prof. David Jishiashvili (Georgia). In addition to phosphide semiconductors as the main target of joint investigations,[195] the method also provides an elegant access to Ge_3N_4 nanowires.[196]

The beauty of this approach lies in its simplicity: While the synthesis of the nanowires is nothing else than chemical vapour deposition (CVD), in contrast to traditional approaches there is no need for expensive and often toxic volatile precursors. Instead, the volatile species are produced *in-situ* from the reactions of hydrazine and traces of water with the bulk precursors. Either pure metals or compounds can be used as precursor materials as has been demonstrated in our recent study on InP nanowire growth;[195] Figure 5.4 displays a scheme of the synthesis reactor. In the current set-up the substrate temperature is a function of the source temperature and of the distance between source and substrate, which can be varied with different spacers.

The presence of water in the system, which is often required for the formation of volatile suboxides, leads to a competition between oxides and nitrides. Experiments in the In/Ge system provide an illustrative example:[197] Under similar conditions as applied for the synthesis of Ge_3N_4, except for the presence of indium,

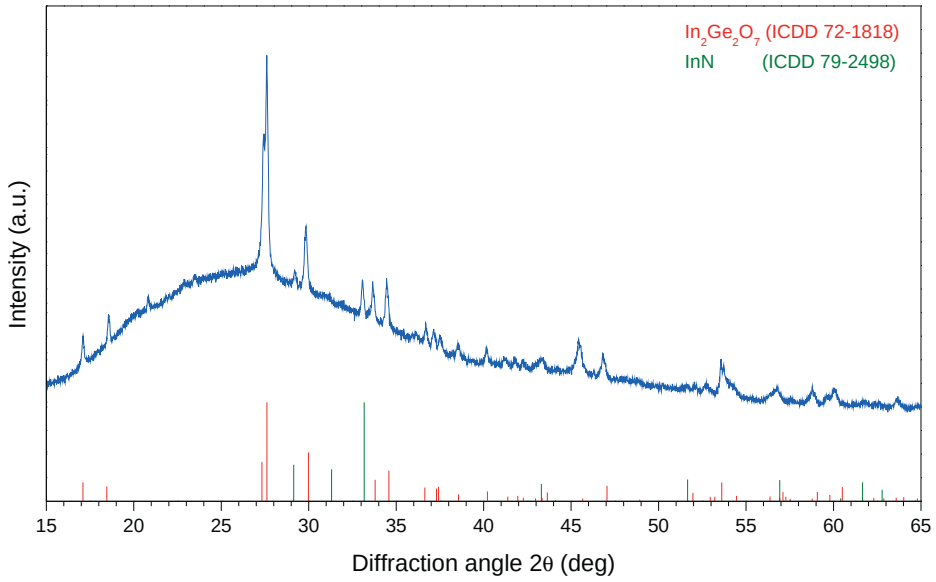

Figure 5.5: Powder diffraction pattern of a sample synthesised from In and Ge using similar conditions as for the Ge_3N_4 samples of reference 196. The strong amorphous background originates from the glass substrate, as the sample was measured in reflection mode still attached to the substrate.

$In_2Ge_2O_7$ is formed as main product in the presence of a a minor amount of InN (Figure 5.5). Accordingly, a high extent of control over different parameters, such as source and substrate temperature as well as the water content of the reaction atmosphere is required for the successful synthesis of nitride nanomaterials.

5.3 Reactive magnetron sputtering

In collaboration with Dr. Jörg Patscheider and Dr. Dominik Jaeger from EMPA Dübendorf first experiments aiming for oxynitride fabrication with reactive magnetron sputtering were undertaken. During sputtering, targets consisting of the selected metals are bombarded with ions which in turn eject atoms from the target surface. These ejected atoms are deposited on a substrate, where they are incorporated into a growing thin film. Usually, the ion source is a plasma discharge in an inert carrier gas. Reactive sputtering offers the option of adding other gases, such as oxygen or nitrogen.[198] The advantage of this technique is the high amount of control over the composition of the produced thin film, as the flux of the metals and the concentration of the reactive gases can be regulated independently. Disad-

Table 5.1: Elemental compositions of the two final samples (in at-%) as determined by XPS. The x parameter of $Ti_{1-x}Nb_xO_{2-x}N_x$ was calculated from the Ti:Nb ratio, and basing on this the deviation parameter Δ (see text).

Sample	Ti	Nb	O	N	x	Δ
jad2194	29.6	2.5	64.6	2.5	0.078	3.5
jad2195	29.5	2.8	61.4	5.3	0.087	10.5

vantages for photocatalytic applications are the frequently amorphous nature and smooth surface, i.e. low surface area, of the products.

Due to the above mentioned preparative difficulties through zinc loss, the target compound for reactive sputtering was $Ti_{1-x}Nb_xO_{2-x}N_x$ (x = 0.1). After optimisation of the deposition conditions over several test runs, two samples with different oxygen content were synthesised. Table 5.1 indicates their elemental composition as determined by x-ray photoelectron spectroscopy (XPS). As the samples were X-ray amorphous, no further phase assignements could be made (Figure 5.6). To determine how close a given sample composition came to the system, after determining x from the Ti:Nb ratio a deviation parameter, Δ, was calculated basing on the ratios O:Ti and O:N. A given composition was interpreted as compound $Ti_{1-x}Nb_xO_yN_z$, which led to:

$$\Delta = \left| \frac{y}{1-x} - \frac{2-x}{1-x} \right| + \left| \frac{y}{z} - \frac{2-x}{x} \right|$$

Both samples were tested for photocatalytic dye degradation of methylene blue and rhodamine B. While they showed activity for degradation of RhB under blue light irradiation, the degradation of MB under blue light and of both dyes under UV light was poor (Figure 5.7). This rather weak performance can be explained by insufficiently optimised sample compositions in combination with a relatively low specific surface area as a result of the synthesis technique. Interestingly, although calcination improved the crystallinity of the previously amorhpous samples (Figure 5.6), the photocatalytic performance remained unchanged.

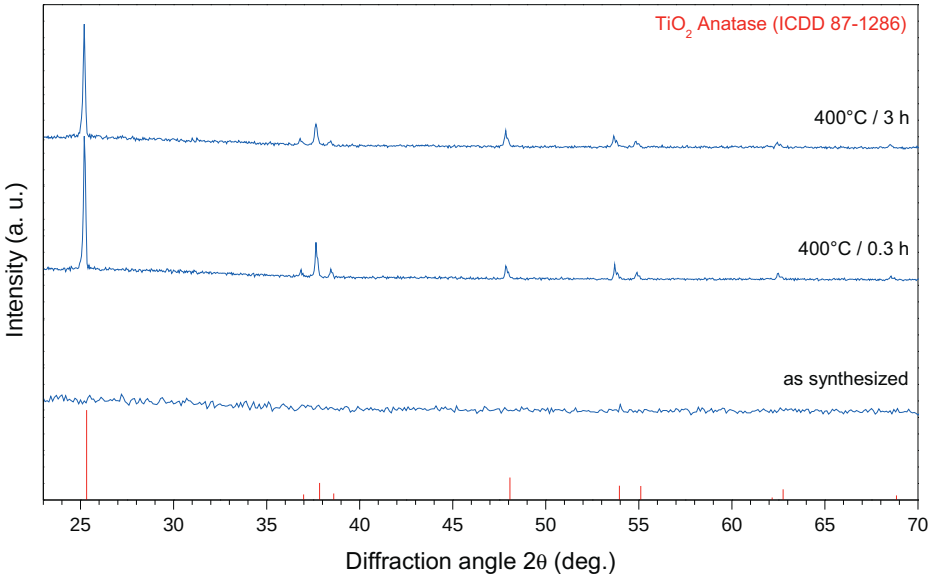

Figure 5.6: Powder diffraction pattern of the as-synthesised and calcined (N_2 atmosphere) sample jad2194.

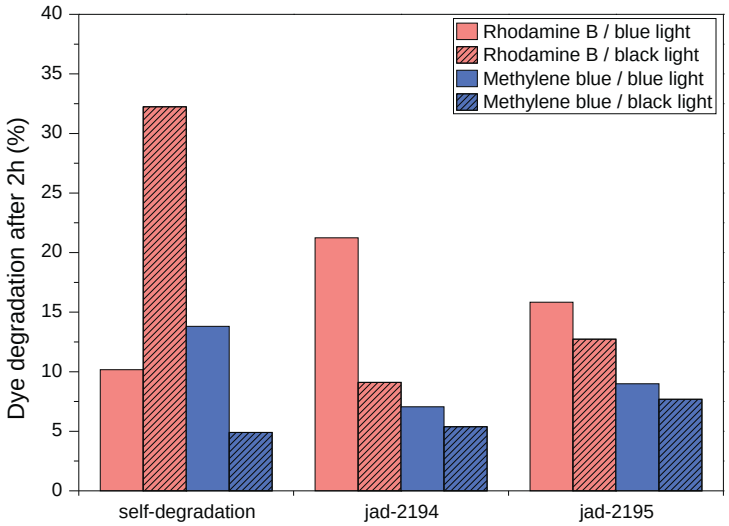

Figure 5.7: Results of photocatalytic dye degradation with the sputtered samples.

5.4 Conclusions and outlook

The high volatility of zinc under reductive conditions or in the absence of significant oxidant amounts in combination with its high oxygen affinity render the synthesis of a zinc containing ternary (oxy)nitride particularly challenging. Reactions in closed vessels (solvothermal or solid-state)[199] or with other nitridation agents (NH_3, N_2H_4, NaN_3)[200–202] might turn out more productive.

The combination of chemical transport and CVD, as described in section 5.2, could in principle be turned into a very powerful technique to access oxynitrides: One possibility would be the reduction of the water content to avoid the formation of pure oxides. Complete or partial replacement of water by CO, or by another chemical transport agent, would strongly enhance the application potential of the method.

Although the product composition might need some fine-tuning, the sputtering experiments point to a very promising direction. If the surface area of the system could be enhanced, for example by sputtering on a rough surface, the activity of the catalyst might be strongly improved. This would open up the opportunity to study the photocatalytic activity of $Ti_{1-x}Nb_xO_{2-x}N_x$ compounds as function of nitrogen content.

Even though their targeted synthesis may be challenging, nitrides and oxynitrides represent a very promising class of materials for photocatalytic applications, so that this concluding chapter is an incentive for follow-up investigations.

Summary

Providing clean water and energy for all inhabitants of our world is the major challenge of the near future. While the advances of technology have improved the living standards of many people, pollution increasingly threatens the water supplies. And while the global energy consumption of private people and companies is rising, the use of fossil fuels becomes problematic due to ecological, social and economical reasons.

Photocatalysis promises answers to both issues, by converting light energy into electrochemical energy which can be used for the degradation of pollutants or to generate energy carriers. At the same time, the manifold factors influencing the photocatalytic activity of materials are still difficult to control. One of the best known visible-light driven photocatalyst is $BiVO_4$. Therefore, two chapters of this thesis are focused on different approaches to improve this photocatalyst.

Firstly, the interplay of molybdenum doping, calcination and heterojunction formation is investigated. While clear trends for the individual parameters emerged, it became apparent that their respective influence on photocatalytic activity is not simply additive. For example, the activity for oxygen production can be enhanced by either calcining or coating with TiO_2 nanoparticles — but the combination of both treatments does not increase the activity with respect to the untreated sample. Furthermore it was confirmed once again that the different applications of waste water cleaning and energy carrier production require different catalyst optimisation strategies. While for the degradation experiments a high surface area is apparently more important than higher crystallinity, the reverse is true for oxygen production.

Secondly, the influence of different additives and pH conditions on the hydrothermal synthesis of undoped $BiVO_4$ is studied. Although hydrothermal reactions are basically "black box reactions", which are not straightforward to optimise and scale up, their frequent advantage of producing well-crystalline materials under comparatively mild conditions often outweighs this drawback. In this case, different hierarchically structured morphologies could be accessed and a new hydrothermal protocol is presented, optimising the morphology of pure $BiVO_4$ while

retaining its crystallinity. This combination of high surface area with high crystallinity leads to a very high photocatalytic activity, both in dye degradation experiments and in oxygen production.

Besides the improvement of existing photocatalysts, the discovery of new materials is often very much determined by serendipity. The list of requirements which a visible-light active photocatalysts needs to fulfill is long and comprises catalyst stability, band gap size and position, efficient charge separation and charge carrier mobility, as well as high surface activity.

Therefore, the fifth chapter illustrates how synthetic screening of vanadate systems can be combined with DFT calculation approaches. Although an exact prediction of photocatalytic activity is still not possible, calculations permit the comparison of expected activities. This combined screening approach resulted in the identification of several promising materials (i.e. $NbVO_5$ and $Nb_{10.7}V_{2.38}O_{32.7}$), which now need to be optimised for maximum activity.

Finally, the last chapter presents different approaches towards the highly promising nitride and oxynitride photocatalysts. Although nitrides and oxynitrides usually need synthesis conditions with well controlled atmosphere, the efforts are well invested: the influence of N^{3+} ions on the band gap is generally favourable for visible-light driven photocatalysts. Techniques ranging from simple “shake ’n bake” protocols with nitrogen precursors to reactive magnetron sputtering in high vacuum systems are compared and discussed.

All in all, this thesis successfully improved a leading photocatalyst material and illustrates the way towards a more targeted approach to new photocatalyst materials.

Zusammenfassung

Alle Menschen auf der Welt mit sauberem Wasser und mit Energie zu versorgen ist eine der grössten Herausforderungen der näheren Zukunft. Während der technologische Fortschritt den Lebensstandard vieler Menschen verbessern konnte, wird die Trinkwasserversorgung vieler zunehmend von Umweltverschmutzung bedroht. Und mit dem weltweit steigenden Energieverbrauch wird die Verwendung fossiler Energieträger aus ökologischen, sozialen und ökonomischen Gründen immer problematischer.

Photokatalyse verspricht eine Antwort auf beide Probleme, indem Lichtenergie in elektrochemische Energie umgewandelt wird, welche zum Abbau von Schadstoffen oder zur Erzeugung von chemischen Energieträgern genutzt werden kann. Allerdings ist die Kontrolle der verschiedenen Faktoren, welche die photokatalytische Aktivität eines Materials beeinflussen, noch immer anspruchsvoll. $BiVO_4$ ist einer der besten bisher bekannten Photokatalysatoren, die sich mit sichtbarem Licht anregen lassen. Entsprechend konzentrieren sich zwei Kapitel dieser Arbeit auf die verschiedenen Ansätze zur Verbesserung dieses Photokatalysators.

Zuerst wird das Zusammenspiel von Molybdän-Dotierung, Auslagerung und der Beschichtung mit anderen Halbleitern (heterojunction) untersucht. Während die einzelnen Parameter zu deutlichen Tendenzen führten, wurde klar, dass diese einzelnen Einflüsse nicht einfach addiert werden können. Beispielsweise kann die Aktivität zur Sauerstoffentwicklung sowohl durch Auslagern als auch durch Beschichtung mit TiO_2 Nanopartikeln verbessert werden — aber die Kombination der beiden Behandlungen führt nicht zu einer höheren Aktivität im Vergleich mit reinem $BiVO_4$. Des weiteren konnte wiederum bestätigt werden, dass die unterschiedlichen Anwendungen der Abwasserbehandlung und der Wasserspaltung auch verschiedene Optimierungsstrategien benötigen. Während für den Farbstoffabbau eine hohe spezifische Oberfläche offensichtlich wichtiger ist als die Kristallinität der Produkte, ist es bei der Sauerstoffentwicklung genau umgekehrt.

Weiterhin wurden die Einflüsse unterschiedlicher Additive und pH Bedingungen auf die hydrothermale Synthese von undotiertem $BiVO_4$ untersucht. Obwohl hydrothermale Synthesen im engen Sinne “black-box”-Reaktionen sind und

ihre Aufskalierung und Optimierung daher anspruchsvoll ist, wird dieser Nachteil von den häufig gut kristallinen Produkten und den milden Synthesebedingungen meist aufgewogen. In diesem Fall konnten verschiedene hierarchisch strukturierte Morphologien erzielt werden. Zudem wurde ein neues hydrothermales Syntheseprotokoll vorgestellt, welches die Morphologie des Produkts optimiert und gleichzeitig seine Kristallinität erhält. Diese Kombination von hoher spezifischer Oberfläche mit hoher Kristallinität führt zu einer hohen photokatalytischen Aktivität, sowohl in den Farbstoff-Abbauexperimenten als auch bei der Sauerstoffentwicklung.

Neben der Verbesserung existierender Photokatalysatoren wird die Endeckung neuer Materialien oft stark von glücklichen Zufällen bestimmt. Die lange Liste der Anforderungen an einen Photokatalysator, der von sichtbarem Licht aktiviert werden soll, umfasst unter anderem chemische Stabilität, Grösse und Position der Bandlücke, effiziente Trennung und Mobilität der Ladungsträger sowie hohe Aktivität der Oberfläche.

Aus diesem Grund illustriert das fünfte Kapitel wie die systematische Suche nach neuen Photokatalysatoren in Vanadatsystemen mit DFT Berechnungen kombiniert werden kann. Obwohl eine exakte Voraussage der photokatalytischen Aktivität nicht möglich ist, erlauben die Berechnungen den Vergleich der erwarteten Aktivitäten. Durch diesen kombinierten Ansatz liessen sich mehrere vielversprechende Materialien (z.B. $NbVO_5$ und $Nb_{10.7}V_{2.38}O_{32.7}$) identifizieren, die nun weiter optimiert werden müssen um ihre maximale Aktivität zu offenbaren.

Das letzte Kapitel zeigt verschiedene Ansätze zur Synthese der vielversprechenden Nitrid- und Oxynitrid-Photokatalysatoren. Obwohl die Synthesen beider Materialklassen normalerweise eine wohl kontrollierte Atmosphäre erfordert, ist der Aufwand gut investiert: Der Einfluss der N^{3+} Ionen auf die Bandlücke von Photokatalysatoren ist im Allgemeinen positiv. Verschiedene Techniken, von einfachen keramischen Synthesen bis hin zu reaktivem Kathodenzerstäuben in Hochvakuumsystemen, werden verglichen und diskutiert.

Alles in allem konnte im Verlauf dieser Doktorarbeit ein führendes Photokatalysator-Material verbessert werden und ein deutlich zielgerichteter Ansatz zur Entwicklung neuer Photokatalysatoren aufgezeigt werden.

Acknowledgments

This thesis would not have been possible without the practical help and moral support of many people.

First of all, I would like to thank Prof. Dr. Greta R. Patzke for giving me the opportunity to conduct my PhD studies in her group and for providing the freedom and infrastructure to explore many the aspects of photocatalyst development.

Furthermore, I also want to thank Prof. Dr. Roger Alberto and Prof. Dr. Roland K. O. Sigel for their work as co-referees of my thesis.

For some of the investigations the help of experts on their respective fields was necessary, and I gratefully acknowledge their contribution to the results presented above. Dr. Frank Krumeich from EMEZ was in charge of the TEM studies. The LA-ICP-MS analysis were performed by Kathrin Hametner in the laboratory of Prof. Dr. Detlef Günther. Dr. Thomas Fox, from our institute, performed the solid state NMR investigations.

The present and former members of our group greatly contributed to the good working atmosphere: Prof. Dr. Ying Zhou, Prof. Dr. Firasat Hussain, Dr. Pierre-Emanuel Car, Dr. Franziska Conrad, Dr. Georg Geisberger, Dr. Min Sheng, Dr. René Moré, Dr. Yang Zhen, Lu-Bin Ni, Kim von Allmen, Fabio Evangelisti, Roger Jacot, Hongfei Liu, Michael Olah, Robin Güttinger, Debora Ressnig, Peter Bösiger, and Franziska Borgogno. Special thanks go to Ying and Franziska, who helped me gain foot in our group and in solid-state chemistry in general. Also many thanks to Debora Ressnig, for being such a friendly, innovative, and independent master student. Thanks also for the manifold practical help of several students and interns: Franziska Borgogno, Angela Steinauer, Valerie Kröni, Adriana Hotz, and Felix Graber. Additionally I should thank Dr. Anne Landwehr, Dr. Mai Tran, Dr. Miguel Guttentag and many others for introducing me to, and making me feel welcome in the ACI.

I also would like to mention several scientist all over the world which I had the chance to meet during my thesis — many times they helped me, sometimes I could help them, all in all I would like to thank them for expanding my horizon:

Prof. Dr. Thomas Graule, Dr. Andre Heel, and Dr. Katarzyna Michalow-Mauke from EMPA Dübendorf — for shared equipment, practical help and many helpful discussions on the topic of photocatalytic dye degradation.

Prof. Dr. Roger Alberto, Dr. Benjamin Probst, and Dr. Miguel Guttentag from our department — for much help and discussions regarding the GC equipment and the O_2 production experiments.

Prof. Dr. David Jishiashvili of the Georgian Technical University — for a good collaboration, new insights into gas phase transport and pleasant discussions.

Dr. Ari P. Seitsonen (Department of chemistry, UZH), Henrik Grundmann (Institute of physics, UZH), and Joachim Breternitz (University of Glasgow) — for helpful discussions regarding the DFT calculations.

Dr. Jörg Patscheider and Dr. Dominik Jaeger from EMPA Dübendorf — for the possibility to test a promising synthesis concept and for help and discussions.

Paraskevi Efstathiou, and Federica Fina of the university of St. Andrews — for nice and interesting discussions. I still keep my fingers crossed for a successful combination of our systems: All the best!

Also I would like to mention Dr. Dorota Koziej (ETHZ), Alexandra Mägli (EMPA), as well as Dr. Sammy Verbruggen and Dr. Marianne Smits (University of Antwerp) — for many nice and interesting discussions at different conferences.

And, although our meetings did not have much to do with any of our theses, I would like to thank the members of the "Graduation ceremony organisation committee": Adele Ferrari, Bettina Schirrmeister, Klemens Koziol, Tobias Baldauf, Robbert Bloem, and not to forget, Cornelia Schmid and Isabelle Wüest.

Then I should thank some people without whom the institute would be in serious trouble: Dr. Ferdinand Wild, for his manifold help and for his patience regarding my questions about diverse devices under his responsibility. Hanspeter Stalder, for his great collection of spare parts and tools as well as for his custom-made apparatuses. Manfred Jöhri for computer and electrics support and for

posters printed under time pressure. Dr. Jae Kyoung Pak, Susanna Sprokkereef, Nathalie Melunsky-Fichter, and Ramona Erni for the great and flexible work with the financial and administrative tasks.

A special thank goes also to my parents and my friends. Their support during difficult times and the good time spent together during more relaxed times gave me the energy to pull it through. Especially I would like to mention Stephan, Dani, Andi, Rebekka, Kathrin, Ben, Manuel, and Roksolana.

And the life-long love and encouragement of my parents only brought me into the position of being able to do anything on my own, which of course also includes starting and finishing this thesis.

Finally, I gratefully acknowledge financial support by the University of Zurich, the Swiss National Science Foundation, and by the Graduate School of Chemical and Molecular Sciences Zurich.

Bibliography

[1] Geiss, I., Ballof, R., and Fricke-Finkelnburg, R., editors. "Epochen und Strukturen — Grundzüge der Universalgeschichte für die Oberstufe", volume II. Verlag Moritz Diesterweg, Frankfurt am Main, **1996**.

[2] Kingsnorth, P. "Global Attack! - Der neue Widerstand gegen die Diktatur der Konzerne". Bastei Lübbe, **2003**.

[3] Kingsnorth, P. "One no, many yeses". Simon & Schuster UK, **2004**.

[4] Frimmel, F. H. "Römpp Online: *Wasser*". *http://www.roempp.com/prod/*, last checked: 08/2012.

[5] Sousa, M. A., Gonçalves, C., Cunha, E. *et al.* "Cleanup strategies and advantages in the determination of several therapeutic classes of pharmaceuticals in wastewater samples by SPE-LC-MS/MS" *Anal. Bioanal. Chem.*, **399**(2):807–822, **2011**.

[6] Gupta, V. K., Ali, I., Saleh, T. A. *et al.* "Chemical treatment technologies for waste-water recycling — An overview" *RSC Adv.*, **2**(16):6380–6388, **2012**.

[7] Homem, V. and Santos, L. "Degradation and removal methods of antibiotics from aqueous matrices — A review" *J. Environ. Manage.*, **92**(10):2304–2347, **2011**.

[8] Watt, J. "Steam Engines, &c." Patent Nr. GB176900913, **1769**.

[9] International Energy Agency. "Statistics". *http://www.iea.org/stats/*, last checked: 08/2012.

[10] Vijaya Venkata Raman, S., Iniyan, S., and Goic, R. "A review of climate change, mitigation and adaptation" *Renewable Sustainable Energy Rev.*, **16**(1):878–897, **2012**.

[11] Intergovernmental Panel on Climate Change. "IPCC fourth assessment report: climate change 2007". *http://www.ipcc.ch/*, last checked: 08/2012.

[12] Stöcklin, Nando Nyberg, H. “Uranwirtschaft in Nordamerika — die Folgen für die Indigenen”. Incomindios Schweiz, **2001**.

[13] Vidal, J. “Nigeria’s agony dwarfs the gulf oil spill. The US and Europe ignore it” *The Observer*, **2010**.

[14] Lindenberger, D. and Kümmel, R. “Energy and the state of nations” *Energy*, **36**(10):6010–6018, **2011**.

[15] Kümmel, R., Lindenberger, D., and Eichhorn, W. “Wettbewerb, Wirtschaftsordnung und Umwelt”, volume III of *Schriften zur Politischen Ökonomik, Evolutorische und ökologische Aspekte*, chapter “Die Produktionsmächtigkeit der Energie und die Nutzungspreise von Energie und Arbeit”, pages 297–310. Peter Lang, Europäischer Verlag der Wissenschaften, **2004**.

[16] Maggio, G. and Cacciola, G. “When will oil, natural gas, and coal peak?” *Fuel*, **98**:111–123, **2012**.

[17] Taylor, P., Francoeur, M., Lavagne d’Ortigue, O. *et al.* “Worldwide trends in energy use and efficiency — key insights from IEA indicator analysis”. Technical report, International Energy Agency (IEA) & Organisation for Economic Co-operation and Development (OECD), **2008**.

[18] Lewis, N. S. and Nocera, D. G. “Powering the planet: chemical challenges in solar energy utilization” *Proc. Natl. Acad. Sci. U. S. A.*, **103**(43):15729–15735, **2004**.

[19] Desertec Foundation. “Clean power from deserts — the DESERTEC concept for energy, water and climate security (WhiteBook)”. Protext Verlag, Bonn, 4th edition, **2009**.

[20] Armaroli, N. and Balzani, V. “The future of energy supply: challenges and opportunities” *Angew. Chem., Int. Ed.*, **46**(1–2):52–66, **2007**.

[21] Krings, S., editor. “Statistisches Jahrbuch für die Bundesrepublik Deutschland mit ‘Internationalen Übersichten”’. Statistisches Bundesamt, Wiesbaden, **2011**.

[22] Schweizerisches Bundesamt für Statistik BFS. "Arealstatistik Standard (NOAS04) - Gemeindedaten nach 4 Hauptbereichen (Periode 2004/09)". *http://www.bfs.admin.ch/bfs/portal/de/index/themen/02/03/blank/data/gemeindedaten.html*, last checked: 08/2012.

[23] United States Census Bureau. "2010 Census of population and housing - CPH-2. Population and housing unit counts: 2. Population, housing units, and land area by urban and rural and size of urban area". *http://www.census.gov/prod/cen2010/index.html*, last checked: 09/2012.

[24] Klingshirn, C. "Römpp Online: *Photoelement*". *http://www.roempp.com/prod/*, last checked: 09/2012.

[25] Schlögl, R. "Catalytic synthesis of ammonia — a 'never-ending story'?" *Angew. Chem., Int. Ed.*, **42**(18):2004–2008, **2003**.

[26] RÖMPP-Autor. "Römpp Online: *Haber-Bosch-Verfahren*". *http://www.roempp.com/prod/*, last checked: 06/2013.

[27] Ashley, M., Magiera, C., Ramidi, P. *et al.* "Nanomaterials and processes for carbon capture and conversion into useful by-products for a sustainable energy future" *Greenhouse Gases: Sci. Technol.*, **2**(6):419–444, **2012**.

[28] Olah, G. A., Goeppert, A., and Prakash, G. K. S. "Chemical recycling of carbon dioxide to methanol and dimethyl ether: from greenhouse gas to renewable, environmentally carbon neutral fuels and synthetic hydrocarbons" *J. Org. Chem.*, **74**(2):487–498, **2009**.

[29] Probst-Rüd, B. "Photocatalytic Hydrogen Production". PhD thesis, University of Zurich, Institute of Inorganic Chemistry, **2010**.

[30] Fujishima, A. and Honda, K. "Electrochemical photolysis of water at a semiconductor electrode" *Nature*, **138**(5358):37–38, **1972**.

[31] Maeda, K. "Photocatalytic water splitting using semiconductor particles: history and recent developments" *J. Photochem. Photobiol., C*, **12**(4):237–268, **2011**.

[32] West, A. R. "Basic solid state chemistry". John Wiley & Sons, Chichester, 2nd edition, **1999**.

[33] Müller, U. "Anorganische Strukturchemie". Vieweg + Teubner, GWV Fachverlage, Wiesbaden, 6th edition, **2008**.

[34] Duffy, J. A. "Bonding, energy levels & bands in inorganic solids". Longman Scientific & Technical, **1990**.

[35] Kudo, A. and Miseki, Y. "Heterogeneous photocatalyst materials for water splitting" *Chem. Soc. Rev.*, **38**(1):253–278, **2008**.

[36] Kumar, S. K. and Devi, L. G. "Review on modified TiO_2 photocatalysis under UV/visible light: selected results and related mechanisms on interfacial charge carrier transfer dynamics" *J. Phys. Chem. A*, **115**(46):13211–13241, **2011**.

[37] Fujishima, A., Rao, T. N., and Tryk, D. A. "Titanium dioxide photocatalysis" *J. Photochem. Photobiol., C*, **1**(1):1–21, **2000**.

[38] Osterloh, F. E. "Inorganic materials as catalysts for photochemical splitting of water" *Chem. Mater.*, **20**(1):35–54, **2008**.

[39] Izumi, Y. "Recent advances in the photocatalytic conversion of carbon dioxide to fuels with water and/or hydrogen using solar energy and beyond" *Coord. Chem. Rev.*, **257**(1):171–186, **2013**.

[40] Ravelli, D., Fagnoni, M., and Albini, A. "Photoorganocatalysis. What for?" *Chem. Soc. Rev.*, **42**(1):97–113, **2013**.

[41] Memming, R. "Semiconductor electrochemistry". Wiley-VCH, **2001**.

[42] Scaife, D. E. "Oxide semiconductors in photoelectrochemical conversion of solar energy" *Sol. Energy*, **25**:41–54, **1980**.

[43] Bisquert, J. and Garcia-Belmonte, G. "On voltage, photovoltage, and photocurrent in bulk heterojunction organic solar cells" *J. Phys. Chem. Lett.*, **2**(15):1950–1964, **2011**.

[44] Zhang, Z. and Yates, J. T. "Band bending in semiconductors: chemical and physical consequences at surfaces and interfaces" *Chem. Rev. (Washington, DC, U. S.)*, **112**(10):5520–5551, **2012**.

[45] Hering, E., Martin, R., and Stohrer, M. "Physik für Ingenieure". Springer Verlag, Berlin, 9th edition, **2004**.

[46] Nozik, A. J. "Photoelectrochemistry: applications to solar energy conversion" *Annu. Rev. Phys. Chem.*, **29**:189–222, **1978**.

[47] Serpone, N. and Pelizzetti, E., editors. "Photocatalysis: fundamentals and applications". Wiley Interscience, New York, **1989**.

[48] Hong, S. Y., Lee, S., Jang, J. S., and Lee, J. S. "Heterojunction $BiVO_4$/WO_3 electrodes for enhanced photoactivity of water oxidation" *Energy Environ. Sci.*, **4**(5):1781–1787, **2011**.

[49] Umezawa, N., Shuxin, O., and Ye, J. "Theoretical study of high photocatalytic performance of Ag_3PO_4" *Phys. Rev. B: Condens. Matter Mater. Phys.*, **83**(3):035202 1–8, **2011**.

[50] Kato, H., Asakura, K., and Kudo, A. "Highly efficient water splitting into H_2 and O_2 over lanthanum-doped $NaTaO_3$ photocatalysts with high crystallinity and surface nanostructure" *J. Am. Chem. Soc.*, **125**(10):3082–3089, **2003**.

[51] Tong, H., Ouyang, S., Bi, Y. *et al.* "Nano-photocatalytic materials: possibilities and challenges" *Adv. Mater.*, **24**(2):229–251, **2012**.

[52] Maeda, K., Takata, T., Hara, M. *et al.* "GaN:ZnO solid solution as a photocatalyst for visible-light-driven overall water splitting" *J. Am. Chem. Soc.*, **127**(23):8286–8287, **2005**.

[53] Yi, Z., Ye, J., Kikugawa, N. *et al.* "An orthophosphate semiconductor with photooxidation properties under visible-light irradiation" *Nat. Mater.*, **9**(7):559–564, **2010**.

[54] Maeda, K. and Domen, K. "Solid solution of GaN and ZnO as a stable photocatalyst for overall water splitting under visible-light" *Chem. Mater.*, **22**(3):612–623, **2010**.

[55] Ogisu, K., Ishikawa, A., Teramuro, K. *et al.* "Lanthanum-indium oxysulfide as a visible-light driven photocatalyst for water splitting" *Chem. Lett.*, **36**(7):854–855, **2007**.

[56] Allred, A. "Electronegativity values from thermochemical data" *J. Inorg. Nucl. Chem.*, **17**(3–4):215–221, **1961**.

[57] Anta, J. A. "Electron transport in nanostructured metal-oxide semiconductors" *Curr. Opin. Colloid Interface Sci.*, **17**(3):124–131, **2012**.

[58] Yin, W.-J., Wei, S.-H., Al-Jassim, M. M. *et al.* "Doping properties of monoclinic $BiVO_4$ studied by first-principles density-functional theory" *Phys. Rev. B: Condens. Matter Mater. Phys.*, **83**(15):155102 1–11, **2011**.

[59] Duffy, J. A. "Chemical bonding in the oxides - a new appraisal" *J. Solid State Chem.*, **62**(2):145–157, **1986**.

[60] Duffy, J. A. "Ultraviolet transparency of glass: a chemical approach in terms of band theory, polarisability and electronegativity" *Phys. Chem. Glasses*, **42**(3):151–157, **2001**.

[61] Bak, T., Nowotny, J., Rekas, M., and Sorrell, C. C. "Photo-electrochemical hydrogen generation from water using solar energy. materials-related aspects" *Int. J. Hydrogen Energy*, **27**(10):991–1022, **2002**.

[62] Carp, O., Huisman, C. L., and Reller, A. "Photoinduced reactivity of titanium dioxide" *Prog. Solid State Chem.*, **32**(1–2):33–177, **2004**.

[63] Liao, P. and Carter, E. A. "New concepts and modeling strategies to design and evaluate photo-electro-catalysts based on transition metal oxides" *Chem. Soc. Rev.*, **42**(6):2401–2422, **2013**.

[64] Cowan, A. J. and Durrant, J. R. "Long-lived charge separated states in nanostructured semiconductor photoelectrodes for the production of solar fuels" *Chem. Soc. Rev.*, **42**(6):2281–2293, **2013**.

[65] Wilker, M. B., Schnitzenbaumer, K. J., and Dukovic, G. "Recent progress in photocatalysis mediated by colloidal II-VI nanocrystals" *Isr. J. Chem.*, **52**(11–12):1002–1015, **2012**.

[66] Takanabe, K. and Domen, K. "Preparation of inorganic photocatalytic materials for overall water splitting" *ChemCatChem*, **4**(10):1485–1497, **2012**.

[67] Chatchai, P., Kishioka, S.-y., Murakami, Y. *et al.* "Enhanced photoelectrocatalytic activity of FTO/WO_3/$BiVO_4$ electrode modified with gold nanoparticles for water oxidation under visible-light irradiation" *Electrochim. Acta*, **55**(3):592–596, **2010**.

[68] Zhang, X., Chen, Y. L., Liu, R.-S., and Tsai, D. P. "Plasmonic photocatalysis" *Rep. Prog. Phys.*, **76**(4):046401 1–41, **2013**.

[69] Leoni, M., Confente, T., and Scardi, P. "PM2K: a flexible program implementing whole powder pattern modelling" *Z. Kristallogr. Suppl.*, **2006**(23):249–254, **2006**.

[70] Leoni, M. and Scardi, P. "Line profile analysis: pattern modelling versus profile fitting" *J. Appl. Crystallogr.*, **39**(1):24–31, **2006**.

[71] Scardi, P., Dong, Y. H., and Leoni, M. "Line profile analysis in the Rietveld method and whole-powder-pattern fitting" *Mater. Sci. Forum*, **378–381**:132–141, **2001**.

[72] Praus, P., Kozák, O., Kočí, K. *et al.* "CdS nanoparticles deposited on montmorillonite: preparation, characterization and application for photoreduction of carbon dioxide" *J. Colloid Interface Sci.*, **360**(2):574–579, **2011**.

[73] Nollé, . L. and Shchelev, M. Y. "Photoelectron emission caused by surface plasmons in silver nanoparticles" *Tech. Phys. Lett.*, **30**(4):304–306, **2004**.

[74] Tauc, J., Grigorovici, R., and Vancu, A. "Optical properties and electronic structure of amorphous germanium" *Phys. Status Solidi B*, **15**(2):627–637, **1966**.

[75] Kumar, V., Sharma, S. K., Sharma, T. P., and Singh, V. "Band gap Determination in thick films from reflectance measurements" *Opt. Mater. (Amsterdam, Neth.)*, **12**(1):115–119, **1999**.

[76] Mills, A. and Wang, J. "Photobleaching of methylene blue sensitised by TiO_2: an ambiguous system?" *J. Photochem. Photobiol., A*, **127**(1–3):123–134, **1999**.

[77] Hernandez-Alonso, M. D., Fresno, F., Suarez, S., and Coronado, J. M. "Development of alternative photocatalysts to TiO_2: challenges and opportunities" *Energy Environ. Sci.*, **2**:1231–1257, **2009**.

[78] Kudo, A., Ueda, K., Kato, H., and Mikami, I. "Photocatalytic O_2 evolution under visible-light irradiation on $BiVO_4$ in aqueous $AgNO_3$ solution" *Catal. Lett.*, **53**(3–4):229–230, **1998**.

[79] Kato, H., Hori, M., Konta, R. *et al.* "Construction of z-scheme type heterogeneous photocatalysis systems for water splitting into H_2 and O_2 under visible-light irradiation" *Chem. Lett.*, **33**(10):1348–1349, **2004**.

[80] Sasaki, Y., Kato, H., and Kudo, A. "$[Co(bpy)_3]^{3+/2+}$ and $[Co(phen)_3]^{3+/2+}$ electron mediators for overall water splitting under sunlight irradiation using z-scheme photocatalyst system" *J. Am. Chem. Soc.*, **135**(14):5441–5449, **2013**.

[81] Bierlein, J. D. and Sleight, A. W. "Ferroelasticity in $BiVO_4$" *Solid State Commun.*, **16**(1):69–70, **1975**.

[82] Kudo, A., Omori, K., and Kato, H. "A novel aqueous process for preparation of crystal form-controlled and highly crystalline $BiVO_4$ powder from layered vanadates at room temperature and its photocatalytic and photophysical properties" *J. Am. Chem. Soc.*, **121**(49):11459–11467, **1999**.

[83] Yu, J., Zhang, Y., and Kudo, A. "Synthesis and photocatalytic performances of $BiVO_4$ by ammonia co-precipitation process" *J. Solid State Chem.*, **182**(2):223–228, **2009**.

[84] Zhang, H.-M., Liu, J.-B., Wang, H. *et al.* "Rapid microwave-assisted synthesis of phase controlled $BiVO_4$ nanocrystals and research on photocatalytic properties under visible-light irradiation" *J. Nanopart. Res.*, **10**(5):767–774, **2008**.

[85] Liu, W., Cao, L., Su, G. *et al.* "Ultrasound assisted synthesis of monoclinic structured spindle $BiVO_4$ particles with hollow structure and its photocatalytic property" *Ultrason. Sonochem.*, **17**(4):669–674, **2010**.

[86] Chatchai, P., Murakami, Y., ya Kishioka, S. *et al.* "Efficient photocatalytic activity of water oxidation over WO_3/$BiVO_4$ composite under visible-light irradiation" *Electrochim. Acta*, **54**(3):1147–1152, **2009**.

[87] Dolgos, M. R., Paraskos, A. M., Stoltzfus, M. W. *et al.* "The electronic structures of vanadate salts: cation substitution as a tool for band gap manipulation" *J. Solid State Chem.*, **182**(7):1964–1971, **2009**.

[88] Su, J., Guo, L., Yoriya, S., and Grimes, C. A. "Aqueous growth of pyramidal-shaped $BiVO_4$ nanowire arrays and structural characterization: application to photoelectrochemical water splitting" *Cryst. Growth Des.*, **10**(2):856–861, **2010**.

[89] Ge, L. "Synthesis and characterization of novel visible-light-driven Pd/$BiVO_4$ composite photocatalysts" *Mater. Lett.*, **62**(6–7):926–928, **2008**.

[90] Kohtani, S., Hiro, J., Yamamoto, N. *et al.* "Adsorptive and photocatalytic properties of Ag-loaded $BiVO_4$ on the degradation of 4-n-alkylphenols under visible-light irradiation" *Catal. Commun.*, **6**(3):185–189, **2005**.

[91] Xu, H., Li, H., Wu, C. *et al.* "Preparation, characterization and photocatalytic properties of Cu-loaded $BiVO_4$" *J. Hazard. Mater.*, **153**(1–2):877–884, **2008**.

[92] Zhang, A. and Zhang, J. "Effects of europium doping on the photocatalytic behavior of $BiVO_4$" *J. Hazard. Mater.*, **173**(1–3):265–272, **2010**.

[93] Jing, D., Liu, M., Shi, J. *et al.* "Hydrogen production under visible-light by photocatalytic reforming of glucose over an oxide solid-solution photocatalyst" *Catal. Commun.*, **12**(4):264–267, **2010**.

[94] Pilli, S. K., Deutsch, T. G., Furtak, T. E. *et al.* "$BiVO_4$/$CuWO_4$ heterojunction photoanodes for efficient solar driven water oxidation" *Phys. Chem. Chem. Phys.*, **15**(9):3273–3278, **2013**.

[95] Pilli, S. K., Janarthanan, R., Deutsch, T. G. *et al.* "Efficient photoelectrochemical water oxidation over cobalt-phosphate (Co-Pi) catalyst modified $BiVO_4$/1D-WO_3 heterojunction electrodes" *Phys. Chem. Chem. Phys.*, **15**(35):14723–14728, **2013**.

[96] Su, J., Zou, X.-X., Li, G.-D. *et al.* "Macroporous V_2O_5-$BiVO_4$ composites: effect of heterojunction on the behavior of photogenerated charges" *J. Phys. Chem. C*, **115**(16):8064–8071, **2011**.

[97] Beale, A. M., Le, M., Hoste, S., and Sankar, G. "A time resolved *in situ* investigation into the formation of bismuth molybdate catalysts prepared by spray-dried methods" *Solid State Sci.*, **7**(10):1141–1148, **2005**.

[98] Bégué, P., Enjalbert, R., Galy, J., and Castro, A. "Single-crystal x-ray investigations of the structures of γ-(H)Bi_2MoO_6 and its partially substituted As^{3+} and Sb^{3+} homologues" *Solid State Sci.*, **2**(6):637–653, **2000**.

[99] Yao, W. and Ye, J. "Photophysical and photocatalytic properties of $Ca_{1-x}Bi_xV_xMo_{1-x}O_4$ solid solutions" *J. Phys. Chem. B*, **110**(23):11188–11195, **2006**.

[100] Yao, W., Iwai, H., and Ye, J. "Effects of molybdenum substitution on the photocatalytic behavior of $BiVO_4$" *Dalton Trans.*, **2008**(11):1426–1430, **2008**.

[101] Guo, W., Ward, T. L., Porter, C., and Datye, A. K. "Phase content and particle morphology of Bi-Mo-V-O powders produced by aerosol pyrolysis" *Mater. Res. Bull.*, **40**(8):1371–1387, **2005**.

[102] Park, H. S., Lee, H. C., Leonard, K. C. *et al.* "Unbiased photoelectrochemical water splitting in z-scheme device using W/Mo-doped $BiVO_4$ and $Zn_xCd_{1-x}Se$" *ChemPhysChem*, **14**(10):2277–2287, **2013**.

[103] Jeong, H. W., Jeon, T. H., Jang, J. S. *et al.* "Strategic modification of $BiVO_4$ for improving photoelectrochemical water oxidation performance" *J. Phys. Chem. C*, **117**(18):9104–9112, **2013**.

[104] Zhang, K., Shi, X.-J., Kim, J. K., and Park, J. H. "Photoelectrochemical cells with tungsten trioxide/Mo-doped $BiVO_4$ bilayers" *Phys. Chem. Chem. Phys.*, **14**(31):11119–11124, **2012**.

[105] Cesari, M., Perego, G., Zazzetta, A. *et al.* "The crystal structures of the bismuth molybdovanadates and of the α-phase bismuth molybdate" *J. Inorg. Nucl. Chem.*, **33**(10):3595–3597, **1971**.

[106] Gruar, R., Tighe, C. J., Reilly, L. M. *et al.* "Tunable and rapid crystallisation of phase pure Bi_2MoO_6 (koechlinite) and $Bi_2Mo_3O_{12}$ via continuous hydrothermal synthesis" *Solid State Sci.*, **12**(9):1683–1686, **2010**.

[107] Ueda, W., Asakawa, K., Chen, C.-L. *et al.* "Catalytic properties of tricomponent metal oxides having the scheelite structure: I. role of bulk diffusion of lattice oxide ions in the oxidation of propylene" *J. Catal.*, **101**(2):360–368, **1986**.

[108] Hartmanova, M., Le, M. T., Jergel, M. *et al.* "Structure and electrical conductivity of multicomponent metal oxides having scheelite structure" *Russ. J. Electrochem.*, **45**(6):621–629, **2009**.

[109] Samant, M. S., Kerkar, A. S., Bharadwaj, S. R., and Dharwadkar, S. R. "Thermodynamic investigation of the vaporization of molybdenum trioxide" *J. Alloys Compd.*, **187**(2):373–379, **1992**.

[110] Ji, T.-h., Yang, F., Zhou, J.-y. *et al.* "Visible-light responding $BiVO_4/TiO_2$ nanocomposite photocatalyst" *Spectrosc. Spectral Anal. (Beijing, China)*, **30**(7):1944–1947, **2010**.

[111] Hu, Y., Li, D., Zheng, Y. *et al.* "$BiVO_4/TiO_2$ nanocrystalline heterostructure: a wide spectrum responsive photocatalyst towards the highly efficient decomposition of gaseous benzene" *Appl. Catal., B*, **104**(1–2):30–36, **2011**.

[112] Murakami, Y., Chatchai, P., and Nosaka, Y. "Developments of the efficient water-splitting electrodes under the visible-light irradiation" *Electrochemistry (Tokyo, Jpn.)*, **77**(1):44–50, **2009**.

[113] Hardcastle, F. D., Wachs, I. E., Eckert, H., and Jefferson, D. A. "Vanadium(V) environments in bismuth vanadates: a structural investigation using Raman spectroscopy and solid state ^{51}V NMR" *J. Solid State Chem.*, **90**(2):194–210, **1991**.

[114] Weinstock, N., Schulze, H., and Müller, A. "Assignment of ν_2(E) and ν_4(F_2) of tetrahedral species by the calculation of the relative Raman intensities: the vibrational spectra of VO_4^{3-}, CrO_4^{2-}, MoO_4^{2-}, WO_4^{2-}, MnO_4^-, TcO_4^-, ReO_4^-, RuO_4, and OsO_4" *J. Chem. Phys.*, **59**(9):5063–5067, **1973**.

[115] Pless, J. D., Kim, H.-S., Smit, J. P. *et al.* "Structure of $Mg_{2.56}V_{1.12}W_{0.88}O_8$ and vibrational Raman spectra of $Mg_{2.5}VWO_8$ and $Mg_{2.5}VMoO_8$" *Inorg. Chem.*, **45**(2):514–520, **2006**.

[116] Sun, Y. J., Liu, H. J., Wang, X. *et al.* "Optical spectroscopy and visible upconversion studies of YVO_4 : Er^{3+} nanocrystals synthesized by a hydrothermal process" *Chem. Mater.*, **18**(11):2726–2732, **2006**.

[117] Zhou, Y., Vuille, K., Heel, A. *et al.* "An inorganic hydrothermal route to photocatalytically active bismuth vanadate" *Appl. Catal., A*, **375**(1):140–148, **2010**.

[118] Lü, X., Ding, S., Xie, Y., and Huang, F. "Non-aqueous preparation of high-crystallinity hierarchical TiO_2 hollow spheres with excellent photocatalytic efficiency" *Eur. J. Inorg. Chem.*, **2011**(18):2879–2883, **2011**.

[119] Zhou, Y., Pienack, N., Bensch, W., and Patzke, G. R. "The interplay of crystallization kinetics and morphology in nanostructured W/Mo oxide formation: an *in situ* diffraction study" *Small*, **5**(17):1978–1983, **2009**.

[120] Thiruvengadathan, R., Korampally, V., Ghosh, A. *et al.* "Nanomaterial processing using self-assembly-bottom-up chemical and biological approaches" *Rep. Prog. Phys.*, **76**(6):066501 1–54, **2013**.

[121] Liu, G., Yu, J. C., Lu, G. Q. M., and Cheng, H.-M. "Crystal facet engineering of semiconductor photocatalysts: motivations, advances and unique properties" *Chem. Commun. (Cambridge, U. K.)*, **47**:6763–6783, **2011**.

[122] Khon, E., Lambright, K., Khnayzer, R. S. *et al.* "Improving the catalytic activity of semiconductor nanocrystals through selective domain etching" *Nano Lett.*, **13**(5):2016–2023, **2013**.

[123] Li, G., Zhang, D., and Yu, J. C. "Ordered mesoporous $BiVO_4$ through nanocasting: a superior visible-light driven photocatalyst" *Chem. Mater.*, **20**(12):3983–3992, **2008**.

[124] Ke, D., Peng, T., Ma, L. *et al.* "Effects of hydrothermal temperature on the microstructures of $BiVO_4$ and its photocatalytic O_2 evolution activity under visible-light" *Inorg. Chem.*, **48**(11):4685–4691, **2009**.

[125] Yin, W., Wang, W., Zhou, L. *et al.* "CTAB-assisted synthesis of monoclinic $BiVO_4$ photocatalyst and its highly efficient degradation of organic dye under visible-light irradiation" *J. Hazard. Mater.*, **173**(1–3):194–199, **2010**.

[126] Xi, G. and Ye, J. "Synthesis of bismuth vanadate nanoplates with exposed $\{001\}$ facets and enhanced visible-light photocatalytic properties" *Chem. Commun. (Cambridge, U. K.)*, **46**(11):1893–1895, **2010**.

[127] Zhang, L., Chen, D., and Jiao, X. "Monoclinic structured $BiVO_4$ nanosheets: hydrothermal preparation, formation mechanism, and coloristic and photocatalytic properties" *J. Phys. Chem. B*, **110**(6):2668–2673, **2006**.

[128] Meng, X., Zhang, L., Dai, H. *et al.* "Surfactant-assisted hydrothermal fabrication and visible-light-driven photocatalytic degradation of methylene blue over multiple morphological $BiVO_4$ Single-crystallites" *Mater. Chem. Phys.*, **125**(1–2):59–65, **2011**.

[129] Patzke, G. R., Zhou, Y., Kontic, R., and Conrad, F. "Oxide nanomaterials: synthetic developments, mechanistic studies, and technological innovations" *Angew. Chem., Int. Ed.*, **50**(4):826–859, **2011**.

[130] Zhang, A. and Zhang, J. "Characterization of visible-light-driven $BiVO_4$ photocatalysts synthesized via a surfactant-assisted hydrothermal method" *Spectrochim. Acta, Part A*, **73**(2):336–341, **2009**.

[131] Martínez-de la Cruz, A. and García Pérez, U. M. "Photocatalytic properties of $BiVO_4$ prepared by the co-precipitation method: degradation of rhodamine B and possible reaction mechanisms under visible irradiation" *Mater. Res. Bull.*, **45**(2):135–141, **2010**.

[132] Payne, D. J., Robinson, M. D. M., Egdell, R. G. *et al.* "The nature of electron lone pairs in $BiVO_4$" *Appl. Phys. Lett.*, **98**(21):212110 1–3, **2011**.

[133] Yu, J. and Kudo, A. "Effects of structural variation on the photocatalytic performance of hydrothermally synthesized $BiVO_4$" *Adv. Funct. Mater.*, **16**(16):2163–2169, **2006**.

[134] Kim, D. and Huh, Y.-D. "Morphology-dependent photocatalytic activities of hierarchical microstructures of ZnO" *Mater. Lett.*, **65**(14):2100–2103, **2011**.

[135] Ryu, M., Ahn, J., You, K. *et al.* "Synthesis of calcium carbonate in ethanol-ethylene glycol solvent" *J. Ceram. Soc. Jpn.*, **117**(1361):106–110, **2009**.

[136] Schwarz, K. and Epple, M. "Biomimetic crystallization of apatite in a porous polymer matrix" *Chem. – Eur. J.*, **4**(10):1898–1903, **1998**.

[137] Kniep, R. and Busch, S. "Biomimetic growth and self-assembly of fluorapatite aggregates by diffusion into denatured collagen matrices" *Angew. Chem., Int. Ed.*, **35**(22):2624–2626, **1996**.

[138] McIntyre, S. K. and Alam, T. M. "^{17}O NMR investigation of phosphite hydrolysis mechanisms" *Magn. Reson. Chem.*, **45**(12):1022–1026, **2007**.

[139] Westheimer, F. H., Huang, S., and Covitz, F. "Rates and mechanisms of hydrolysis of esters of phosphorous acid" *J. Am. Chem. Soc.*, **110**(1):181–185, **1988**.

[140] Saison, T., Chemin, N., Chanéac, C. *et al.* "Bi_2O_3, $BiVO_4$, and Bi_2WO_6: impact of surface properties on photocatalytic activity under visible light" *J. Phys. Chem. C*, **115**(13):5657–5666, **2011**.

[141] Liu, G., Li, X., Zhao, J. *et al.* "Photooxidation pathway of sulforhodamine-B. Dependence on the adsorption mode on TiO_2 exposed to visible light radiation" *Environ. Sci. Technol.*, **34**(18):3982–3990, **2000**.

[142] Kohtani, S., Yoshida, K., Maekawa, T. *et al.* "Loading Effects of Silver Oxides upon Generation of Reactive Oxygen Species in Semiconductor Photocatalysis" *Phys. Chem. Chem. Phys.*, **10**(20):2986–2992, **2008**.

[143] Osterloh, F. E. "Inorganic nanostructures for photoelectrochemical and photocatalytic water splitting" *Chem. Soc. Rev.*, **42**(6):2294–2320, **2013**.

[144] Kubacka, A., Fernández-García, M., and Colón, G. "Advanced nanoarchitectures for solar photocatalytic applications" *Chem. Rev. (Washington, DC, U. S.)*, **112**(3):1555–1614, **2012**.

[145] Ye, J., Zou, Z., Oshikiri, M. *et al.* "A novel hydrogen-evolving photocatalyst $InVO_4$ active under visible light irradiation" *Chem. Phys. Lett.*, **356**(3–4):221–226, **2002**.

[146] Amarilla, J. M., Casal, B., and Ruiz-Hitzky, E. "Synthesis and characterization of the new mixed oxide $NbVO_5$" *Mater. Lett.*, **8**(3–4):132–136, **1989**.

[147] Polte, A. and Langbein, H. "Formation and transformation of oxide phases in the quasi-binary system V_2O_5-Nb_2O_5" *Z. Anorg. Allg. Chem.*, **620**(11):1947–1952, **1994**.

[148] Chahboun, H., Groult, D., and Raveau, B. "$TaVO_5$, a novel derivative of the series of monophosphate tungsten bronzes $(PO_2)_4(WO_3)_{2m}$" *Mater. Res. Bull.*, **23**(6):805–812, **1988**.

[149] Wang, J., Deng, J., Yu, R. *et al.* "Coprecipitation synthesis and negative thermal expansion of $NbVO_5$" *Dalton Trans.*, **40**(13):3394–3397, **2011**.

[150] Wang, X., Huang, Q., Deng, J. *et al.* "Phase transformation and negative thermal expansion in $TaVO_5$" *Inorg. Chem.*, **50**(6):2685–2690, **2011**.

[151] Krins, N., Bass, J. D., Grosso, D. *et al.* "$NbVO_5$ mesoporous thin films by evaporation induced micelles packing: pore size dependence of the mechanical stability upon thermal treatment and Li insertion/extraction" *Chem. Mater.*, **23**(18):4124–4131, **2011**.

[152] Amarilla, J. M., Casal, B., and Ruiz-Hitzky, E. "MVO_5 (M = Nb, Ta) mixed oxides: sol-gel synthesis, structural and thermal characterization and electrochemical Li^+ insertion" *J. Mater. Chem.*, **6**(6):1005–1011, **1996**.

[153] Barbieri, F., Cauzzi, D., De Smet, F. *et al.* "Mixed-oxide catalysts involving V, Nb and Si obtained by a non-hydrolytic sol-gel route: preparation and catalytic behaviour in oxydative dehydrogenation of propane" *Catal. Today*, **61**(1–4):353–360, **2000**.

[154] Dhachapally, N., Kalevaru, V. N., Brückner, A., and Martin, A. "Metal vanadate catalysts for the ammoxidation of 2-methylpyrazine to 2-cyanopyrazine" *Appl. Catal., A*, **443–444**:111–118, **2012**.

[155] Yamaguchi, O., Mukaida, Y., and Shigeta, H. "New compounds in the Nb_2O_5(Ta_2O_5)-V_2O_5 systems" *Z. Anorg. Allg. Chem.*, **574**(7):235–238, **1989**.

[156] Börrnert, C., Carillo-Cabrera, W., Simon, P., and Langbein, H. "$V_{2.38}Nb_{10.7}O_{32.7}$: a V_2O_5-Nb_2O_5 mixed oxide tunnel structure related to the tetragonal tungsten bronzes" *J. Solid State Chem.*, **183**(5):1038–1045, **2010**.

[157] Börrnert, C., Zosel, J., Polte, A. *et al.* "Temperature-dependent oxygen release, intercalation behaviour and catalytic properties of V_2O_5-Nb_2O_5 compounds" *Mater. Res. Bull.*, **46**(11):1955–1962, **2011**.

[158] Pozas, R., Madueño, S., Bruque, S. *et al.* "Lithium insertion in vanadyl phosphate" *Solid State Ionics*, **51**(12):79–83, **1992**.

[159] Gaubicher, J., Le Mercier, T., Chabre, Y. *et al.* "Li/β-$VOPO_4$: a new 4V system for lithium batteries" *J. Electrochem. Soc.*, **146**(12):4375–4379, **1999**.

[160] Whittingham, M. S., Song, Y., Lutta, S. *et al.* "Some transition metal (oxy)phosphates and vanadium oxides for lithium batteries" *J. Mater. Chem.*, **15**(33):3362–3379, **2005**.

[161] Seeboth, H., Kubias, B., Wolf, H., and Lucke, B. "Studies of selective oxidation of butene into maleic-anhydride on vanadium phosphate catalysts: 2. Catalytic oxidation of butene into maleic anhydride on $(VO)_2P_2O_7$ and α-$VOPO_4$" *Chem. Tech. (Leipzig, Ger.)*, **28**(12):730–734, **1976**.

[162] Lashier, M. E. and Schrader, G. L. "Reactive lattice oxygen sites for C_4-hydrocarbon selective oxidation over β-$VOPO_4$" *J. Catal.*, **128**(1):113–125, **1991**.

[163] Hutchings, G. J., Sananes, M. T., Sajip, S. *et al.* "Improved method of preparation of vanadium phosphate catalysts" *Catal. Today*, **33**(1–3):161–171, **1997**.

[164] Shin, Y.-G. K., Saari, E. A., Torgerson, M. R., and Nocera, D. G. "Design of layered phosphate hosts containing multiply bonded bimetallic guest species" *ACS Symp. Ser.*, **517**:244–259, **1993**.

[165] Beneš, L., Melánová, K., Svoboda, J., and Zima, V. "Intercalation chemistry of layered vanadyl phosphate: a review" *J. Inclusion Phenom. Macrocyclic Chem.*, **73**(1–4):33–53, **2012**.

[166] Sun, Y., Li, C., Wang, L. *et al.* "Ultralong monoclinic ZnV_2O_6 nanowires: their shape-controlled synthesis, new growth mechanism, and highly reversible lithium storage in lithium-ion batteries" *RSC Adv.*, **2**(21):8110–8115, **2012**.

[167] Klissurski, D., Ivanov, K., Dimitrov, D. *et al.* "Catalytic oxidation of methanol on mechanochemically obtained ZnV_2O_6 catalysts" *C. R. Acad. Bulg. Sci.*, **63**(5):693–698, **2010**.

[168] Chen, Z., Huang, W., Lu, D. *et al.* "Hydrothermal synthesis and electrochemical properties of crystalline $Zn_2V_2O_7$ nanorods" *Mater. Lett.*, **107**:35–38, **2013**.

[169] Clark, S. J., Segall, M. D., Pickard, C. J. *et al.* "First principles methods using CASTEP" *Z. Kristallogr.*, **220**(5–6):567–570, **2005**.

[170] Perdew, J. P., Burke, K., and Ernzerhof, M. "Generalized gradient approximation made simple" *Phys. Rev. Lett.*, **77**(18):3865–3868, **1996**.

[171] Tkatchenko, A. and Scheffler, M. "Accurate molecular van der Waals interactions from ground-state electron density and free-atom reference data" *Phys. Rev. Lett.*, **102**(7):073005 1–4, **2009**.

[172] Perdew, J. P., Chevary, J. A., Vosko, S. H. *et al.* "Atoms, molecules, solids, and surfaces: applications of the generalized gradient approximation for exchange and correlation" *Phys. Rev. B: Condens. Matter Mater. Phys.*, **46**(11):6671–6687, **1992**.

[173] Ortmann, F., Bechstedt, F., and Schmidt, W. G. "Semiempirical van der Waals correction to the density functional description of solids and molecular structures" *Phys. Rev. B: Condens. Matter Mater. Phys.*, **73**(20):205101 1–10, **2006**.

[174] Andreetti, G. D., Calestani, G., Montenero, A., and Bettinelli, M. "Refinement of the crystal structure of ZnV_2O_6" *Z. Kristallogr.*, **168**(1–4):53–58, **1984**.

[175] Deschizeaux-Chéruy, M. N., Aubert, J. J., and Joubert, J. C. "Relation entre structure et conductivité ionique basse temperature de Ag_3PO_4" *Solid State Ionics*, **7**(2):171–176, **1982**.

[176] Sleight, A. W., Chen, H., and Ferretti, A. "Crystal growth and structure of $BiVO_4$" *Mater. Res. Bull.*, **14**(12):1571–1581, **1979**.

[177] Keller, C. "Über ternäre Oxide des Niobs und Tantals von Typ ABO_4" *Z. Anorg. Allg. Chem.*, **318**(1–2):89–106, **1962**.

[178] Tachez, M., Theobald, F., and Bordes, E. "A structural explanation for the polymorphism of the α-form of anhydrous vanadyl phosphate" *J. Solid State Chem.*, **40**(3):280–283, **1981**.

[179] Gopal, R. and Calvo, C. "Crystal-Structure of β-VPO_5" *J. Solid State Chem.*, **5**(3):432–435, **1972**.

[180] Gopal, R. and Calvo, C. "Crystal Structure of α-$Zn_2V_2O_7$" *Can. J. Chem.*, **51**(7):1004–1009, **1973**.

[181] Perdew, J. P. "Density functional theory and the band gap problem" *Int. J. Quantum Chem.*, **28**(S19):497–523, **1985**.

[182] Oshikiri, M., Boero, M., Ye, J. *et al.* "Electronic structures of promising photocatalysts $InMO_4$ (M=V, Nb, Ta) and $BiVO_4$ for water decompositon in the visible wavelength region" *J. Chem. Phys.*, **117**(15):7313–7318, **2002**.

[183] Walsh, A., Yan, Y., Huda, M. N. *et al.* "Band edge electronic structure of $BiVO_4$: elucidating the role of the Bi *s* and V *d* orbitals" *Chem. Mater.*, **21**(3):547–551, **2009**.

[184] Zhao, Z., Li, Z., and Zou, Z. "Electronic structure and optical properties of monoclinic clinobisvanite $BiVO_4$" *Phys. Chem. Chem. Phys.*, **13**(10):4746–4753, **2011**.

[185] Park, H. S., Kweon, K. E., Ye, H. *et al.* "Factors in the metal doping of $BiVO_4$ for improved photoelectrocatalytic activity as studied by scanning electrochemical microscopy and first-principles density-functional calculation" *J. Phys. Chem. C*, **115**(36):17870–17879, **2011**.

[186] Fratzky, D., Götze, T., Worzala, H., and Meisel, M. "The formation of vanadyl phosphate hydrates from aqueous phase: a systematic study" *Mater. Res. Bull.*, **33**(4):635–643, **1998**.

[187] Ladwig, G. "Über die Konstitution des $VPO_5(nH_2O)$" *Z. Anorg. Allg. Chem.*, **338**(5–6):266–278, **1965**.

[188] Gregory, D. H. "Structural families in nitride chemistry" *J. Chem. Soc., Dalton Trans.*, **1999**(3):259–270, **1999**.

[189] Ebbinghaus, S. G., Abicht, H.-P., Dronskowski, R. *et al.* "Perovskite-related oxynitrides — recent developments in synthesis, characterisation and investigations of physical properties" *Prog. Solid State Chem.*, **37**(2–3):173–205, **2009**.

[190] Giordano, C., Erpen, C., Yao, W. *et al.* "Metal nitride and metal carbide nanoparticles by a soft urea pathway" *Chem. Mater.*, **21**(21):5136–5144, **2009**.

[191] Buha, J., Djerdj, I., Antonietti, M., and Niederberger, M. "Thermal transformation of metal oxide nanoparticles into nanocrystalline metal nitrides using cyanamide and urea as nitrogen source" *Chem. Mater.*, **19**(14):3499–3505, **2007**.

[192] Hartwig, A. "Römpp Online: *Zink*". *http://www.roempp.com/prod/*, last checked: 08/2013.

[193] Shannon, R. D. "Revised effective ionic radii and systematic studies of interatomic distances in halides and chalcogenides" *Acta Crystallogr., Sect. A: Cryst. Phys., Diffr., Theor. Gen. Crystallogr.*, **32**(5):751–767, **1976**.

[194] Wang, Y., Wang, X., and Antonietti, M. "Polymeric graphitic carbon nitride as a heterogeneous organocatalyst: from photochemistry to multipurpose catalysis to sustainable chemistry" *Angew. Chem., Int. Ed.*, **51**(1):68–89, **2012**.

[195] Patzke, G. R., Kontic, R., Shiolashvili, Z. *et al.* "Hydrazine-assisted formation of indium phosphide (InP)-based nanowires and core-shell composites" *Materials*, **6**(1):85–100, **2013**.

[196] Jishiashvili, D., Kapaklis, V., Devaux, X. *et al.* "Germanium nitride nanowires produced by thermal annealing in hydrazine vapor" *Adv. Sci. Lett.*, **2**(1):40–44, **2009**.

[197] Patzke, G. R. and Jishiashvili, D. "SCOPES interim scientific report". JRP/IP: IZ73Z0_127943/1, **2010**.

[198] Martin, P. M., editor. "Handbook of deposition technologies for thin films and coatings". William Andrew (Elsevier), 3rd edition, **2010**.

[199] Horvath-Bordon, E., Riedel, R., Zerr, A. *et al.* "High-pressure chemistry of nitride-based materials" *Chem. Soc. Rev.*, **35**:987–1014, **2006**.

[200] Hisatomi, T., Teramura, K., Kubota, J., and Domen, K. "Characterization of spinel zinc titanium nitride oxide as a visible-light driven photocatalyst" *Bull. Chem. Soc. Jpn.*, **81**(12):1647–1656, **2008**.

[201] Shkabko, A., Aguirre, M. H., Marozau, I. *et al.* "Synthesis and transport properties of $SrTiO_{3-x}N_y$ /$SrTiO_{3-d}$ layered structures produced by microwave-induced plasma nitridation" *J. Phys. D: Appl. Phys.*, **42**(14):145202 1–8, **2009**.

[202] Zhu, Y., Li, Q., Mei, T., and Qian, Y. "Solid state synthesis of nitride, carbide and boride nanocrystals in an autoclave" *J. Mater. Chem.*, **21**(36):13756–13764, **2011**.